2019-01-01

Exploring Dynamic Triggering Of Earthquakes Within The United States & Quaternary Faulting And Urban Seismic Hazards In The El Paso Metropolitan Area

Richard Alexander Alfaro-Diaz
University of Texas at El Paso, Richard-Alfaro@outlook.com

EXPLORING DYNAMIC TRIGGERING OF EARTHQUAKES WITHIN THE UNITED STATES & QUATERNARY FAULTING AND URBAN SEISMIC HAZARDS IN THE EL PASO METROPOLITAN AREA

RICHARD ALEXANDER ALFARO-DIAZ

Doctoral Program in Geological Sciences

APPROVED:

Aaron A. Velasco, Ph.D., Chair

Terry L. Pavlis, Ph.D.

Jose M. Hurtado Jr., Ph.D.

Marianne Karplus, Ph.D.

Vladik Kreinovich Ph.D.

Charles Ambler, Ph.D.
Dean of the Graduate School

EXPLORING DYNAMIC TRIGGERING OF EARTHQUAKES WITHIN THE UNITED STATES & QUATERNARY FAULTING AND URBAN SEISMIC HAZARDS IN THE EL PASO METROPOLITAN AREA

by

RICHARD ALEXANDER ALFARO-DIAZ, B.S., M.S.

DISSERTATION

Presented to the Faculty of the Graduate School of

The University of Texas at El Paso

in Partial Fulfillment

of the Requirements

for the Degree of

DOCTOR OF PHILOSOPHY

Department of Geological Sciences

THE UNIVERSITY OF TEXAS AT EL PASO

May 2019

Table of Contents

List of Tables

List of Figures

Chapter 1: A Time-Domain Detection Approach to Identify Small Earthquakes within the Continental United States Recorded by the USArray and Regional Networks

Technological advances in combination with the onslaught of data availability allow for large seismic data streams to automatically and systematically be recorded, processed, and stored. Here, we develop an automated approach to identify small, local earthquakes within these large continuous seismic data records. Our aim is to automate the process of detecting small seismic events triggered by a distant large earthquake, recorded at a single station. Specifically, we apply time-domain short-term average (STA) to long-term average (LTA) ratio algorithms to three-component data to create a catalog of detections. We remove some of the false detections by requiring the detection be recorded on a minimum of two channels. To calibrate the algorithm, we compare our automatic detection catalog to a set of analyst-derived P-wave arrival times for a subset of small earthquakes occurring in the December 2008 Yellowstone swarm. Of the four STA/LTA algorithms we test (1 s/10 s; 4 s/40 s; 8 s/80 s; 16 s/160 s), the 1 s/10 s and 4 s/40 s detectors proved most effective at identifying the majority of events in the swarm. We apply these detectors to ±45 hrs and ±5 hrs of USArray data from the 2011 Japan M 9.0 and the 2010 Chile M 8.8 earthquakes, respectively. Using time-of-day versus number of detection relationships, we identify 38 of the 728 available stations that exhibit strong anthropogenic noise following the 2011 Japan earthquake. Our detection algorithm identified three regional earthquakes concurrent with the passage of the S and surface waves of the Chile mainshock at USArray station R11A that locate in the Coso region of California, as well as events in Texas following the Japan earthquake. This chapter is based on the paper (Velasco et. al., 2016).

1 INTRODUCTION

Remote triggering of earthquakes or other phenomena in the far field following the passage of large amplitude surface waves has been observed in some regions (small earthquakes [Pankow et al., 2004; Freed, 2005, and references therein], tremor [Aiken and Peng, 2014; Aiken et al., 2015], aseismic creep [Shelly et al., 2011], and clusters of events [Kato et al., 2013;

Saccorotti et al., 2013]). At these relatively remote distances, the mainshock-generated static stress changes are negligible and the dynamic stress changes are often an order of magnitude (or more) greater than static stress changes (e.g., Hill and Prejean, 2007, 2015). Over the last 20 years, there have been many observations of remotely triggered earthquakes, yet an understanding of the underlying physics that governs the triggering remains elusive (e.g., Hill et al., 1993; Kilb et al., 2002; Gomberg, 2013; van der Elst et al., 2013; Brodsky and van der Elst, 2014; Johnson et al., 2015). Resolving the source physics involved in remote earthquake triggering is compounded by the non-uniformity of seismic networks and the scarcity of seismic stations in some regions.

Within the last decade, the Incorporated Research Institutions for Seismology (IRIS) Data Management Center (DMC) has archived a four-fold increase in data and now this repository stores and distributes more than 350 TB of data (see Data and Resources). Of these data, ~50 TB are from the ~450 stations in the USArray Transportable Array (USArray TA) seismic network, which is a rolling array (traversing from west to east) throughout the North American continent (see Data and Resources). Since its inception in 2004, data recorded by the USArray TA network have been compiled into an extensive earthquake catalog that has reduced the magnitude of completeness level throughout the United States (Astiz et al., 2014).

The rapid increase in the rate of seismic data collection and distribution makes it difficult to manually review all seismic waveforms from all earthquakes, forcing seismologists to re-evaluate how they search for important seismic signatures. With the large amount of data currently being collected, new approaches to reviewing data must include semi to fully automated approaches specific to the scientific problem being addressed. Standard automated processing for seismic events has routinely occurred in seismology using global, regional, and

local networks, with some human review (e.g., the National Earthquake Information Center; the International Data Centre, Comprehensive Test Ban Treaty Organization, and other smaller local networks such as the University of Utah Seismograph Stations [UUSS]). However, detection of new signals of interest generally requires manual review of individual seismic traces. For example, volcanic tremor and/or nonvolcanic tremor create signals that are difficult to detect using standard approaches (e.g., Battaglia et al., 2005; Rubinstein et al., 2007; Shelly et al., 2007; Peng et al., 2009; Husker et al., 2010; Aiken et al., 2015), and generally are identified with manual review. Methods such as template matching can assist with the detection of specialized events (e.g., Van Trees, 1968; Schaff et al., 2004; Peng and Zhao, 2009; Rubinstein and Ellsworth, 2010; Shelly and Hardebeck, 2010; van der Elst et al., 2013), yet are limited to the template for which there is a match (Barrett and Beroza, 2014). Here, we develop a time-domain approach to automatically identify previously undetected remote dynamically triggered earthquakes using data from the USArray TA and regional networks within the continental United States (Fig. 1).

Our overall goal is to design detectors that can be applied to large data streams and produce an earthquake catalog robust enough to successfully test hypotheses pertaining to the source physics of remote earthquake triggering. To accomplish this, we focus on using a time-domain short-term average (STA) to long-term average (LTA) ratio automated detection algorithm to identify signals above the noise, which analysts can then review to determine if these signals are earthquakes. We explore different STA and LTA window lengths that we tune using data from two different seismic environments: (1) exceptionally quiet seismic stations located in areas with a relatively low number of seismic events and (2) relatively quiet seismic stations recording during the energetic 2008 Yellowstone earthquake swarm. We then apply our

preferred detectors to data recorded in the continental United States that recorded the remote 2010 M 8.8 Maule, Chile, and the 2011 M 9.0 Tohoku, Japan, earthquakes. One outcome of this analysis is the classification of stations particularly susceptible to anthropogenic noise.

2 DATA

To begin, we tune our detection algorithm using data from the December 2008 Yellowstone swarm (Farrell et al., 2010) (Fig. 2). Specifically, we examine three-component data from 29 December 2008 recorded by stations in the UUSS network. This swarm sequence has many small events closely spaced in time, as might be expected in remote aftershock sequences, and will allow us to test the capability of detecting multiple close-in-time events. For this 24-hr time period, the UUSS catalog contains 146 earthquakes that range in magnitude from 0.2 to 3.6 of which the majority of the events have a magnitude of ~1.5 (Fig. 3).

We also test our algorithms using three-component data from the ~450 stations in the USArray TA network (see Data and Resources) and available regional seismic networks within the continental United States. We focus on broadband channel data sampled at 40 or 100 samples per second (BH and HH channels, respectively). TA network stations have a regular station spacing of ~70 km, and each TA station records continuous three-component data. The TA network configuration differs as a function of time because the TA is a rolling array traversing from the west coast to the east coast of the contiguous United States. On average, each TA recording site is occupied for two years (see Data and Resources). When processing waveform data, we use the Standing Order Data interface (Owens et al., 2004) and FetchData (see Data and Resources) to request the seismic waveform data of interest, which we subsequently store on our local data servers in Seismic Analysis Code data format. We process one year of continuous data for stations TA.R11A, IU. ANMO, and IM.TX31 and ±5 and ±120 hrs for all available stations

from the 2010 M 8.8 Maule, Chile, and the 2011 M 9.0 Tohoku, Japan, earthquakes, respectively. We convert these data into an Antelope Boulder Real Time Technologies database for initial processing, and then we use MATLAB for post-processing.

3 METHOD

Automatic picking algorithms can be classified into four main families: energy methods (e.g., Allen, 1978, 1982; Baer and Kradolfer, 1987; Earle and Shearer, 1994; Xiantai et al., 2011; Lomax et al., 2012; Vassallo et al., 2012; Linville et al., 2014), autoregressive methods (e.g., Leonard and Kennet, 1999; Sleeman and Van Eck 1999; Leonard, 2000), neural network approaches (e.g., Dai and MacBeth, 1997; Zhao and Takano, 1999), and template matching (e.g., Shearer, 1994; Peng and Zhao, 2009; Shelly and Hardebeck, 2010; Zhang and Wen, 2015). Each method has advantages and disadvantages depending on the application. In this work, we choose the STA/LTA method, which is an energy method, for its simplicity in implementing and its sensitivity to a variety of signals. One requirement of the STA/LTA approach is it requires some a priori knowledge of the signal properties to set time-average windows, filter type, time between detections, and triggering thresholds. However, an advantage of this method is there are no restrictions on the characteristics of the detected signals (e.g., Vassallo et al., 2012).

We design the STA/LTA ratio detectors to identify signals within a continuous data stream that are above the noise floor. The STA is computed as the average of the L1 norm of the signal (i.e., average of the absolute values) of a relatively short time window, whereas the LTA uses a longer time window and again computes the average of the L1 norm of the signal. We test the time windows used to compute the STA and LTA values to design a method that will optimally detect local to regional earthquakes. We declare a detection when the ratio of these two values (STA/LTA) exceeds a predetermined threshold value. This method can be applied to any

time-series data, and here we apply the STA/LTA algorithms to both single-component (Z) and three-component data (Z, N, E).

The aim of the STA is to measure the instantaneous value of a seismic signal or its envelope, and in general it should be longer than a few periods of the target seismic signal and shorter than the shortest duration of the signal (Trnkoczy, 2002). Therefore, the STA choice is sensitive to the frequency (and user-imposed filters) of the seismic signal. In general, the LTA duration measures the average seismic noise or background amplitude, and should exceed a few cycles of the typical irregular seismic noise fluctuations (Trnkoczy, 2002). By changing the LTA window duration, the detector can become more or less sensitive to emergent signals and noise. In this work, we design and test four STA/LTA ratios that have different STA and LTA window lengths (Table 1). The first detector D uses a 1s/10 s ratio, which is similar to algorithms typically used for earthquake detection (e.g., Velasco et al., 2008). Here, we explore a wide range of parameters, testing STA/LTA windows of 4 s/40 s, 8 s/80 s, and 16 s/ 160 s window lengths. In urban areas prone to continuous anthropogenic seismic noise, it is best to reduce the LTA duration. For example, using a shorter LTA in the STA/LTA of 2 s/30 s (1:15 ratio) as opposed to 2 s/60 s (1:30 ratio) tends to reduce non-seismic false detections (Trnkoczy, 2002). The goal is to make the LTA short enough so the method can capture emergent signals while at the same time minimizing false triggers. In our tests, we maintain a 1:10 ratio for all STA/LTA combinations, which allows for similar sensitivities to noise characteristics and limits sensitivity to anthropogenic noise (Table 1).

The STA/LTA methods place no restrictions on the characteristics of the detected signals and thus the resulting detections may, or may not, be earthquakes. This differs from other detection algorithms that, for example, require the data match a predefined template signal (e.g.,

Shearer, 1994; Peng and Zhao, 2009; Shelly and Hardebeck, 2010; Zhang and Wen, 2015). Although STA/LTA methods will likely identify more spurious signals than match-filter techniques because the STA/LTA method is less restrictive, it is more apt to identify other, not yet identified signals.

To enhance the local earthquake signals, we first apply a 5-Hz high-pass filter to all seismograms, and then compute STA/LTA ratios for each of the three-component waveforms using the four detectors. For all tests, we assign a detection to any ratio that exceeds our threshold value of 3.5. Similar to implementing a signal-to-noise ratio restriction, this value allows for detections to be confidently determined, and also reduces the number of false detections and low-signal to noise detections. We store these final detections in our database along with the associated metadata.

4 RESULTS

4.1 STA/LTA Testing

We first determine how well our detectors perform using optimal data (i.e., high-signal-to-noise data, recorded in nonurban areas). For this, we analyze one year of continuous data (2007) focusing on three seismic stations from three different seismic networks (TA R11A, IU ANMO, and IM TX31). These stations were selected because they are known to be quiet stations (Bahavar and North, 2002; Wilson et al., 2002) and/or have been operational for many years. For simplicity, we detect events only on the vertical (BHZ) component, and count the number of detections in hourly bins over the year. In general, we find detectors D and Ev1 detect more signals than the Ev2 and Ev3 detectors, and that for all detectors the hourly bins show a significant increase in detections between UTC 12 and 15, corresponding to daytime hours at the

recording site (Fig. 4). We expect these increases are directly related to anthropogenic noise sources (mining explosions, city noise such as traffic, construction, etc.), suggesting that even for optimal data, anthropogenic-generated seismic signals can dominate and potentially bias detections from the quietest of stations during daylight hours (Astiz et al., 2014).

We next test our detection methods using data from the December 2008 Yellowstone swarm (Farrell et al., 2010). We focus on 24 hrs of data from 29 December 2008 that includes a large portion of events that are magnitude ~1.5, which is the lower limit of what we aim to detect with our algorithm given the ~70 km USArray TA station spacing. To improve detection capabilities and reduce the number of false detections, we add a restriction that detections must exist on two of the three channels processed (allowing a ~1 s lag time between channels). Figure 5 shows select three-component (BHZ, BHN, BHE for vertical, horizontal north–south, and horizontal east–west, respectively) seismograms and detections (D, Ev1, Ev2, Ev3) for the Yellowstone swarm data recorded at station H17A. The D and Ev1 detections that only occur on the Z-component waveforms (boxed for emphasis) are eliminated when requiring that a detection must be recorded on a minimum of two channels. In this example, the first D-detected event is a false positive, Ev2 does not detect the last clear earthquake in the waveform, and there is one event (mid-trace) that is only successfully detected by Ev1.

Applying our detectors and using the two-component detection restriction to the Yellowstone swarm data, we find that all of our methods (D, Ev1, Ev2, and Ev3) successfully capture the relative behavior and general temporal characteristics of the swarm (Fig. 6). Because our STA/LTA algorithm simply detects signals above the noise, it does not differentiate between P- and S-wave signals. Thus, we cannot determine the exact percentage of swarm earthquakes that we detected by our methods (i.e., if the P wave and S wave are both detected the method

would net two detections for one earthquake). Picking both phases could explain why the D detector nets more detections than events found in the UUSS catalog. The Ev3 detector detects some of the swarm events, but it also misses many of the earthquakes in the sequence. This is also true for the Ev2 detector, but to a lesser extent. These results indicate that of the four methods that include the two-component restriction, the D and Ev1 methods appear the best at identifying the majority of small earthquakes in the swarm.

We next determine how well our automated detection catalog compares with an independent catalog generated by a human analyst by conducting a blind (not using the detections as a guide) manual review of seismic data from the Yellowstone sequence for 29 December. To do this, we select data from three stations (US-LKWY, TAH17A, WY-YFT), located 5 km north, 22.5 km southwest, and 36.5 km west, respectively, from the center of the Yellowstone swarm (Fig. 2). These data are first preprocessed using a 5-Hz high-pass filter and then sorted by station and component. Examining individual seismograms (i.e., the three-component data were not viewed simultaneously), we conduct a blind search for high-frequency signals indicative of local earthquakes. We manually flag earthquakes using P picks on each individual component and then, similar to our auto-processing method, we remove some spurious detections by requiring detections be visible on a minimum of two components (allowing a ~1 s time lag).

We find that for station H17A, our human-reviewed catalog includes 859 possible earthquakes compared to 40 in the UUSS catalog and 488 found with the Ev1 auto-detector. The likely reason for the difference in the number of automatic detectors and human review is that when events in the swarm occur in rapid succession, a longer LTA window (e.g., Ev2, Ev3) encompasses multiple earthquakes and therefore the STA/LTA algorithm will not be able to

successfully differentiate each individual earthquake. Furthermore, it is much easier for an analyst to identify small events that have amplitudes just above the noise because they have an innate understanding of the characteristics of earthquake seismic signals, and they can explore the data interactively using zooming and filtering techniques, skills and tools which typically exceed the capabilities of automated methods.

To help judge how many false detections the automated STA/LTA detector nets and to quantify the improvements when using the two-component restriction, we conduct the following tests using the Yellowstone swarm data recorded at seismic stations LKWY (~5 km from the swarm) and YFT (~36.5 km from the swarm). Using seismic-wave velocities appropriate for the Yellowstone region (based on TauP; Crotwell et al., 1999), we calculate the travel time for Pand S waves from events in the swarm centroid to both stations. Using the spatial footprint of the swarm, which spans ~14 km in diameter, we assume errors in these travel-time estimates are less than three seconds for both the P-wave and S-wave arrivals. We next reduce all single-component vertical detection arrival times by the expected travel time from the swarm centroid to create a reduced detection time catalog for P-wave arrivals, such that the reduced arrival times from one earthquake that is detected at all stations should be within our anticipated error bounds. In this way, we visually examine all detections at the station farthest from the swarm (YFT) to determine if there is a corresponding detection at the closer station (LKWY). Because our detectors do not differentiate between P-wave and S-wave arrivals, we allow an additional 4-s error tolerance (the difference between S–P arrivals calculated using TauP, Crotwell et al., 1999) consistent with the scenario that the P wave is identified at the close station LKWY and the S wave being identified at the farthest station YFT. We flag all detections at station YFT that do not have a corresponding detection at the closest station LKWY (Table 2). We deem these

flagged detections as either false positives or assume they represent the detection of an earthquake not originating in the swarm. We also repeat these tests using a detection database created after applying the two-component detection restriction. We find that the two-component restriction is important in reducing false detections, as the false detections are reduced by 64%, 85%, 88%, and 75% for detectors D, Ev1, Ev2, and Ev3, respectively (Table 2).

4.2 The 11 March 2011 M 9.0 Tohoku, Japan, earthquake

We apply the detectors with the two-component restriction criteria to _120 hrs of USArray TA network data that recorded the 11 March 2011 05:46:24 (UTC) M 9.0 Tohoku, Japan, earthquake. Examining the cumulative number of detections from 728 stations (Fig. 7), we observe what appears to be a decrease in the rate of seismic events at the time of the mainshock. However, upon further investigation, we find an increased rate of detections at the onset of daytime hours and a decreased rate of detections at the onset of nighttime hours. We also find a day-of-the-week pattern with fewer events occurring on the weekend. We define night as 05:00 to 10:00 GMT. The seismic waves from the Tohoku earthquake swept through the USArray network on a Friday evening (local time); the apparent drop in detection rate in the 40 hrs following the earthquake is well correlated to a decrease in anthropogenic noise during the weekend (Fig. 7).

To further investigate the time-of-day pattern, we examine time-of-day histograms juxtaposed with the cumulative number of detections as a function of time for each of the 728 stations in the USArray network that recorded the 2011 M 9.0 Japan earthquake. Data from stations with strong anthropogenic signals produce peaked detection time-of-day histograms, typically displaying more daytime detections than nighttime detections, and also producing a stair-step behavior in the cumulative number of detections as a function of time (Fig. 8).

We identified 38 stations that have a peaked histogram distribution and stair-step behavior in the cumulative number versus time plots (Table 3), indicating that for these stations our detection algorithm is likely identifying anthropogenic noise signals, not seismic signals. Some of these 38 stations have known noise sources, such as stations CIA and NEE2 that are near airports, but the source of detected signals from other stations were initially more difficult to identify. For example, we found a strong signal during daytime hours at stations in close proximity to farms (Table 3), yet these signals also extended into nighttime hours. This may be due to animal sleep cycles (Campbell and Tobler, 1984) and therefore the observed signals are consistent with 20 consecutive hours of anthropogenic activity at dairy farms.

Examining the time-of-day distribution of detections and flagging any stations with non-uniform distributions are not foolproof methods in catching all strong anthropogenic signals. For example, the time-of-day detections at station UPAO is relatively uniform, but looking at the waveforms it is clear the detection algorithm is identifying signals that are not earthquakes (Fig. 9). These detections are attributed to the mechanics of a heating or cooling system at the University of Pittsburgh's Allegheny Observatory.

There is no case for widespread dynamic earthquake triggering in the five days following the Tohoku, Japan, earthquake within the footprint of the TA network (Fig. 4). Linville et al. (2014) reached the same conclusion using different processing methods. However, for a small spatial region near Snyder, Texas, remote seismicity triggered by the Tohoku earthquake was previously identified (van der Elst et al., 2013). To test our detection methodology, we manually reviewed the seismograms and Ev1 detections at stations in the vicinity of Snyder, Texas. We found that the Ev1 detector does successfully identify the seismic events (Fig. 10) occurring before and after the passage of the surface waves. However, these events occurred outside the

footprint of the array (the closest station, TA ABTX, was ~120 km away), and detections were limited to several stations, not enough to influence the array stack of detections (Fig. 7). This suggests that array stacks may be ineffective for identifying individual triggered events or triggering in limited spatial areas. Ideally, we should continue to pursue single-station detection rate changes as previously proposed (e.g., Velasco et al., 2008). However, given the variations in detection as a function of time-of-day and day of the week demonstrated here and in Linville et al. (2014), determining the significance of rate changes at individual stations is beyond the scope of this article.

4.3 The 27 February 2010 M 8.8 Offshore Maule Chile, earthquake

In a second analysis, we applied the Ev1 detector to ±5 hrs of USArray TA data with respect to the 27 February 2010 M 8.8 Offshore Maule Chile, earthquake, a typical win- dow used to identify dynamically triggered events (Velasco et al., 2008). This mainshock event occurred at 06:34:14 UTC. At this time, the centroid of the USArray network was in Denver, Colorado, where the local time was 11:34:14 p.m. MST. The fact that these data were collected during nighttime hours at the recording sites is optimal, for reducing the anthropogenic signals (Astiz et al., 2014). For these 10 hrs of data and using the two-station criteria, the Ev1 detector net a total of 6166 detections, of which approximately half, 2971, occurred in the 5 hrs following the mainshock. This indicates the earthquake rates in this region remained relatively constant before and after the Maule, Chile, mainshock seismic- wave passage based on ±5 hrs of data from the mainshock event, indicating that there was no widespread dynamic earth- quake triggering within the footprint of the array.

Looking at detections from each individual station separately, we found evidence of a small or potential rate increase following the mainshock for isolated areas. Specifically, at station

R11A, a high-signal-to-noise station, we found using the Ev1 detector that three regional earthquakes occurred during the mainshock coda. The first of these events occurred at the time of the mainshock's S-wave passage and the largest of the three events occurred at the time of the Love wave, while the other, and smallest event, occurred between the mainshock's S-wave and Love-wave arrivals (Fig. 11). The Lg- minus P-wave arrival times for all three small earthquakes (~38 s) indicates these events are ~300 km from station R11A. This successful identification of small events in the wavetrain of a large teleseismic event shows proof-of-concept that our automated detection algorithm can successfully accomplish our project goals of identifying potentially dynamically triggered events recorded by USArray.

One location that is consistent with the 330 km distance from station R11A is Coso Junction, California (−115.6°longitude; 38.35°latitude), and indeed we find three events located in Coso Junction in the Southern California Seismic Network (SCSN) catalog consistent with the recordings at R11A. The SCSN catalog also shows an increase in seismic activity near Coso began after the passage of the S wave (e.g., Peng et al., 2010). This increase in seismic activity suggests these events constitute remote aftershocks of the M 8.8 Chile earthquake triggered in the Coso Geothermal field, where in this case the onset of triggering began with the S wave. The important point here is that these potentially dynamically triggered events can be detected by our auto- mated approach, and that individual station rate changes could identify events, as seen with the Snyder, Texas, results.

5 DISCUSSION

Developing automated time-domain detectors to identify small signals within seismic data is challenging because a trade-off exists between identifying too many incorrect signals (false positives) versus missing key signals (missed detections). Because an earthquake's

waveform amplitude and duration scale with magnitude and source or station distance, it is difficult to design a one-size-fits-all detector. Our findings suggest that of the four single-station detectors we tested, the Ev1 detector, in combination with requiring a detection on a minimum of two components, is the preferred method to auto-detect earthquakes. However, this approach is not fool- proof, and we cannot rule out that this automated process may detect noise sources and/or not detect some earthquakes.

The STA/LTA time-domain single-station detection analysis is most successful at identifying small earthquakes when the dataset is rich in seismic signals and lacks anthropogenic sources. However, when there are minimal seismic events within the data, the detector is apt to identify non-earthquake signals. This results in a high number of false positives when the data has a paucity of earthquakes. Regardless of the approach, it is difficult to automatically remove all anthropogenic noise, which is typically much higher during daylight hours (Astiz et al., 2014). Our goal in this work was to automate the process of identifying small local earthquakes on single stations, yet we realize that analyst review is a critical component to finalize any catalog that will be subject to statistical tests.

In this work, we have flagged 38 stations (see Table 3) that have a strong time-of-day bias in the detections indicative of detecting primarily anthropogenic signals. We do not advocate completely discarding data from these flagged stations, nor focusing only on the best stations. Instead, our aim in listing these stations is to help future studies use the highest quality data first (i.e., station R11A) to test algorithms and then subsequently process the more challenging data.

In similar work, we have also explored other detection methods that use information contained within the frequency spectra of the data (Linville et al., 2014). Frequency-domain

detection methods can leverage the broadband nature of earthquake signals and avoid band-limited noise signals. However, they do require an added processing step to calculate the spectra. The pros and cons of opting for time-domain detection methods are that limited processing is required, yet these time-domain approaches are more susceptible to noise. Here, we have found that requiring the detections be identified on at least two of three components reduces the false positives but does not completely eliminate them. In the future, merging the time-domain and frequency-domain approaches may yield improved results for detecting remotely triggered small earth- quakes and other phenomena.

6 CONCLUSIONS

The four STA/LTA detection methods we tested successfully identified earthquake signals, and by requiring a multi-component approach false detections were reduced. An analysis of one-year worth of data confirms that even the quietest of stations are susceptible to anthropogenic noise. In our calibrated 2008 Yellowstone swarm dataset, we found that the Ev1 detector (5-Hz high pass, STA = 4, LTA = 40), in combination with the restriction that a detection be identified on at least two of the three channel components, reduces the number of high-frequency noise triggers and optimizes the detection of local earthquake events recorded by the UUSS network. Extending our investigation to examine ±120 hrs of data from the 11 March 2011 M 9.0 Japan, Tohoku, earthquake, we found the cumulative number of detections from all seismic stations had a rate increase at the transition to daytime hours and a rate decrease at the transition to nighttime hours, indicative of anthropogenic noise detections. Our results of the 2011 Japan data recorded in the USA also show evidence of a 40-hr weekend effect such that from Friday night to Sunday the anthropogenic signals that are detected are reduced because of reduced anthropogenic activity during the weekend. We have identified 38 stations that have

significant time-of-day rate changes likely caused by anthropogenic activities. Some of the noise sources are from known activities, such as airports, heating or cooling systems, farm-based activities, and car road traffic. To help inform future studies, in Table 3 we listed these 38 stations and made a note of the potential non-earthquake signals. Finally, applying our detectors to ±5 hrs of data from the 27 February 2010 M 8.8 Chile, earthquake, the Ev1 detector successfully identified three regional earthquakes during the teleseismic wavetrain concurrent with the passage of the S- and surface-wave passage at USArray TA station R11A. We conclude that automatic approaches can significantly assist with data reduction, yet careful analysis is needed to clearly identify triggered events within the wavetrain of the transient waves from large earthquakes.

Table 1.1 Short-term-average (STA) to long-term-average (LTA) detectors. Before the data is processed we apply a 5-Hz high-pass filter. A detection is flagged if the STA/LTA ratio exceeds the detection threshold, set here to 3.5 for all detectors.

Name	Filter	STA (s)	LTA (s)	Threshold Detection Level
D	HP 5 Hz	1	10	3.5
Ev1	HP 5 Hz	4	40	3.5
Ev2	HP 5 Hz	8	80	3.5
Ev3	HP 5 Hz	16	160	3.5

Table 2.1 Test using the Yellowstone swarm data to determine if it is productive to apply our restriction that eliminates all detections that are not identified on at least 2- of the 3-component data. To accomplish this we assume all detections at station YFT (36.5 km from the swarm) that do not have a corresponding detection (No Match; assumed false positive detection) at station LKWY (closest to the swarm, 5 km) are spurious. Note that the percentage of false positive detections for the 1-component method range from ~26-44%, whereas when the 2-component restriction is enforced these percentages drop to 10-17%, indicating the 2-component restriction is useful in eliminating false-positive detections.

1-Component				
Detector	**Number of LKWY Detections**	**Number of YFT Detections**	**Number of Detections at YFT that have No Match at LKWY**	**% of Detections with No Match**
D	1160	41	11	26.8
Ev1	488	34	13	38.2
Ev2	215	18	8	44.4
Ev3	154	12	4	33.3
2-Component				
D	755	32	4	12.5
Ev1	241	17	2	11.8
Ev2	123	6	1	16.7
Ev3	103	10	1	10

Table 3.1 List of seismic stations that recorded the 2011 Japan M=9 earthquake that have a peaked distribution in the time-of-day of the detections, suggesting these stations record a large amount of anthropogenic signals that our detectors are identifying. Stations are sorted by the total number of detections within our study period (i.e., ±120 hours from the 2011 Japan mainshock).

Number of detections within 90 hours	**Station Name**	**Lat**	**Lon**	**Town, State**	**Potential Noise Sources**
110	TZTN	-83.55	36.54	Tazewell, Tennessee	Housing, small farm
157	I25A	-103.73	44.02	Rochford, SD	Housing, and city to the south
159	S40A	-92.50	37.60	Lebanon, MO	Near Housing, and roads
164	C25A	-103.26	47.71	Freed Ranch, Watford, ND	Freed Ranch and Indian Hills Lodge
178	SNCC	-119.52	33.25	San Nicolas Island, CA	San Nicolas Naval Facility
200	J25A	-103.80	43.39	Sunshine Ranch, Edgemont, SD	Sunshine ranch, farm and city to the south
238	936A	-97.31	27.42	North Padre Island, Corpus Christi, TX	Padre Island National Seashore (national park), Padre Island National Seashore South Beach
241	D30A	-98.76	47.11	Buchanan, ND	River, roads, and farm

248	443A	-91.78	30.76	Delano Plantation, Melville, LA	Delano Plantation, and Atchafalaya River
252	NEE2	-114.62	34.77	Needles Airport, Needles, CA	Needles Airport
255	CNNC	-77.89	35.24	Cliffs of the Neuse, North Carolina	Cliffs of the Neuse State Park
288	PSUB	-75.45	39.92	Media, PA	Penn State - Brandywine Campus
291	WISH	-123.77	47.11	Wishka, WA	Wishkah Valley School District
293	PHIN	45.89	-119.92	Phinny Hill Vineyards, Prosser, WA, USA	Phinny Hill Vineyard, and Mercer Ranch Airport
350	Z40A	-93.4	33.26	Long Farm, Magnolia, AR	Long Farm, Housing, Roads
375	138A	-92.33	44.04	Scanlan Farm, Eyota, MN	Scanlan Farm, and Roads
402	ISA	-118.47	35.66	Isabella, Lake Isabella, CA	Road and campsites
417	BMR	-120.29	40.11	Black Mountain, California	Sierra Army Depot, and Patton Village
473	CIA	-118.42	33.40	Catalina Island Airport, Avalon, CA	Airport landing strip
477	439A	-94.77	30.79	Center Grove, Livingston, TX	Farm and river
528	F05D	-121.46	45.89	White Salmon, WA	Farm
577	W38A	-94.52	35.07	Poteau, OK	Housing, roads, and livestock
595	UPAO	-80.02	40.48	University of Pittsburgh's Allegheny Observatory, Pittsburgh, PA	University of Pittsburgh's Allegheny Observatory City noise, and a/c unit
643	MPH	-89.93	35.12	Memphis, TN	University of Memphis, and City noise
663	Y22D	-106.92	34.07	IRIS PASSCAL Instrument Center, Socorro, NM	Magdalena Ridge Observatory offices, and residential area
708	P37A	-94.35	39.59	Lathrop, MO	Road, housing, and construction
726	WRAK	-132.35	56.42	Wrangell Island, Southeastern Alaska	Near ship Port, and town
735	S22A	-106.83	37.75	4UR Ranch, Creede, CO	4UR Ranch, roads, and small town
849	JCT	-99.80	30.48	Junction, Texas	Near highway
891	SMM	-120.00	35.31	Simmler, CA	California Valley Airport
905	EGAK	-141.16	64.78	Eagle, Central Alaska, Alaska	Eagle Airport
1120	SOL	-117.25	32.84	Mt. Soledad, CA	Soledad Park
1131	GRA	-117.37	37.00	Grapevine Ranger Station, Death Valley, CA	Roads, and ranger station
1183	S38A	-93.91	37.63	Stockton, MO	Housing, farm, and livestock
1213	RCT	-119.24	36.31	Rector, Farmersville, CA	City noise, and agriculture
1340	W13A	-113.89	35.10	Hualapai Mountain Park, Kingman, AZ	Hualapai Mountain Resort, and public park
1413	DAN	-115.38	34.64	Danby, Needles, CA	Single House
1745	VES	-119.08	35.84	Vestal, Richgrove, CA	Farm, Agriculture

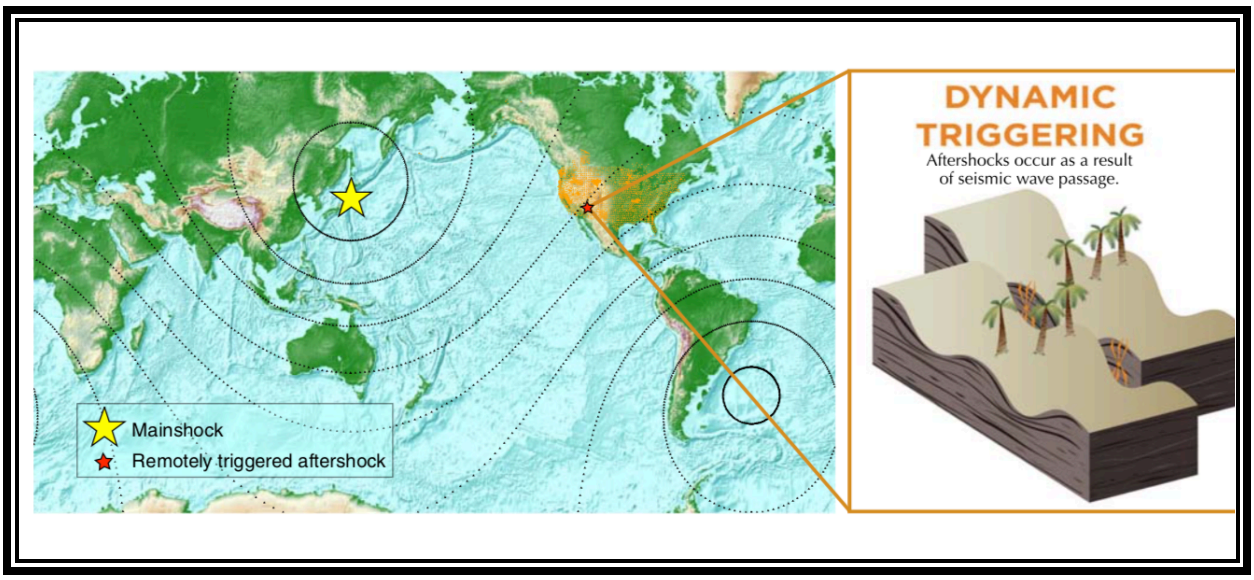

Figure 1.1 Our aim is to design an automated detection scheme to catalog local earthquakes recorded by the USArray Transportable Array (USArray TA) network (points distributed throughout the continental United States), which can be used to help test the hypothesis that a large earthquake (e.g., large star, contours illustrate the mainshock's seismic-waves trajectory where the bolder the contour the larger the seismic- wave amplitudes) can trigger small aftershocks at remote distances (i.e., small star, many mainshock fault lengths away). These distant aftershocks are assumed to be triggered by dynamic stress changes caused by the mainshock's seismic waves (pull-out cartoon). The color version of this figure is available only in the electronic edition.

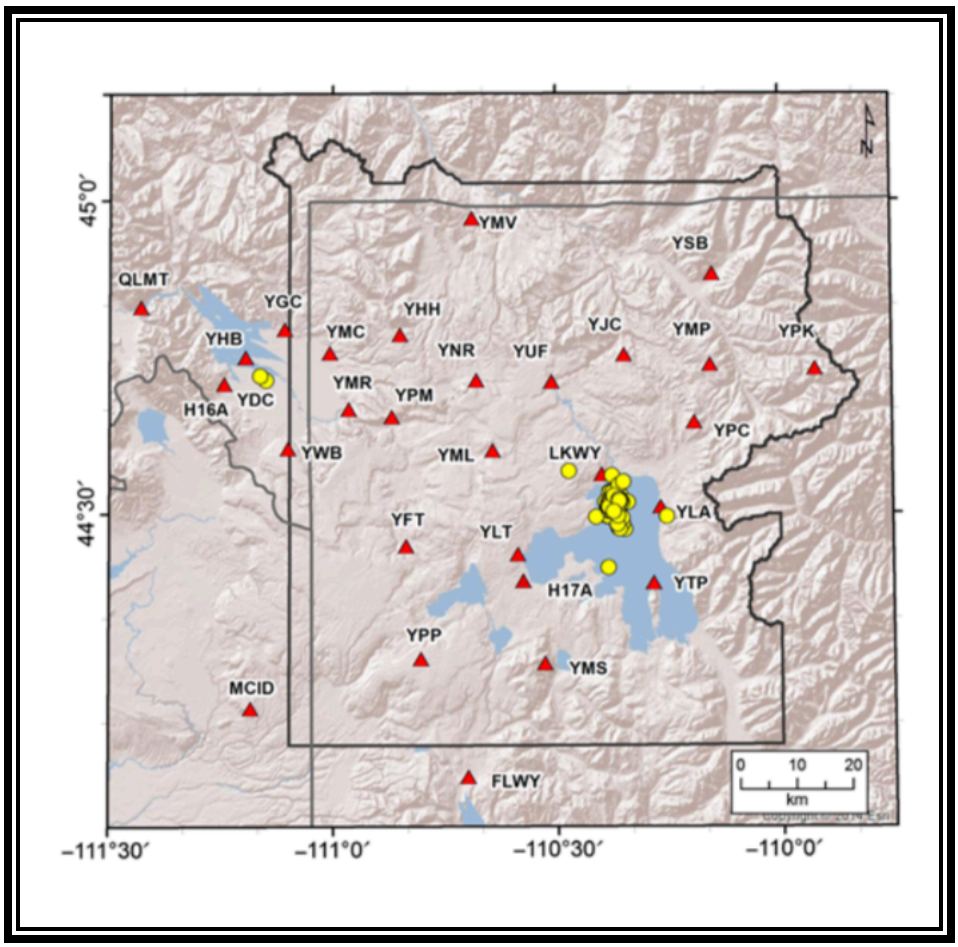

Figure 2.1 Map of the University of Utah Seismograph Stations (UUSS) regional seismic network for the Yellowstone region in December 2008 (triangles) and earthquakes originating on 29 December 2008 (circles). State boundaries (thin lines) and the extent of Yellowstone National Park (thick lines) are also shown. The color version of this figure is available only in the electronic edition.

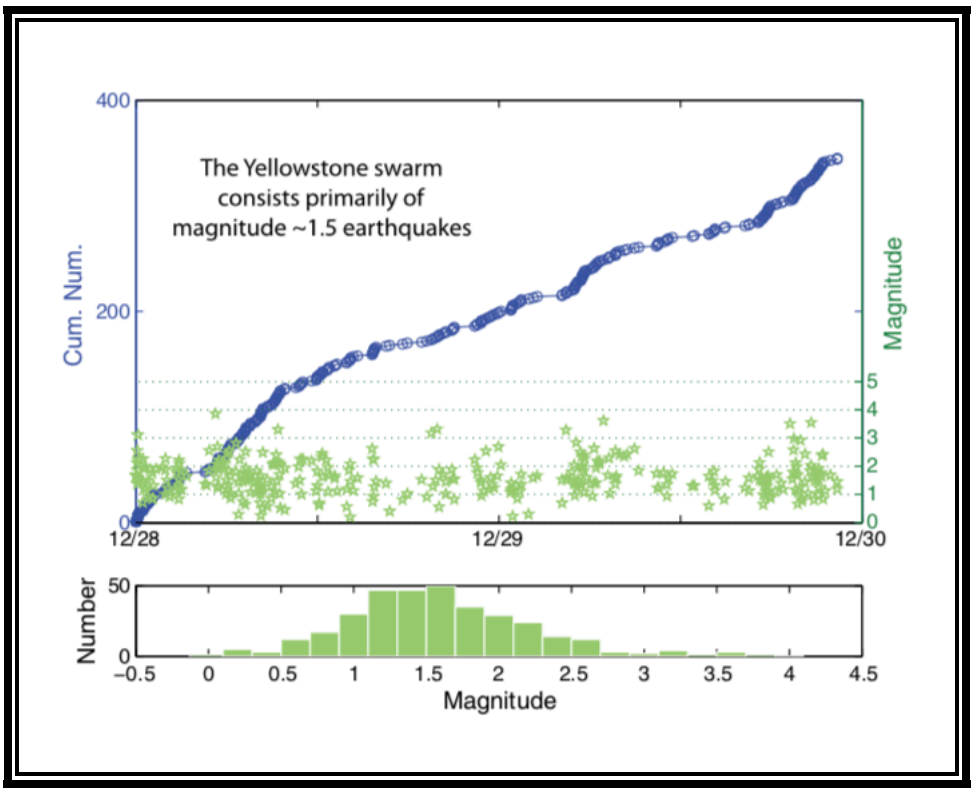

Figure 3.1 Two days of data from the Yellowstone swarm showing cumulative number of events (circles, left axis) and magnitude (stars, right axis). A histogram of the magnitude distribution is shown below. We focus on 24 hrs of data on 29 December 2008, which includes 146 events $0{:}2 \le M_L \le 3{:}6$. The color version of this figure is available only in the electronic edition.

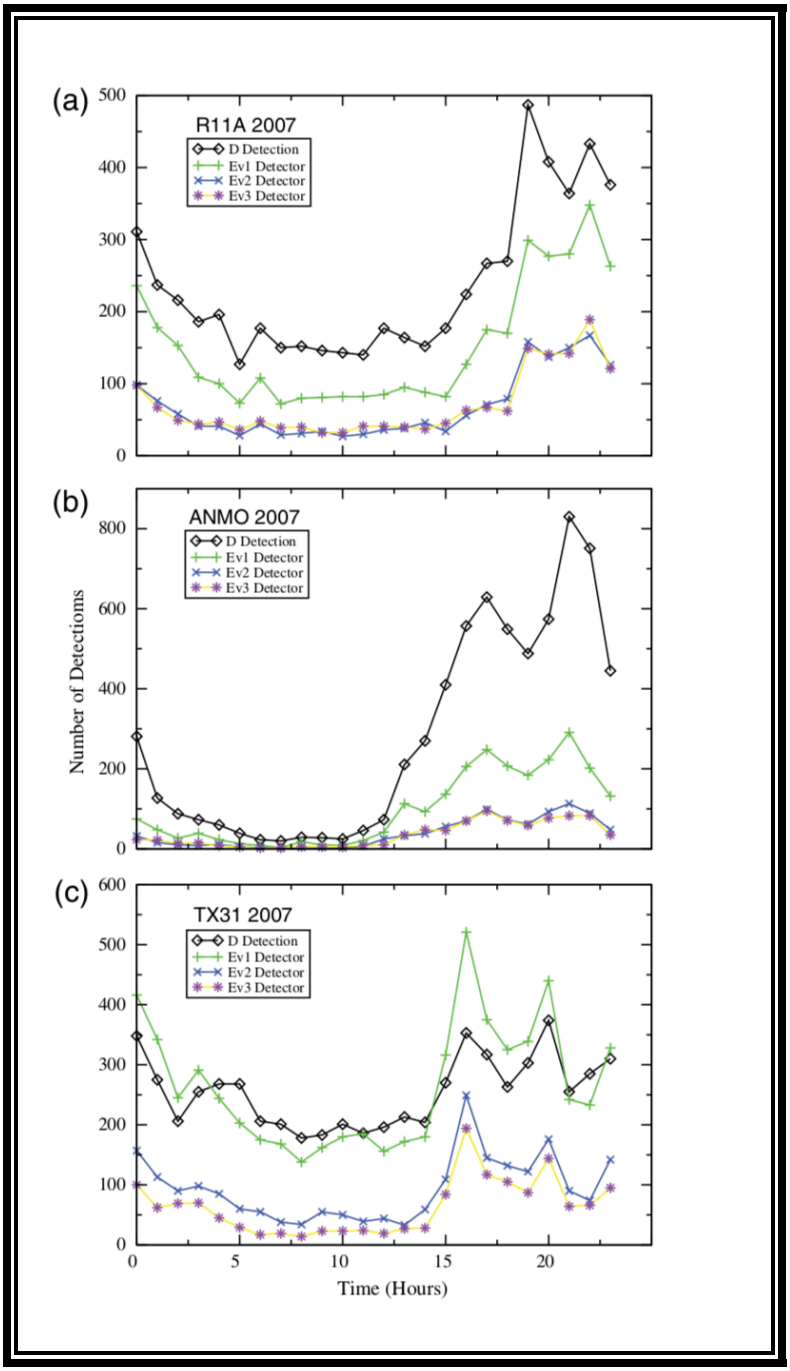

Figure 4.1 Number of detections as a function of time-of-day over a one-year period in 2007 for four different detection algorithms (D, Ev1, Ev2, Ev3; see Table 1). Data from seismic stations: (a) TA-R11A, (b) IU-ANMO, and (c) IM-TX31. For all three stations, there is an increase in detections during the daylight hours local time (between 11:00 UTC and 05:00 UTC) indicative of anthropogenic signals. The color version of this figure is available only in the electronic edition.

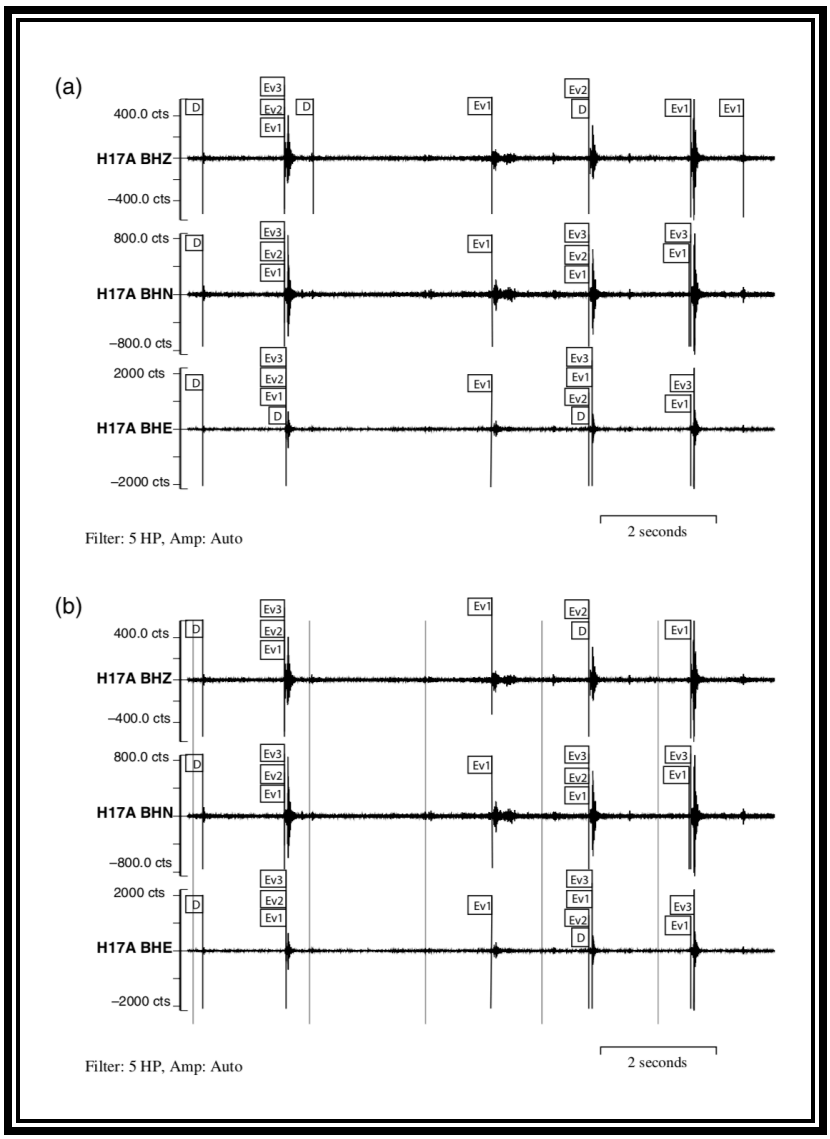

Figure 5.1 Select three-component seismograms from the Yellowstone swarm 29 December 2008, recorded at station H17A. Vertical lines indicate short-term average/long-term average (STA/LTA) algorithm detections with flags indicating the detector type, in which D _ 1 s=10 s; Ev1 _ 4 s=40 s; Ev2 _ 8 s=80 s; Ev3 _ 16 s=160 s. (a) Detections derived from processing each channel individually (BHZ, BHN, and BHE for vertical, horizontal north–south, and horizontal east–west, respectively). The D and Ev1 detections that only occur on the Z-component waveforms are false detections that can be easily removed in subsequent data processing as shown in (b). (b) Detections after requiring a detection must be recorded on a minimum of two channels (allowing a _1 s lag time between channels). In this example, the first D-detected event is a false positive, Ev2 does not detect the last clear earthquake in the waveform and there is one event (mid-trace) that is only successfully detected by Ev1.

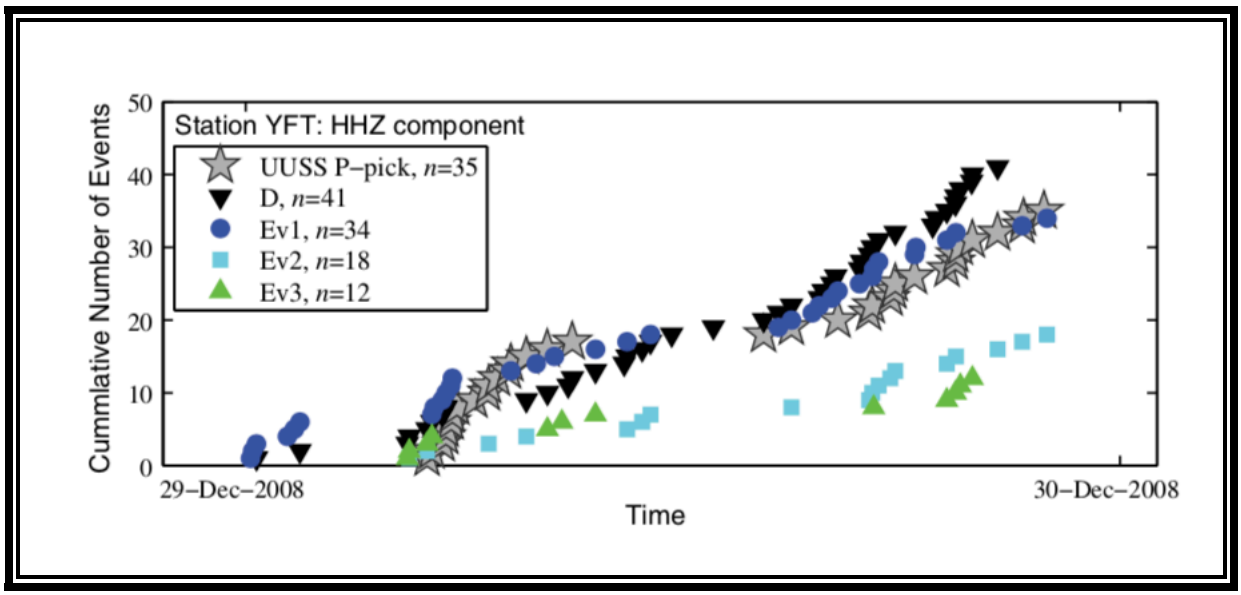

Figure 6.1 Data and detections from the 2008 Yellowstone swarm. The UUSS analyst reviewed P-wave detections (stars) and automated time-domain detections (EV1, circles; Ev2, squares; Ev3, triangles) are shown. The Ev1 and D detectors best capture the general characteristics of the swarm, unlike the Ev2 detector and the Ev3 detector that miss events. The color version of this figure is available only in the electronic edition.

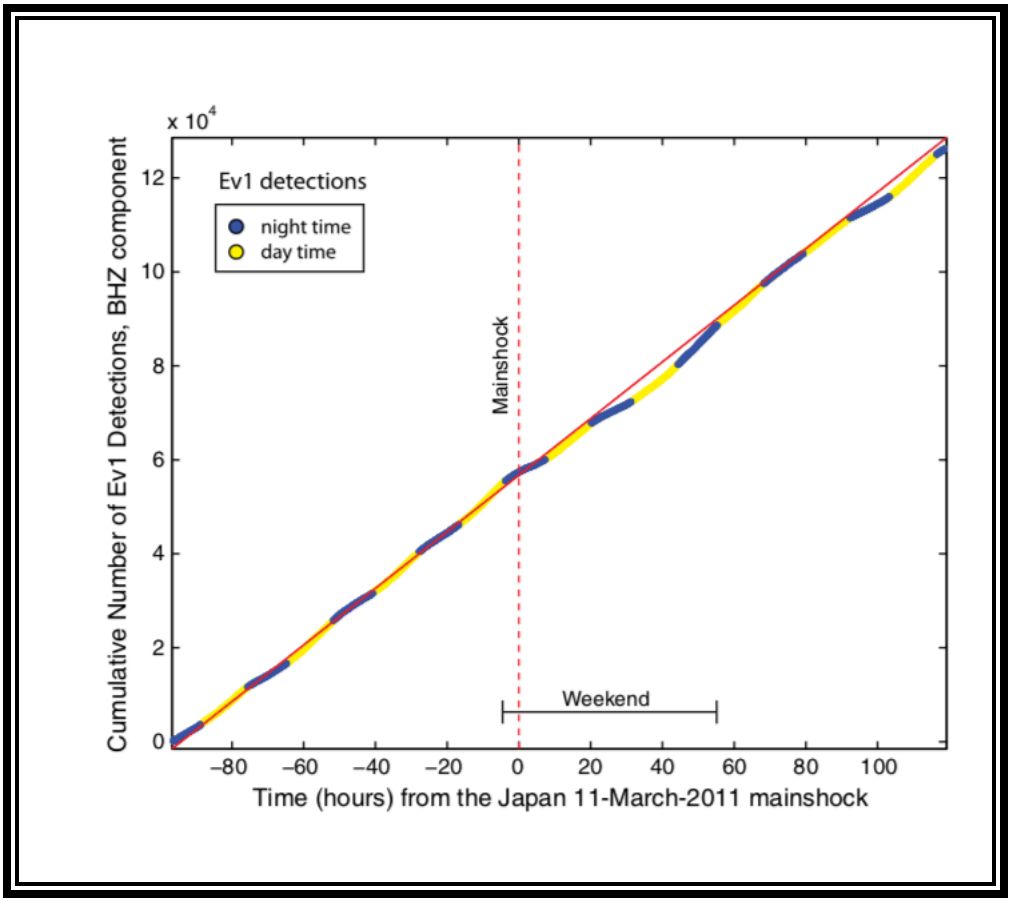

Figure 7.1 Cumulative number of detections from all 728 stations as a function of time. Data includes Ev1 detection spanning 90 hrs before and 120 hrs after the M 9.0 Tohoku earthquake. Time zero (dotted vertical line) corresponds to the origin time of the Tohoku mainshock on 11 March 2011 at 05:46:24 UTC. Detections are coded by day (lighter hue) and night (darker hue), where we define night as GMT 05:00 to 10:00, which corresponds to 9:00/ 10:00 p.m. to 2:00/3:00 a.m. PST/PDT and 12:00/1:00 a.m. to 5:00/6:00 a.m. EST/EDT. In general, detections rates are lower during the nighttime hours and higher during daytime hours, indicative of detecting anthropogenic activity. The color version of this figure is available only in the electronic edition.

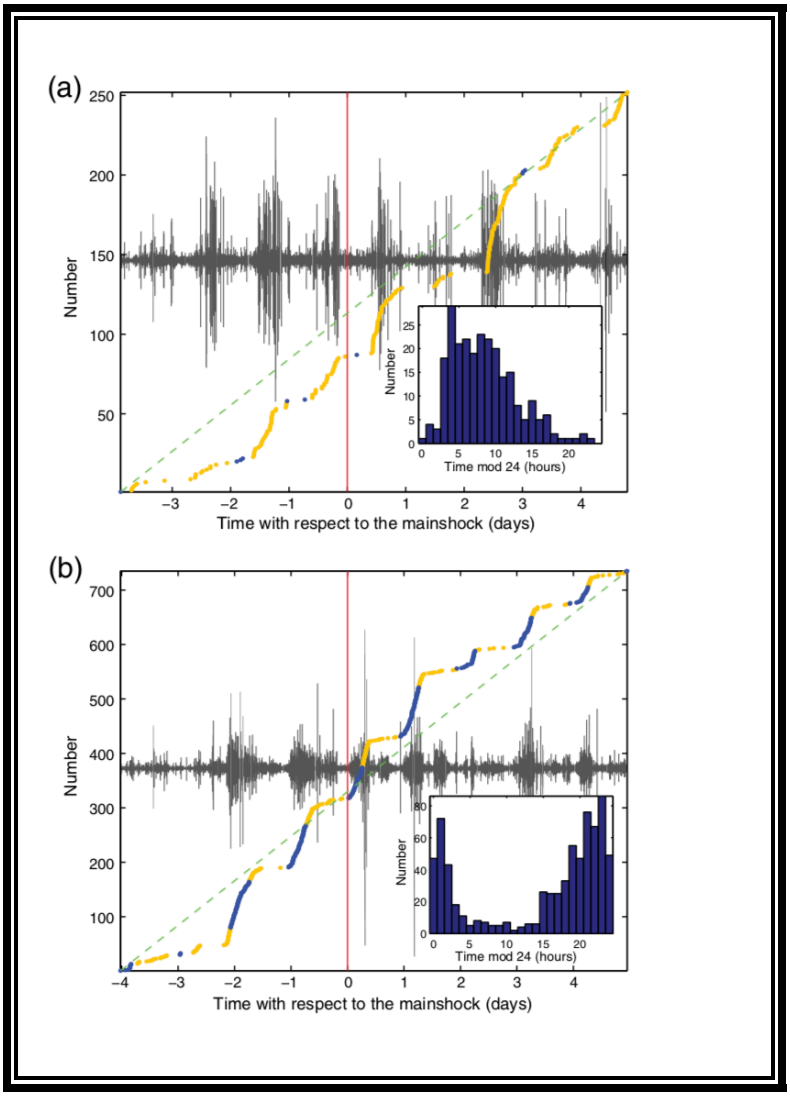

Figure 8.1 Example of two stations with detection histograms that have a peaked time-of-day distribution. Data are from the Ev1 STA/LTA time-domain detector database, spanning 4 days be- fore and 5 days after the 2011 M 9.0 Tohoku Earthquake. (a) Data from CI network station NEE2, located at the Needles Airport, Needles, California. The corresponding 5 Hz filtered waveform is dis- played in the background of the cumulative number of detections versus time plot. Time zero (vertical line) corresponds to the origin time of the Tohoku M 9.0 mainshock earthquake. Detections are coded by day (lighter hue) and night (darker hue), where we define night as 05:00 to 10:00 GMT. Inset shows a histogram of the detections (same 9 days) as a function of time-of-day, indicating most detections are in the daytime, and likely are anthropogenic signals from the activity at the Needles Airport. (b) As in (a) for TA Network station S22A at 4UR Ranch in Creede, Colorado. These data show most, but not all, of the detections are during the nighttime and the regularity of this behavior suggests these detections are likely identifying anthropogenic signals. The color version of this figure is available only in the electronic edition.

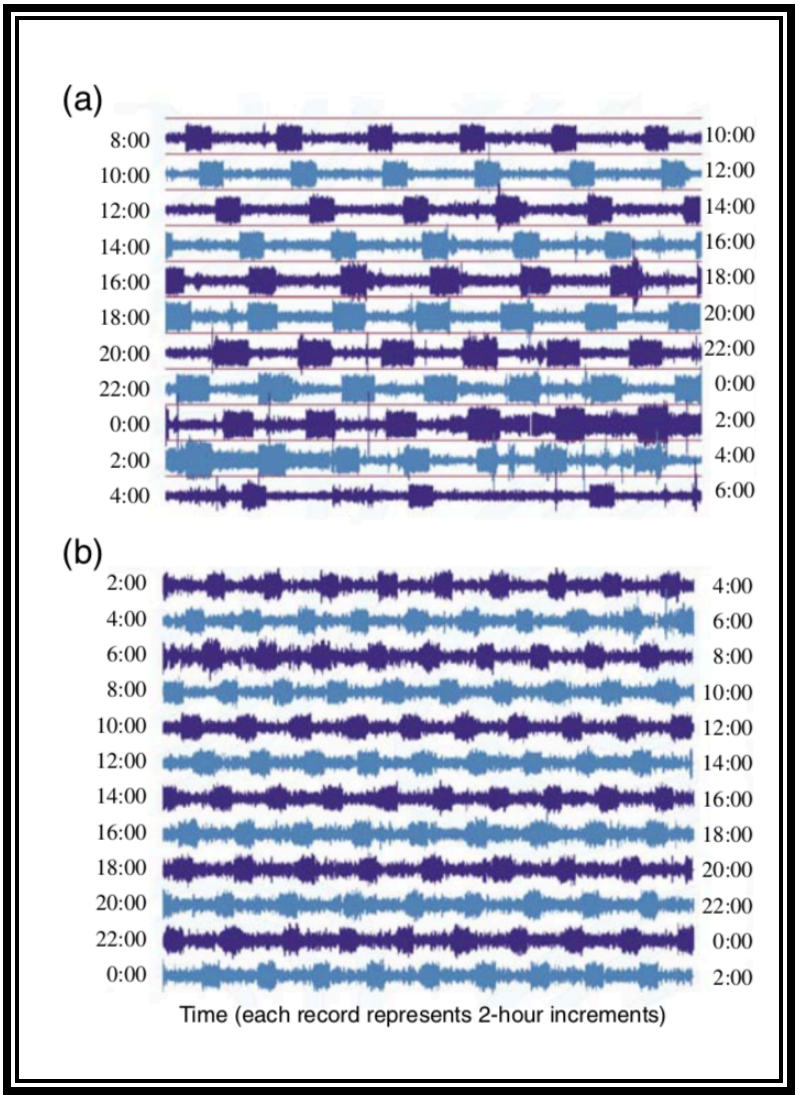

Figure 9.1 Record section from station UPAO (80.02° W, 40.48° N) located at the University of Pittsburgh's Allegheny Observatory. Wave- form data show a prevalence of nonseismic noise likely related to the air circulation system. Automated STA/LTA detection might incorrectly catalog these signals because of the large signal to noise ratio. (a) Summertime data recording at station UPAO. (b) Wintertime recording at station UPAO. These data snapshots are from the Rapid Earthquake Viewer (REV) (see Data and Resources). The color version of this figure is available only in the electronic edition.

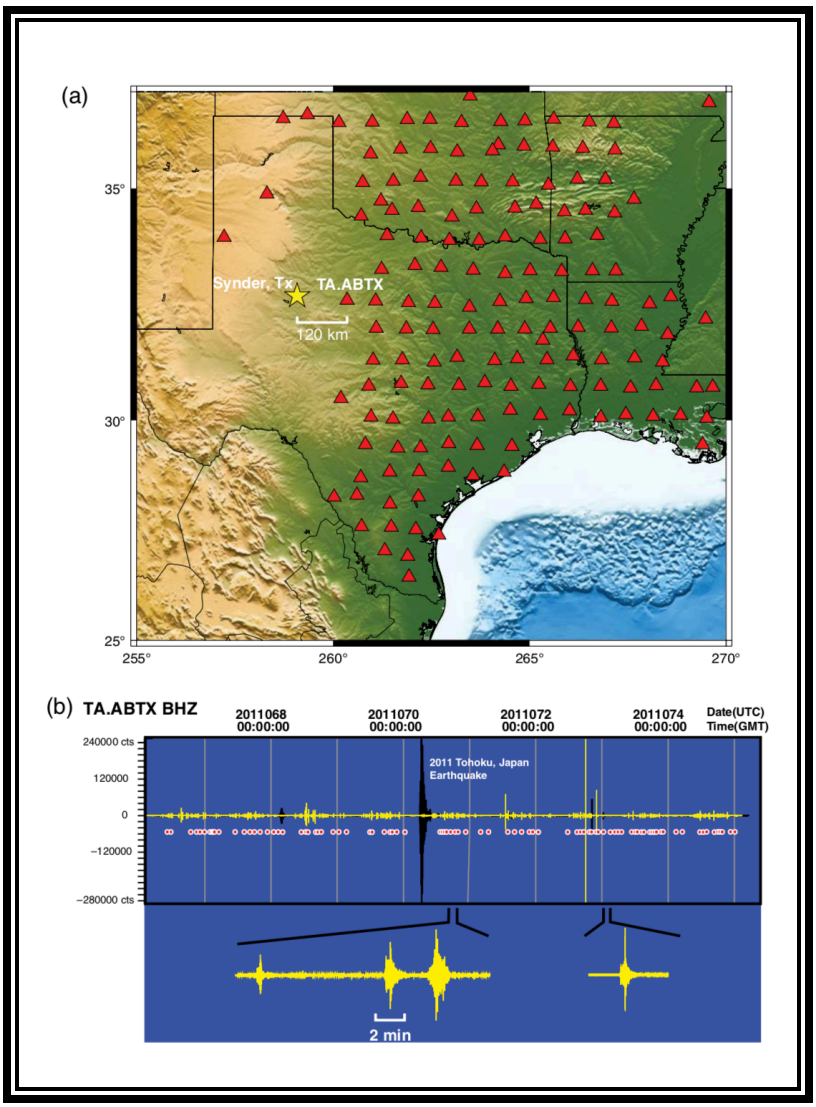

Figure 10.1 (a) Seismic station map of the South Midwestern United States at the time of the 11 March 2011 05:46:24 (UTC) M 9.0 Tohoku, Japan, earthquake. Operational USArray TA stations and regional seismic network stations are shown as triangles, and a star marks Snyder, Texas, where remotely triggered earthquakes were reported (van der Elst et al., 2013). The closest TA station to Snyder, Texas, is station ABTX, which is ~120 km away. (b) Seismogram (BHZ component) from TA station ABTX showing 9 days of data (4 days before and 5 days after the Tohoku mainshock). Juxtaposed on the raw data (dark hue waveforms; Tohoku mainshock labeled) is 5-Hz high-pass data (light hue waveforms). Circles indicate Ev1 detections. Zoom highlights examples of locally triggered earthquakes detected by the Ev1 detector. The Ev1 detector successfully identifies events triggered by the M 9.0 Tohoku, Japan, earthquake; however because these triggering events were off array, manual review is required to flag these detections as remotely triggered aftershocks. The color version of this figure is available only in the electronic edition.

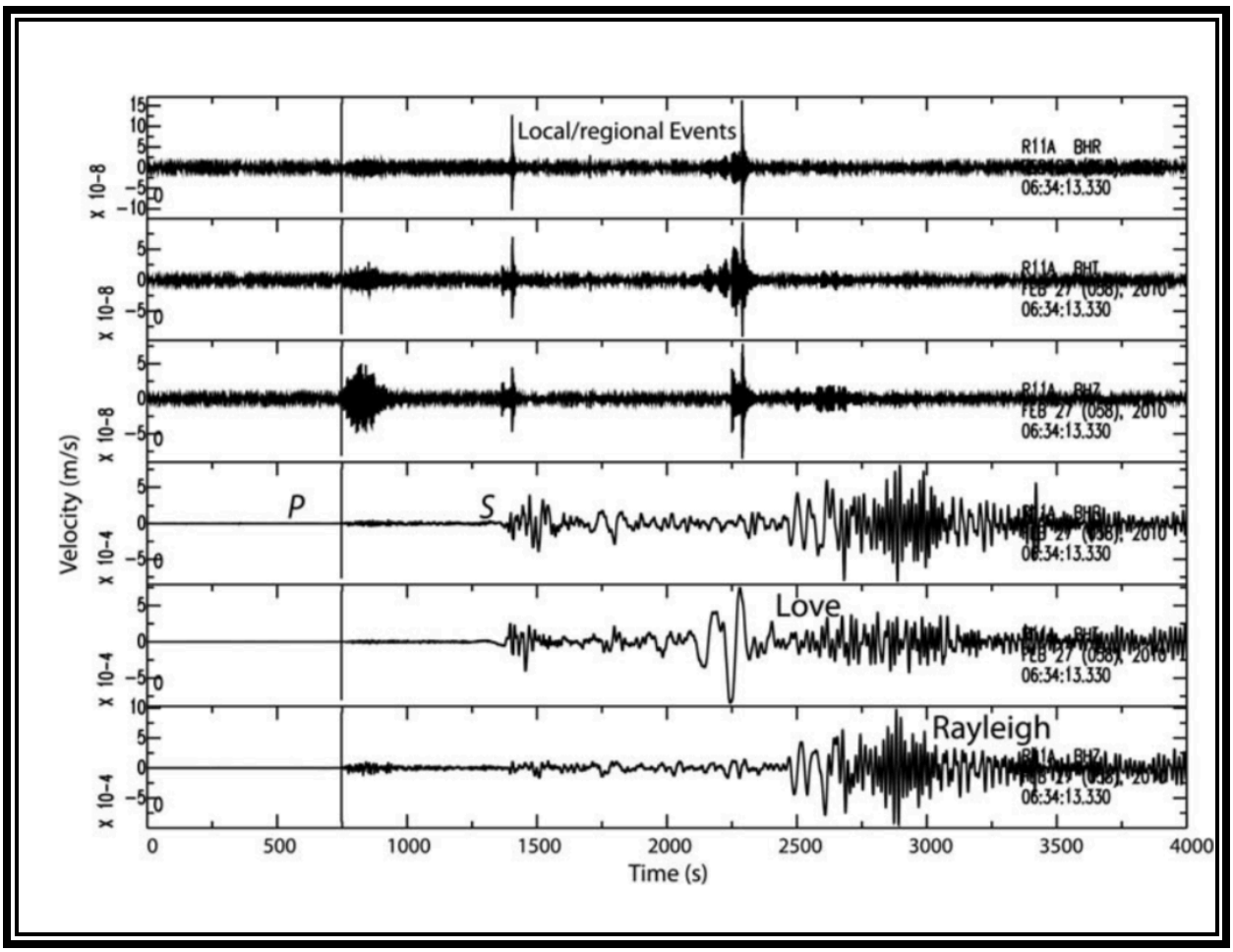

Figure 11.1 Seismic waveforms from the 27 February 2010 06:34:14 M 8.8 Offshore Bio Bio, Chile, earthquake recorded at USArray TA station R11A. Top three waveforms are high-pass filtered at 5 Hz, which removes the surface-wave signal and reveals three regional events in the mainshock coda wave that arrive at the time of the S wave (first event) the Love wave (third and largest event) and at a time in between the S- and Love wave (second and smallest event). Bottom three waveforms display the raw waveform data.

References

Allen, R. V., Automatic earthquake recognition and timing from single traces, *Bull. Seismol. Soc. Am.*, 68, 1,521–1,532, 1978.

Allen, R. V., Automatic phase pickers: heir present use and future prospects, *Bull. Seismol. Soc. Am.*, 72, S225–S242, 1982.

Astiz, L., J. H. Dieterich, C. Frohlich, B. H. Hager, R. Juanes, and J. H. Shaw, On the potential for induced seismicity at the Cavone oilfield: Analysis of geological and geophysical data, and geomechanical modeling, Report for the Laboratorio di Monitoraggio Cavone, 139 pp, 2014. [Available at http://labcavone.it/documenti/32/allegatrapporto-studiogiacimento.pdf.]

Aiken, C. and Z. Peng, Dynamic triggering of microearthquakes in three geothermal/volcanic regions of California, *J. Geophys. Res.*, 119, 6992–7009, 10.1002/2014JB011218, 2014.

Aiken, C., J. P. Zimmerman, Z. Peng, and J. I. Walter, Triggered Seismic Events along the Eastern Denali Fault in Northwest Canada Following the 2012 Mw 7.8 Haida Gwaii, 2013 Mw 7.5 Craig, and Two Mw>8.5 Teleseismic Earthquakes, Bulletin of the Seismological Society of America, 105(2B), 1165–1177, doi:10.1785/0120140156, 2015.

Baer, M., and U. Kradolfer, An automatic phase picker for local and teleseismic events, *Bull. Seismol. Soc. Am.*, 77, 1,437–1,445, 1987.

Bahavar, M., and R. North, Estimation of background noise for International Monitoring System seismic stations, *Pure and Applied Geophys.*, 159, 911-944, 2002.

Barrett, S. A., and G. C. Beroza, An empirical approach to subspace detection, *Seism. Res. Lett.*, 85, 594-599, 2014.

Battaglia, J., V. Ferrazzini, T. Staudacher, K. Aki, and J.-L. Cheminee, Pre-eruptive migration of earthquakes at the Piton de la Fournaisevolcano (Reunion Island), *Geophys. J. Int.*, 161, 449– 458, 2005.

Brodsky, E.E., N.J. van der Elst, The uses of dynamic earthquake triggering, Annual Reviews of Earth and Planetary Sciences, 42, 317-339, DOI: 10.1146/annurev-earth-060313-054648, 2014.

Campbell, S.S. and I. Tobler, Animal sleep: a review of sleep duration across phylogeny, *Neuroscience and Biobehavioral Rev.*, 8, 269-300, 1984.

Crotwell, H. P., T. J. Owens, and J. Ritsema, The TauP Toolkit: Flexible seismic travel-time and ray-path utilities, *Seism. Res. Lett.*, 70, 154–160, 1999.

Dai, H., and C. MacBeth, The application of back-propagation neural network to automatic picking seismic arrivals from single-component recordings, *J. Geophys. Res.*, 102, 15,105–15,115, 1997.

Earle, P. S., and P. M. Shearer, Characterization of global seismograms using an automatic-picking algorithm, *Bull. Seismol. Soc. Am.*, 84, 366–376, 1994.

Farrell, J., R. B. Smith, T. Taira, W.-L. Chang, and C. M. Puskas, Dynamics and Rapid Migration of the Energetic 2008–2009 Yellowstone Lake Earthquake Swarm, *Geophysical Research Letters* 37, no. 19 (October 1, 2010): L19305. doi:10.1029/2010GL044605, 2010.

Freed, A. M., Earthquake Triggering by Static, Dynamic, and Postseismic Stress Transfer, Annual Review of Earth and Planetary Sciences, 33(1), 335–367, doi:10.1146/annurev.earth.33.092203.122505, 2005.

Gomberg, J., Permanently enhanced dynamic triggering probabilities as evidenced by two M≥ 7.5 earthquakes, *Geophys. Res. Lett.*, 40, 1–6, doi:10.1002/grl.50933, 2013.

Hill, D. P., P. A. Reasenberg, A. Michael, W. J. Arabaz, G. Beroza, D. Brumbaugh, J. N. Brune, et al.m Seismicity Remotely Triggered by the Magnitude 7.3 Landers, California, Earthquake, *Science* 260, no. 5114 (June 11, 1993): 1617–23. doi:10.1126/science.260.5114.1617, 1993.

Hill, D.P., and S. Prejean, Dynamic triggering, in H. Kanamori (ed.) V. 4 *Earthquake Seismology*, pp. 258-288, Treatise on Geophysics (G. Schubert, ed. in chief), Elsevier, Amsterdam, 2007.

Hill, D.P., and S. Prejean, Dynamic triggering, in H. Kanamori (ed.) V. 4 *Earthquake Seismology*, Treatise on Geophysics, 2nd edition (G. Schubert, ed. in chief), Elsevier, Amsterdam, 2015.

Husker, A., S. Peyrat, N. Shapiro, and V. Kostoglodov, Automatic non-volcanic tremor detection in the Mexican subduction zone, Geofis. Int., 49(1), 17–25, 2010.

Incorporated Research Institutions for Seismology (IRIS), Web Service Fetch Scripts. Retrieved from https://seiscode.iris.washington.edu/projects/ws-fetch-scripts, March, 2015.

Johnson, C. W., R. Bürgmann, and F. F. Pollitz, Rare dynamic triggering of remote M≥5.5 earthquakes from global catalog analysis, J. Geophys. Res. Solid Earth, 120(3), 2014JB011788, doi:10.1002/2014JB011788, 2015.

Kato, A., J. Fukuda, and K. Obara, Response of seismicity to static and dynamic stress changes induced by the 2011 M9.0 Tohoku-Oki earthquake, Geophys. Res. Lett., 40, 3572–3578, doi:10.1002/grl.50699, 2013.

Kilb, D., J. Gomberg and P. Bodin, Aftershock triggering by complete Coulomb Stress changes, J. Geophys. Res., 107, 10.1029/2001JB000202, 2002.

Leonard, M., Comparison of manual and automatic onset time picking, Bull. Seismol. Soc. Am., 90, 1,384–1,390, 2000.

Leonard, M., and B. L. N. Kennett, Multi-component autoregressive techniques for the analysis of seismograms, Physics Earth and Planet. Int., 113, 247–263, 1999.

Linville, L., K. L. Pankow, D. L. Kilb, and A. A. Velasco, Exploring Remote Earthquake Triggering Potential Across Earthscope's Transportable Array through Frequency Domain Array Visualization, J. Geophys. Res., 119, 8950–8963, doi:10.1002/2014JB011529, 2014.

Lomax, A., M. Vassallo, and C. Satriano, Automatic picker developments and optimization: FilterPicker—a robust, broadband picker for real-time seismic monitoring and earthquake early warning, Seismological Res. Lett., 83, 531–540, 2012.

Owens, J., H. P. Crotwell, C. Groves, and P. Oliver-Paul, "SOD: Standing Order for Data", Seismological Research Letters, 75:515–520, 2004.

Pankow, K. L., W.J. Arabasz, J.C. Pechmann, and S.J. Nava, Triggered seismicity in Utah from the 3 November 2002 Denali fault earthquake, *Bull. Seis. Soc. Am.*, 94(6), 332-347, 2004.

Peng, Z., and P. Zhao, Migration of early aftershocks following the 2004 Parkfield earthquake, *Nat. Geosci.*, 2, 877–881, 2009.

Peng, Z., J. E. Vidale, A. G. Wech, R. M. Nadeau, and K. C. Creager, Remote triggering of tremor along the San Andreas fault in central California, *J. Geophys. Res.* ,114, no. B00A06, doi: 10.1029/2008JB006049, 2009.

Peng, Z., D. P. Hill, D. R. Shelly, and C. Aiken, Remotely triggered microearthquakes and tremor in central California following the 2010 Mw 8.8 Chile earthquake, *Geophys. Res. Lett.*, 37, L24312, doi:10.1029/2010GL045462, 2010.

Rubenstein, J. L., J. E. Vidale, J. Gomberg, P. Bodin, K. C. Creager, S. D. Malone, Non-volcanic tremor driven by large transient shear stresses, *Nature*, 448,579–582, 2007.

Rubinstein, J. L., and W. L. Ellsworth, Precise estimation of repeating earthquake moment: Example from Parkfield, California, *Bull. Seismol. Soc. Am.*, 100, 1952–1961, 2010.

Saccorotti, G., D. Piccinini, F. Mazzarini, and M. Zupo, Remotely triggered micro-earthquakes in the Larderello-Travale Geothermal Field (Italy) following the 2012 May 20, Mw 5.9, Poplain earthquake, *Geophys. Res. Lett.*, 40, 835–840, doi:10.1002/grl.50254, 2013.

Schaff, D. P., G. H. R. Bokelmann, W. L. Ellsworth, E. Zanzerkia, F. Waldhauser, and G. C. Beroza, Optimizing correlation techniques for improved earthquake location, , 94, 705–721, 2004.

Shearer, P. M., Global seismic event detection using a matched filter on long-period seismograms, J. Geophys. Res., 99(B7), 13713–13725, doi:10.1029/94JB00498, 1994.

Shelly, D. R., G. C. Beroza, and S. Ide, Non-volcanic tremor and low frequency earthquake swarms, *Nature*, 446, 305–307, doi:10.1038/nature05666, 2007.

Shelly, D. R., Z. Peng, D. P. Hill, and C. Aiken, Triggered creep as a possible mechanism for delayed dynamic triggering of tremor and earthquakes, *Nature Geoscience*, 4, June 2011, DOI: 10.1038/NGEO1141, 2011.

Shelly, D. R., and J. L. Hardebeck, Precise tremor source locations and amplitude variations along the lower-crustal central San Andreas Fault, *Geophys. Res. Lett.*, 37, L14301, doi:10.1029/2010GL043672, 2010.

Sleeman, R. and T. van Eck, Robust automatic P-phase picking: an on-line implementation in the analysis of broadband seismogram recordings, *Physics Earth and Planet. Int.*, 113, 265–275, 1999.

Trnkoczy, A, Understanding and parameter setting of STA/LTA trigger algorithm, *IASPEI New Manual of Seismological Observatory Practice*, 2, 1-19. 2002.

van der Elst, N. J., H. M. Savage, K. M. Keranen, and G. A. Abers, Enhanced remote earthquake triggering at fluid-injection sites in themidwestern United States, Science, 341, 164–167, 2013.

Van Trees, H. L. Detection, Estimation and Modulation Theory, Vol. 1, John Wiley and Sons, New York, 1968.

Vassallo, M., C. Satriano, and A. Lomax, Automatic picker developments and optimization: A strategy for improving the performances of automatic phase pickers, *Seism. Res. Lett.*, 83, doi: 10.1785/gssrl.83.3.541, 2012.

Velasco, A. A., S. Hernandez, T. Parsons, and K. Pankow, Global ubiquity of dynamic earthquake triggering, Nature Geoscience, Published online: 25 May 2008; doi:10.1038/ngeo204, 2008.

Velasco, A. A., Alfaro-Diaz, R., Kilb, D., & Pankow, K. L. (2016). A Time-Domain Detection Approach to Identify Small Earthquakes within the Continental United States Recorded by the USArray and Regional Networks. *Bulletin of the Seismological Society of America*, *106*(2), 512–525. https://doi.org/10.1785/0120150156

Wessel, P., and W. H. F. Smith, New, improved version of the Generic Mapping Tools Released, *EOS Trans. AGU*, 79, 579, 1998.

Wilson, D., J. Leon, R.Aster, J. Ni, J. Schlue, S. Grand, S. Semken, S. Baldridge, and W. Gao, Broadband seismic background noise at temporary seismic stations observed on a regional scale in the southwestern United States, *Bull. Seismol. Soc. Am.*, 92, 3335–3341, 2002.

Xiantai, G., L. Zhimin, Q. Na, J. Weidong, Adaptive picking of microseismic event arrival using a power spectrum envelope, *Comp. & Geo.*, 37, 158–164, 2011.

Zhang, M., and L. Wen, Earthquake characteristics before eruptions of Japan's Ontake volcano in 2007 and 2014, Geophys. Res. Lett., 2015GL065165, doi:10.1002/2015GL065165, 2015.

Zhao, Y., and K. Takano, An artificial neural network approach for broadband seismic phase picking, *Bull. Seismol. Soc. Am.*, 89, 670-680, 1999.

Chapter 2: Optimally Oriented Remote Triggering in the Coso Geothermal Region

Using 13 years of data (2004-2016) from the EarthScope USArray Transportable Array and the Southern California Seismic Network, we search for remotely triggered seismicity in the Coso Geothermal Field (CGF), California. We first apply a short term to long term average ratio detector to high-pass (5 Hz) filtered waveforms spanning ±5 hours encompassing 211 M ≥ 7 global earthquakes. We visually inspect these waveforms to identify uncatalogued local earthquakes. We use our augmented local earthquake catalog to investigate remote earthquake triggering in the CGF region. Flagging mainshocks with a statistically significant increase in seismicity following the P-wave arrival, we find that of the 211 remote mainshocks, 32 (15%) triggered seismicity in the CGF. An additional 9 mainshocks had local earthquakes coincident with the surface waves, but no statistically significant rate increase was found. Of the 41 (19%) triggering mainshocks, 28 and 13 exhibit instantaneous and delayed triggering, respectively. We find no correlation between triggering and mainshock depth, peak dynamic stress, nor mainshock focal mechanism type. However, the CGF is optimally oriented for remote triggering from mainshocks in the West Pacific, since dynamic stresses align favorably with the local stress field (maximum horizontal stress).

1 INTRODUCTION

Static stresses imposed by the physical movement along fault planes from large earthquakes typically trigger other earthquakes within two mainshock fault lengths, a triggering process referred to as static triggering (e.g., *Stein et al.*, 1992; *Stein et al.*, 1994; *King et al.*, 1994; *Toda et al.*, 1998; *Parsons et al.*, 1999). Seismic waves originating from large magnitude earthquakes ($M \geq 7$) can also trigger small earthquakes and tremor at remote distances (larger

than two fault lengths) from the mainshock location, which is referred to as dynamic or remote triggering (e.g., *Hill et al*., 1993; *Brodsky et al*., 2000; *Kilb et al*., 2000; *Gomberg et al*., 2001, 2004; *Pankow et al*., 2004; *West et al*., 2005; *Velasco et al*., 2008; *Guilhem et al*., 2010; *Parsons et al*., 2012; *Chao et al*., 2012; *Prejean & Hill*, 2018). Although dynamic and static triggering have been studied extensively, little consensus exists on the exact mechanisms behind dynamic triggering (*Kane et al.,* 2007; *Hill & Prejean*, 2015; *Brodsky & van der Elst*, 2014).

Dynamically triggered seismic events can occur either instantaneously during the passage of seismic waves (instantaneous triggering) or after the passage of the seismic wave (delayed triggering). Instantaneous triggering of other phenomena, such as non-volcanic tremor, has been documented beneath locked sections of faults (e.g., *Chao et al*., 2013). Delayed dynamic triggering has been proposed in regions of induced seismicity related to deep wastewater injection (*van der Elst et al*., 2013). Deciphering the stress needed to trigger earthquakes can reveal the current state of stress of faults in natural and anthropegenic (induced) tectonic settings, the potential for triggering large events, and a basic understanding of fault dynamics and interactions. Our goal here is to explore to what extent remote dynamic triggering occurs in the CGF and what physical mechanisms controls dynamic triggering in the region.

We examine the CGF, CA (Figure 1), which is known to be susceptible to dynamic triggering (*Hill et al*., 1993; *Prejean et al*., 2004; *Peng et al*., 2010; *Aiken and Peng*, 2014; *Schoenball, et al.*, 2015, *Zhang et al.,* 2017). The CGF region presents an ideal study site to observe the interaction of dynamic stresses produced by $M \geq 7$ earthquakes and the local stress field, since the regional broadband and short period networks have been operational for 13 years (*Hutton and Hauksson*, 2010). We select data 5 hours before and 5 hours after the origin times for 211 $M \geq 7$ earthquakes at stations from the EarthScope Transportable Array (TA) and the Southern California Seismic Network (CI) over a thirteen-year period (2004-2016). We use an optimized detection

algorithm to detect high frequency signals (*Velasco et al.,* 2016), and visually inspect these signals to identify earthquakes. All newly identified earthquakes are added to existing catalogs. These catalogs are then used to identify statistically significant changes in detection rates assuming a Poissonian distribution (*Velasco et al.,* 2008; *Linville et al*., 2014).

2 THE COSO GEOTHERMAL FIELD, CALIFORNIA

The CGF, located east of the Sierra Nevada Mountains between Owens Valley and the Garlock fault in southern California, lies within the present-day Basin and Range province (Figure 1). The CGF sits above a shallow heat source (presumed to be a partially molten magma body) and is one of the most seismically active regions in California (*Schoenball, et al.*, 2015). The CGF is a highly-fractured, trans-tensional region (*Davatzes and Hickman*, 2006) exhibiting both strike-slip and normal faulting.

Faults within the CGF can be divided into two groups: 1) WNW striking dextral strike slip faults and minor NE trending faults with sinistral strike-slip motion (*Duffield et al*., 1980; *Roquemore*, 1980) that are relatively inactive (*Davatzes and Hickman*, 2006) and 2) more active N to NNE striking normal faults that dip both west and east (*Davatzes and Hickman*, 2006) (Figure 1). *Davatzes and Hickman* (2006) identify the most prominent of these fault systems in the CGF to be the Coso Wash normal fault, which coincides with the eastern margin of the geothermal field. The Coso Wash fault is composed of several *en-echelon* NNE- SSW trending segments variably connected by NW- striking normal faults (*Davatzes and Hickman*, 2006). Based on previous studies of geomorphic expression, offset hydrothermal deposits and basalt flow, *Davatzes and Hickman* (2006) interpret these faults to be actively slipping.

3 DATA AND METHOD

We investigate remote triggering at the CGF and the surrounding region using a tuned Short Term Average over Long Term Average (STA/LTA) detection algorithm (*Velasco et al*.,

2016) using waveform data from the EarthScope Transportable Array (TA) and the Southern California Seismic Network (CI network), and catalog earthquake data from the Southern California Seismic Network (SCSN) (last accessed Nov. 2018, http://scedc.caltech.edu). We obtained seismograms from 39 stations within the CGF and surrounding region. For each of our 211 M≥7 mainshocks, we collect 10 hours of data (5 hours before and after the mainshock) bracketing the origin time of 211 $M \geq 7$ earthquakes over a thirteen-year period (2004-2016). We create individual waveform databases for each of our 211 mainshocks using the Boulder Real Times Technologies Antelope software. We apply a 4s/40s STA/LTA detection algorithm to three-component high-passed (5 Hz) filtered data, and flag detections that occur on at least 2 of the 3 components (Figure S1) (method Ev1 from *Velasco et. al*, 2016). This approach, requiring a detection on not just one, but two components, significantly reduces the detection of spurious non-seismic sources (*Velasco et. al*, 2016).

We next visually inspect each of the detections within our 2,110 hours of waveform data (10-hours for each of our 211 mainshocks) to identify uncatalogued local earthquakes in the CGF region (Figure 1). For the same time period and geographic region, there are 653 events in the SCSN catalog, and from our visual inspection we were able to identify an additional 181 earthquakes, bringing the total augmented catalog to 834 events.

4 Assessing Remote triggering in the Coso Geothermal Field (CGF) Region

4.1 Triggering Results

We calculate the probability of increased seismicity rates by comparing the number of local earthquakes expected in a 5-hour window to the number of events in the 5-hour window following the arrival of the *P*-wave from the teleseismic mainshock. We assume that earthquakes occur independently (randomly) at a constant rate, following a Poissonian

distribution (*Shearer and Stark*, 2012). We categorize seismic triggering as: 1) instantaneous if the increase in number of events begins in the wavetrain of the mainshock and 2) delayed if there is an increase in number of events after the wavetrain but within 5 hours of the initial mainshock.

To determine statistical significance, we follow what is expected for a Poisson distribution and compare the number of expected events in a 5-hour window to the number of events in the post 5-hour window (*Npost*). In past studies (Velasco et al., 2008; Linville et al., 2014), the number of expected events was set equal to the number of events in the 5-hour window before the *P*-arrival (*Npre*) and significance was determined by assuming that the Poisson distribution approximates a Gaussian distribution (Taylor, 1982). Two weaknesses of this past approach are (1) *Npre* was assumed to be equal to the average background rate and (2) even when the rate was small, a Gaussian distribution was used to determine the significance in the rate change.

To improve on these past studies, we assumed the background rate within a 5-hour window is equivalent to the average of the *Npre* values from our 211 mainshocks. We set this average to be the expected number of events, or μ, within a 5-hour window. To determine significant changes in rates, we calculate the Poisson probability of getting *Npost* events (ν) given the expected number of events (μ).

$$P_\mu(\nu) = e^{-\mu}\frac{\mu^\nu}{\nu!} \quad (1)$$

For the 211 mainshocks in our dataset, the average number of *Npre* (μ) equals 2 (the standard deviation of the mean is also 2). Using this as μ in the probability equation, *Npost* values $\nu > 4$ have < 5% probability of occurring and $\nu > 6$ have < 1% probability of occurring.

Using equation 1, we identify mainshocks that trigger remote aftershock(s) in the CGF with statistical significance. We use a threshold of 5% probability to identify when *Npost* is

significantly above the assume expected background (*Npre*=2). Using this criterion, 37 mainshocks are identified for further analysis (Table S1).

For these 37 events, we next look at the number of *Npre* events to determine if there was already an elevated rate of earthquakes at the time of the mainshock, and then we further compare the rate change between *Npre* and *Npost* (assuming *Npre* equals μ). For the 37 mainshocks, 6 have *Npre* values greater than 4 indicating an elevated rate of events at the time of the mainshock. Of these, we conclude that 4 are probably associated with dynamic triggering because the probability of the rate change between *Npre* and *Npost* < 1.5%. For the other two events, one does not show a significant increase in the *Npre to Npost* events, and the other has a decrease in events following the mainshock. There are also 3 mainshocks where *Npre* is within 1 standard deviation of the 211 event *Npre* mean (i.e., 2). For these, we also test *Npre* as μ and calculate the probability of the change in rate between *Npre* and *Npost*. All three cases exceed a 5% chance of occurring and we exclude them from the triggering catalog. Based on a statistically significant change in earthquake rate at the time of the mainshock 32 of the 37 identified events dynamically triggered aftershocks in the CGF.

In addition to looking at statistically significant changes in earthquake rates, we also identify mainshocks that have local earthquakes embedded within the surface waves. While it is difficult to rule out that these events might have occurred by chance, the coincidence with the timing of the surface waves warrants additional analysis. We identify 9 mainshocks that had local earthquakes occurring during the passage of the surface wave (with no statistically significant seismicity rate increase) and report them as special cases (Table S1). Counting these 9 mainshocks as also triggering brings us to 41 (19%) remote triggering mainshocks. These 41

events have moment magnitudes ranging from 7.0 to 8.8 and depths 10 to 598 km (35 mainshocks 0-200 km, 2 mainshocks 200-439 km, 5 mainshocks 440-600 km).

4.2 Identifying Instantaneous and Delayed Triggering in the CGF

Of our 41 triggering mainshocks, 28 instantaneously triggered local seismicity, of which the majority of the triggering occurred within the wavetrain of the passing surface waves (Figure S1). Of the 28 cases of observed instantaneous triggering, 13 (46%) show no seismic activity in the CGF or its vicinity in the 5-hours prior to the mainshock seismic waves. The remaining 13 mainshocks are classified as delayed triggering events, where the triggered seismicity occurred within 5-hours of the P-wave, but after the passage of the mainshock energy (Figure S1). Of the 13 delayed triggering events, 7 (54%) show no activity in the 5-hours prior to passage of the mainshock seismic waves.

We identify 311 local events ranging in magnitude (M_L) 0.02-3.45 triggered within 5-hours following 41 mainshock earthquakes ($M_W \geq 7.0$). Of the 311 local events, we identify 181 events that had not been previously cataloged, the remaining 130 events were included in the SCSN catalog (Figure 2). All events reported here have been visually reviewed.

A 2010 July 18 13:04:11 UTC *M* 6.9 mainshock in the New Britain Region, Papua New Guinea, instantaneously triggered seismicity in the CGF during the Rayleigh waves. We include this event in Table S1, even though it was below the $M \geq 7$ magnitude threshold. This event occurred ~30 minutes prior to a magnitude 7.3 mainshock also located in the New Britain, Papua New Guinea region. The local seismicity rate had decreased before the arrival of the *M* 7.3 mainshock, but then increased again following this larger event. The *M* 6.9 mainshock in Table S1 is excluded from further analysis.

4.3 Factors Contributing to Remote Dynamic Triggering in the CGF

To investigate the physical mechanisms involved in dynamic triggering, we explore a suite of different factors including focal mechanism, depth, peak dynamic stress, and orientation of the incoming seismic waves (Table S1, Figure S2, and Figure 3). Many of our 211 mainshocks are concentrated near the western edge of the Pacific Plate, a naturally more seismically active region (Figure S3). The mainshock focal mechanisms are diverse, showing normal, strike-slip, thrust, transpression, transtension mechanisms, for 42, 33, 111, 11, 14 events, respectively. There is no obvious preference for one type of mainshock mechanisms to promote triggering more than another, and each of the three mechanism types are associated with both instantaneous and delayed triggering (Table S1). We, thus, do not attribute mainshock focal mechanism as a preferential trigger mechanism specific to the CGF region. There is also no obvious correlation between depth and triggering (Figure S2b).

We next compute the mainshock generated peak dynamic stress (PDS) at five seismic stations (TA-HELL, CI-MPM, CI-CWC, CI-SLA, CI-CLC), the stations that were recording data during the time range of this study. To compute PDS, we estimate peak vector velocities using three-component broadband data and multiply by the shear modulus/Love wave group velocity (shear modulus = 33,000 MPa, Love wave group velocity = 3.5 km/s) (*Pankow et al*., 2004; *Velasco et al*., 2004). We average the derived PDS obtained for all five stations to determine a single PDS value for each mainshock. In this way, we can examine the average PDS values as a function of mainshock magnitude, depth, and back-azimuth for each triggering and non-triggering mainshock (Table S1 and Figure S2 & 3). The average PDS values, for both non-triggering mainshocks and triggering mainshocks (Figure S2a) range between values of (10^{-4}-10^{-1} MPa). As expected, the general trend shows that larger magnitude mainshocks produce

larger PDS values. Several Mw 7-7.5 mainshocks deviate from this trend, producing PDS values as high as 0.12 MPa, a value more consistent with a magnitude 9 mainshock. These high PDS values could result from surface wave directivity effects (e.g., *Velasco et al*., 2004). The highest PDS value found was ~0.2 MPa for non-triggering events and ~0.027MPa for triggering events. The lowest PDS for a triggering event is ~0.0002MPa a small value implying relatively weak triggering; however, the value is consistent with the findings of *Aiken and Peng* (2014), who indicate geothermal sites in California are susceptible to a triggering threshold of ≤ 0.001 MPa.

Finally, we investigate the relationship between the local stress field (maximum horizontal stress) and orientation of the incoming surface waves (Figure 3). Back-azimuth orientations are calculated from each mainshock to the receiver station MPM (Table S1). To increase the data density, we map the back-azimuth orientations, resulting in orientations ranging from 0°-180° (Figure S3). We separate these back-azimuths into delayed and instantaneous triggering categories, and further divide the instantaneous triggered events into triggering phases (S, Love, and Rayleigh waves). We calculate and compare the mean and standard deviation of the delayed and instantaneous back-azimuths. We find back azimuths of the instantaneous triggering occurs mainly over a narrow band: ~89° ±11° (approx. E-W) and delayed triggering occurs over a similar range ~81° ±21° (Figure 3). The azimuthal orientation of the non-triggering mainshocks, differ, occurring over a wide range of azimuths (3°-178°.)

5 DISCUSSION

5.1 Instantaneous Triggering

Of the 311 locally triggered earthquakes 57 events were instantaneously triggered. Most of these instantaneously triggered events occurred during the Rayleigh wavetrain (47), while three occurred during the S-wave passage and seven during the Love-wave passage. Cases of

local earthquakes triggered by the onset of Love-wave and Rayleigh-wave arrivals are likely consistent with failure by the Coulomb failure criteria (*Kilb et al*., 2002; *Peng and Chao*, 2008; *Hill*, 2008; *Peng et al*. 2008, 2009, 2010; *Gonzalaz-Huizar and Velasco*, 2010). Additionally, Rayleigh waves can trigger events by inducing fluid excitation and changing the pore-fluid pressures (*Rubinstein et al*. 2007, 2009; *Hill* 2008; *Miyazawa et al*. 2008; *Peng and Chao*, 2008; *Peng et al*., 2009, 2010).

Examining the back-azimuth angles of our triggering mainshocks and find a narrow range of azimuths in which instantaneous triggering events (63°- 123° back azimuths), and delayed triggered events (73°- 98° back azimuths, with the exception of one event at 13°) occur. Analyzing stress data taken from *Heidbach et al.* (2010), we observe two prominent directions of maximum horizontal stress that exist within our study area. On average, these directions are oriented at 175° and 16° (Figure 3 and 4). Back-azimuth angles indicate the orientation of seismic arrival phases at 89° ±11 for instantaneous triggering and 81° ±21 for delayed triggering, approximately perpendicular to the direction of the local stress field (Figure 3 and 4) (*Heidbach et al.,* 2008).

Our results indicate that dynamic triggering in the CGF is highly dependent on the orientation of the mainshocks seismic wave propagation direction with respect to the local stress field and the orientation of local strike slip and normal faults (Figure 3 and 4). If we consider the particle motion of a Rayleigh wave propagating in a direction perpendicular to faulting and the maximum horizontal stress; the displacement field across a normal fault will promote the unclamping of stress, and reduce the normal stress on the fault. The sudden change in normal stress will result in a response of increased shear stress on the fault. In the case of a Love wave propagating in a direction perpendicular to the strike of a strike slip fault, the wave will displace

particles in a motion perpendicular to the strike of the fault and impart positive stress (*Tape et al., 2013*), increasing shear stress across the fault. In both cases, the imposed transient stresses cause an increase in shear stress within the system, in turn driving fault slip. The unique position of CGF, its local stress field, and faulting patterns is optimally oriented to host remotely triggered earthquakes caused by large earthquakes from the Western Pacific.

5.2 Delayed Triggering

31% of our triggering mainshocks have a time delay, such that the local earthquakes occur after the passage of the remote mainshock seismic waves (e.g., *Gonzalez-Huizar et al.*, 2012; *Jagla*, 2011; *Morton and Bilek*, 2014; *Peng et al.*, 2010; *van der Elst et al.*, 2013). There have been a number of triggering mechanisms proposed to explain these delays including: the excitation of crustal fluids (e.g., *Hill and Prejean*, 2015 and references therein), a change in frictional contact along a fault (*Parsons*, 2005), arrival of multiple surfaces waves circling the Earth (*Peng et al.*, 2011), pore fluid diffusion, and transient pore-pressure changes (*Brodsky et al.*, 2003; *Brodsky and Prejean*, 2005; *Bodin and Gomberg*, 1994; *Brodsky*, 2006; *Syracuse et al.*, 2010). *Parsons et al.* (2017) found that delay times even appear to correlate with magnitude of triggered earthquakes, as fluid needs to diffuse across a locked fault asperity before failure.

A combination of these mechanisms may incite a delay in the triggered response in the CGF region. Delay times related to this process specifically in seismically active geothermal areas such as the CGF can be short (seconds-minutes-hours) as the distance between pockets of elevated pore-pressure and adjacent faults is short (*Prejean and Hill*, 2018). Our delayed triggering results are likely most consistent with the excitation of crustal fluids, pore fluid diffusion, transient pore-pressure, and changes in frictional contact. In this case, fluids associated with the shallow heat source of the CGF region may migrate after the passage of the mainshock

generated transient wavetrain, eventually triggering local seismicity. The normal stress and strength of a fault may be reduced by these processes promoting failure by shear stresses.

5.3 Previous studies in the Coso Geothermal Field

Using a different approach, observations, and study region, *Aiken and Peng* (2014) also examined dynamic triggering in the CGF. Their study and ours both identify the 02/27/2010 M=8.8, Chile, earthquake as instantaneously triggering local events in the CGF. While our method can identify more triggered events than *Aiken and Peng* (2014), there are five events they identified as triggering (Table S2) that we do not. We attribute these deviations to differences in our study areas. Our region encompasses ~15,000 km^2 whereas theirs encompasses ~400 km^2. Our results diverge from those of *Aiken and Peng* (2014) since we account for seismic activity in both pre- and post 5-hour windows far beyond the extent of the CGF. Given the active exploitation (three geothermal power plants locations) in the region, many of the events in the CGF are assumed to be induced (*Schoenball et al*., 2015), and this anthropogenic activity may alter the natural stress state of the CGF. *Zhang et al*. (2017) observed that geothermal production wells can affect subsurface facture networks in a manner that can actually increase the likelihood of dynamic triggering in a region surrounding the anthropogenic footprint of the production wells, where pore pressure gradients may be higher. We find the majority of dynamic triggering occurs in the areas outside of the geothermal plants (Figure 2) consistent with observations of *Zhang et al*. (2017).

6 Conclusion

In this study, we investigated the capability of 211 global mainshocks M ≥ 7 (depths 8 to 664 km) to trigger remote seismicity in the CGF region. We find 41 cases of local triggering, both instantaneous (28 mainshocks) and delayed (13 mainshocks) within 5 hours of the mainshock passage. These 41 trigging mainshocks, produced 311 locally triggered earthquakes of which 57 are considered instantaneously triggered (within the wavetrain of the mainshock; Figure S2), 3 are coincident with the arrival of the *S*-phase, 7 with the Love wave, and 47 with

the passage of the Rayleigh wave. The remaining 268 triggered events have delayed triggering, occurring after the passage of the mainshock seismic waves but within 5 hours of the mainshock.

We find no correlation between mainshock depth and triggering, no obvious indication that larger PDS are more likely to trigger events in the CGF, nor evidence that a specific mainshock focal mechanism type routinely causes triggering in the CGF. However, the similarity of the triggering mainshock's back-azimuths indicate dynamic triggering is highly dependent on the dynamic stresses aligning favorably with the local stress field (maximum horizontal stress). Instantaneously triggered events have a narrow back-azimuth range (89°±11°), which aligns approximately perpendicular to the study area's dominant stress directions. Events related to delayed triggering in the region exhibit a slightly wider range of back-azimuth dependence (81° ±21°). For the instantaneous triggering cases, the orientation (back-azimuth) of the incoming seismic waves in relation to the local stress field does enhance triggering in the CGF region. We find that seismicity in the CGF region is more likely to be triggered by Love and Rayleigh waves arriving approximately perpendicular to the average local stress orientation. The stress field and orientation of normal and strike slip faults in the region align perfectly with the transient stresses of large earthquakes originating from azimuths at ~89°. The unique position of the CGF, the local stress field, and faulting orientation is optimally oriented to slip under stresses imparted by earthquakes from the Western Pacific.

Table S1.2 Parameters for 41 M ≥ 7 triggering mainshocks. We compute distance and back-azimuth, with respect to SCSN CI-Network Code station MPM (36.06 N, -117.49 E) located ~30 km from the centroid of the Coso Geothermal Field (36.03N, -117.82E). We calculate the average mainshock generated peak dynamic stress (PDS) at five seismic stations (TA-HELL, CI-MPM, CI-CWC, CI-SLA, CI-CLC). PDS values are an average of the PDS from all five stations. The table also lists if the locally triggered seismicity is assumed to be consistent with triggering that is instantaneous or delayed. We indicate which phase(s) (S=S-Wave, G=Love Wave, R=Rayleigh Wave) of the mainshock wavetrain best correlate with the times of the triggered local events.

Date	mag	depth	Back-Az wrap-ped	pds	Region	Trig Type	Trig Phase	N-pre	N-post	Mechanism	Special Case
2/27/10	8.8	22.9	124	0.0271	Chile	Instant	S,G	2	14	Normal	N
11/7/12	7.4	24	63	0.0143	Guatemala	Instant	G	1	7	Thrust	N
4/1/14	8.2	25	107	0.0084	Chile	Instant	R	1	8	Thrust	N
4/16/16	7.8	20.59	90	0.0059	Ecuador	Instant	S,R	0	13	Thrust	N
5/5/15	7.5	55	90	0.0055	Papua New Guinea	Instant	R	8	19	Thrust	N
12/23/04	8.1	10	83	0.0045	Macquarie Island	Instant	R	1	5	Strike-Slip	N
12/21/10	7.4	14	86	0.0023	Japan	Instant	R	1	9	Transtension	N
12/7/12	7.3	31	85	0.0020	Japan	Instant	R	10	20	Thrust	N
4/6/10	7.8	31	87	0.0018	Indonesia	Instant	R	*0*	9	Thrust	N
1/3/09	7.4	23	90	0.0018	Indonesia	Instant	G, R	*0*	5	Thrust	N
5/23/13	7.4	173.7	77	0.0012	Tonga	Instant	S,R	0	6	Normal	N
8/20/11	7.2	32	85	0.0009	Vanuatu	Instant	R	*0*	9	Thrust	N
1/3/10	7.1	10	89	0.0008	Solomon Islands	Instant	R	1	6	Thrust	N
7/15/04	7.1	565.5	81	0.0008	Fiji region	Instant	G	2	7	Thrust	N
7/17/06	7.7	20	99	0.0005	Indonesia	Instant	R	*0*	9	Thrust	N
11/15/14	7.1	45	89	0.0004	Indonesia	Instant	R	0	6	Thrust	N

4/6/13	7	66	91	0.0004	Indonesia	Instant	R	7	13	Normal	N
12/10/12	7.1	155	93	0.0003	Banda Sea	Instant	G,R	6	27	Transpression	N
2/27/15	7	552.1	94	0.0002	Indonesia	Instant	R	1	6	Transtension	N
5/24/13	8.3	598.1	91	0.0112	Sea of Okhotsk	Delay	--	0	8	Normal	N
7/6/11	7.6	17	73	0.0064	Kermadec Islands	Delay	--	1	6	Normal	N
5/30/15	7.8	664	84	0.0033	Japan	Delay	--	1	6	Normal	N
12/17/16	7.9	94.54	90	0.0032	Papua New Guinea	Delay	--	0	5	Thrust	N
8/31/12	7.6	28	85	0.0031	Philippine Islands	Delay	--	0	5	Transpression	N
4/19/14	7.5	43.37	90	0.0023	Papua New Guinea	Delay	--	1	5	Thrust	N
2/13/15	7.1	16.68	87	0.0022	Mid-Atlantic Ridge	Delay	--	2	9	Strike-Slip	N
10/26/15	7.5	231	13	0.0010	Afghanistan	Delay	--	1	6	Thrust	N
4/28/16	7	24	86	0.0008	Vanuatu	Delay	--	0	5	Thrust	N
8/9/09	7.1	292	82	0.0008	Japan	Delay		0	8	Thrust	N
8/24/11	7	147	98	0.0006	Peru	Delay	--	0	7	Normal	N
10/20/15	7.1	135	86	0.0006	Vanuatu	Delay	--	0	10	Transpression	N
7/15/13	7.3	11	88	0.0005	Bristol Island	Delay	--	1	5	Strike-Slip	N
11/26/04	7.1	10	91	0.0007	Indonesia	Instant	G	1	4	Transtension	Y
1/2/06	7.2	582.9	85	0.0006	Sandwich Islands	Instant	G, R	0	3	Normal	Y
9/12/07	7.9	35	96	0.0036	Indonesia	Instant	R	0	2	Thrust	Y
9/12/07	8.4	34	93	0.0058	Indonesia	Instant	R	0	2	Thrust	Y
4/12/08	7.1	16	85	0.0008	Macquarie Island	Instant	R	0	3	Thrust	Y
6/30/08	7	8	85	0.0002	Sandwich Islands	Instant	R	0	2	Strike-Slip	Y
2/11/09	7.2	20	88	0.0010	Indonesia	Instant	R	1	3	Thrust	Y
7/18/10	7.3	35	90	0.0015	Papua New Guinea	Instant	G, R	3	6	Thrust	Y
7/18/10	6.9				Papua New Guinea	Instant	R			Thrust	Y
9/1/16	7	19	73	0.0006	New Zealand	Instant	R	0	4	Normal	Y

Table S2.2 List of 211 M ≥ 7 mainshocks and associated parameters. We compute distance and back-azimuth, with respect to SCSN CI-Network Code station MPM (36.06 N, -117.49 E) located ~30 km from the centroid of the Coso Geothermal Field (36.03N, -117.82E). We calculate the average mainshock generated peak dynamic stress (PDS) at five seismic stations (TA-HELL, CI-MPM, CI-CWC, CI-SLA, CI-CLC). PDS values are an average of the PDS from all five stations.

Date	Origin Time	lat	lon	mag	depth	distance	BAZ wrapped	pds	Npre	Npost
1/3/04	16:23:21	-22.253	169.683	7.1	22	8252	83.4	0.001	3	2
2/5/04	21:05:03	-3.615	135.538	7	16.6	11904	91.1	3.586	3	2
2/7/04	02:42:35	-4.003	135.023	7.3	10	11961	91.3	0.001	2	4
7/15/04	04:27:15	-17.656	-178.76	7.1	565.5	6982	80.6	0.001	2	7
7/25/04	14:35:19	-2.427	103.981	7.3	582.1	15415	92.7	0.001	5	6
9/5/04	14:57:19	33.184	137.071	7.4	10	11455	81.4	0.002	0	0
9/5/04	10:07:08	33.07	136.618	7.2	14	11499	81.2	0.001	2	0
10/9/04	21:26:54	11.422	-86.665	7	35	3635	71.8	0.003	0	0
11/11/04	21:26:41	-8.152	124.868	7.5	10	13063	94.2	0.001	0	0
11/15/04	09:06:57	4.695	-77.508	7.2	15	4476	84.5	0.002	1	2
11/22/04	20:26:24	-46.676	164.721	7.1	10	9087	81.1	0.001	0	1
11/26/04	02:25:03	-3.609	135.404	7.1	10	11919	91.1	0.001	1	4
11/28/04	18:32:14	43.006	145.119	7	39	10622	85.0	0.001	1	1
12/23/04	14:59:04	-49.312	161.345	8.1	10	9377	83.3	0.005	1	5
12/26/04	00:58:53	3.295	95.982	9.1	30	16296	85.1	0.026	11	1
12/26/04	04:21:30	6.91	92.958	7.2	39.2	16571	78.5	0.001	1	0
2/5/05	12:23:19	5.293	123.337	7.1	525	13252	87.1	0.000	2	4
3/2/05	10:42:12	-6.527	129.933	7.1	201.7	12515	92.7	0.000	2	0
3/28/05	16:09:37	2.085	97.108	8.6	30	16180	87.0	0.007	0	0
6/13/05	22:44:34	-19.987	-69.197	7.8	115.6	5707	106.8	0.005	2	0

6/15/05	02:50:54	41.292	-125.953	7.2	16	4654	167.2	0.045	2	0
7/24/05	15:42:06	7.92	92.19	7.2	16	16630	76.5	0.001	1	1
8/16/05	02:46:28	38.276	142.039	7.2	36	10934	83.5	0.001	2	1
9/9/05	07:26:44	-4.539	153.474	7.6	90	9912	89.9	0.002	2	1
9/26/05	01:55:38	-5.678	-76.398	7.5	115	4610	96.4	0.002	12	8
10/8/05	03:50:41	34.539	73.588	7.6	26	16042	19.1	0.003	1	1
11/14/05	21:38:51	38.107	144.896	7	11	10687	85.3	0.001	0	1
1/2/06	22:13:40	-60.957	-21.606	7.4	13	10338	84.9	0.001	0	3
1/2/06	06:10:50	-19.926	-178.178	7.2	582.9	6966	79.2	0.001	1	0
1/27/06	16:58:54	-5.473	128.131	7.6	397	12720	92.5	0.001	5	1
2/22/06	22:19:08	-21.324	33.583	7	11	16107	56.8	0.001	3	0
4/20/06	23:25:02	60.949	167.089	7.6	22	9233	102.8	0.006	2	0
5/3/06	15:26:40	-20.187	-174.123	8	55	6556	77.3	0.007	1	3
5/16/06	10:39:23	-31.81	-179.307	7.4	152	7380	74.3	0.003	1	0
7/17/06	08:19:27	-9.284	107.419	7.7	20	14956	99.1	0.001	0	9
8/20/06	03:41:48	-61.029	-34.371	7	13	9647	96.0	0.001	1	3
11/15/06	11:14:14	46.592	153.266	8.3	10	9961	90.5	0.008	0	0
12/26/06	12:26:21	21.799	120.547	7.1	10	13300	77.0	0.001	1	1
1/13/07	04:23:21	46.243	154.524	8.1	10	9863	91.4	0.014	3	0
1/21/07	11:27:45	1.065	126.282	7.5	22	12938	89.5	0.001	2	2
3/25/07	00:40:02	-20.617	169.357	7.1	34	8265	83.9	0.001	1	0
4/1/07	20:39:59	-8.466	157.043	8.1	24	9520	89.3	0.004	2	0
8/1/07	17:08:51	-15.595	167.68	7.2	120	8393	85.9	0.001	3	1
8/8/07	17:05:05	-5.859	107.419	7.5	280	15006	95.8	0.001	1	0
8/15/07	23:40:58	-13.386	-76.603	8	39	4746	104.9	0.007	1	0
9/2/07	01:05:18	-11.61	165.762	7.2	35	8574	87.3	0.002	4	0
9/12/07	23:49:04	-4.438	101.367	8.4	34	15689	95.5	0.004	0	2
9/12/07	11:10:27	-2.625	100.841	7.9	35	15762	93.3	0.006	0	2
9/13/07	03:35:29	-2.13	99.627	7	22	15900	92.8	0.000	0	0
9/28/07	13:38:58	22.013	142.668	7.5	260	11035	86.3	0.003	0	0

9/30/07	05:23:34	-49.271	164.115	7.4	10	9176	81.2	0.001	0	0
10/31/07	03:30:16	18.9	145.388	7.2	207	10769	87.7	0.001	0	0
11/14/07	15:40:51	-22.247	-69.89	7.7	40	5715	109.0	0.003	9	2
11/29/07	19:00:20	14.944	-61.274	7.4	156	6399	80.3	0.002	0	1
12/9/07	07:28:21	-25.996	-177.514	7.8	152.5	7044	75.9	0.003	2	0
12/19/07	09:30:28	51.36	-179.509	7.2	34	8114	112.5	0.002	1	1
2/20/08	08:08:31	2.768	95.964	7.4	26	16303	85.8	0.001	4	1
2/25/08	08:36:33	-2.486	99.972	7.2	25	15860	93.2	0.001	2	0
3/20/08	22:32:58	35.49	81.467	7.2	10	15642	30.7	0.001	1	0
4/9/08	12:46:13	-20.071	168.892	7.3	33	8307	84.3	0.001	2	1
4/12/08	00:30:13	-55.664	158.453	7.1	16	9644	85.1	0.001	0	3
5/12/08	06:28:02	31.002	103.322	7.9	19	14531	59.3	0.006	0	0
6/30/08	06:17:43	-58.227	-22.099	7	8	10336	85.4	0.000	0	2
7/5/08	02:12:04	53.882	152.886	7.7	632.8	9994	90.3	0.003	1	0
7/19/08	02:39:29	37.552	142.214	7	22	10928	83.7	0.000	2	0
9/29/08	15:19:32	-29.756	-177.683	7	36	7168	74.2	0.000	1	1
11/16/08	17:02:33	1.271	122.091	7.4	30	13404	89.3	0.000	0	0
11/24/08	09:02:59	54.203	154.322	7.3	492.3	9900	91.5	0.001	11	3
1/3/09	22:33:40	-0.691	133.305	7.4	23	12157	90.2	0.002	0	5
1/3/09	19:43:51	-0.414	132.885	7.7	17	12204	90.1	0.002	1	1
1/15/09	17:49:39	46.857	155.154	7.4	36	9817	91.9	0.003	1	0
2/11/09	17:34:50	3.886	126.387	7.2	20	12920	88.1	0.001	1	3
2/18/09	21:53:45	-27.424	-176.33	7	25	6971	74.5	0.001	0	1
3/19/09	18:17:40	-23.043	-174.66	7.6	31	6684	75.9	0.003	0	0
5/28/09	08:24:47	16.731	-86.217	7.3	19	3898	64.8	0.011	4	2
7/15/09	09:22:29	-45.762	166.562	7.8	12	8929	79.9	0.003	2	0
8/9/09	10:55:55	33.167	137.944	7.1	292	11375	81.9	0.001	0	8
8/10/09	19:55:39	14.099	92.902	7.5	24	16344	67.6	0.001	2	0
9/2/09	07:55:01	-7.782	107.297	7	46	14994	97.7	0.000	4	2
9/29/09	17:48:11	-15.489	-172.095	8.1	18	6240	79.3	0.021	0	2

9/30/09	10:16:09	-0.72	99.867	7.6	81	15879	90.9	0.001	1	1
10/7/09	22:18:51	-12.517	166.382	7.8	35	8512	87.0	0.006	7	1
10/7/09	22:03:14	-13.006	166.51	7.7	45	8501	86.8	0.006	7	1
10/7/09	23:13:48	-13.093	166.497	7.4	31.1	8503	86.8	0.003	7	1
11/9/09	10:44:55	-17.239	178.331	7.3	595	7281	81.9	0.001	2	4
1/3/10	22:36:26	-8.783	157.354	7.1	10	9486	89.3	0.001	1	6
1/12/10	21:53:10	18.443	-72.571	7	13	5317	72.5	0.012	2	2
2/26/10	20:31:27	25.93	128.425	7	25	12419	79.0	0.000	1	2
2/27/10	08:01:23	-36.122	-72.898	8.8	22.9	6099	120.8	0.004	2	14
2/27/10	06:34:12	-37.773	-75.048	7.4	35	6035	123.7	0.027	5	3
3/11/10	14:55:28	-34.326	-71.799	7	18	6087	118.7	0.001	0	0
4/4/10	22:40:42	32.2861	-115.2953	7.2	9.987	3582	04.1	0.238	1	0
4/6/10	22:15:02	2.383	97.048	7.8	31	16185	86.6	0.002	0	9
5/9/10	05:59:42	3.748	96.018	7.2	38	16287	84.4	0.000	2	2
5/27/10	17:14:47	-13.698	166.643	7.2	31	8491	86.6	0.001	3	2
6/12/10	19:26:50	7.881	91.936	7.5	35	16658	76.4	0.002	0	0
6/16/10	03:16:28	-2.174	136.543	7	18	11795	90.6	0.001	2	0
7/18/10	13:34:59	-5.931	150.59	7.3	35	10232	90.2	0.001	3	6
7/23/10	22:51:12	6.497	123.48	7.6	578	13228	86.4	0.002	3	0
7/23/10	22:08:11	6.718	123.409	7.3	607.1	13234	86.3	0.002	3	0
7/23/10	23:15:10	6.776	123.259	7.5	640.6	13251	86.2	0.002	3	0
8/4/10	22:01:44	-5.746	150.765	7	44	10212	90.2	0.000	1	1
8/10/10	05:23:45	-17.541	168.069	7.3	25	8368	85.2	0.001	5	2
8/12/10	11:54:16	-1.266	-77.306	7.1	206.7	4475	91.5	0.000	5	2
9/3/10	16:35:48	-43.522	171.83	7	12	8469	76.5	0.001	1	1
9/29/10	17:11:26	-4.963	133.76	7	26	12098	91.7	0.000	1	1
10/25/10	14:42:22	-3.487	100.082	7.8	20.1	15840	94.5	0.001	2	0
12/21/10	17:19:41	26.901	143.698	7.4	14	10894	86.0	0.002	1	9
12/25/10	13:16:37	-19.702	167.947	7.3	16	8402	84.7	0.002	4	3
1/1/11	09:56:58	-26.803	-63.136	7	576.8	6524	107.8	0.001	1	0

1/2/11	20:20:18	-38.355	-73.326	7.2	24	6197	122.5	0.001	1	1
1/13/11	16:16:42	-20.628	168.471	7	9	8357	84.3	0.001	0	2
1/18/11	20:23:23	28.777	63.951	7.2	68	16849	03.0	0.001	0	0
3/9/11	02:45:20	38.435	142.842	7.3	32	10863	84.0	0.001	2	1
3/11/11	06:25:50	38.058	144.59	7.7	18.6	10714	85.1	0.019	0	0
3/11/11	05:46:24	38.297	142.373	9.1	29	10905	83.7	0.026	3	0
3/11/11	06:15:40	36.281	141.111	7.9	42.6	11042	83.2	0.024	0	0
4/7/11	14:32:43	38.276	141.588	7.1	42	10974	83.2	0.001	8	0
6/24/11	03:09:39	52.05	-171.836	7.3	52	7670	119.4	0.003	0	1
7/6/11	19:03:18	-29.539	-176.34	7.6	17	7036	73.5	0.006	1	6
7/10/11	00:57:11	38.034	143.264	7	23	10830	84.3	0.001	3	0
8/20/11	16:55:03	-18.365	168.143	7.2	32	8368	85.0	0.001	0	9
8/20/11	18:19:24	-18.311	168.218	7.1	28	8360	85.0	0.001	0	1
8/24/11	17:46:12	-7.641	-74.525	7	147	4842	98.1	0.001	0	7
9/3/11	22:55:41	-20.671	169.716	7	185.1	8229	83.8	0.000	1	0
9/15/11	19:31:04	-21.611	-179.528	7.3	644.6	7139	79.0	0.001	2	1
10/21/11	17:57:16	-28.993	-176.238	7.4	33	7010	73.7	0.003	0	4
10/23/11	10:41:23	38.721	43.508	7.1	18	15329	151.1	0.001	2	0
12/14/11	05:04:59	-7.551	146.809	7.1	135	10648	90.7	0.000	1	1
1/10/12	18:36:59	2.433	93.21	7.2	19	16611	85.9	0.000	2	1
2/2/12	13:34:41	-17.827	167.133	7.1	23	8470	85.5	0.001	1	0
3/20/12	18:02:47	16.493	-98.231	7.4	20	2792	51.1	0.039	1	0
3/25/12	22:37:06	-35.2	-72.217	7.1	40.7	6101	119.6	0.001	0	0
4/11/12	08:38:37	2.327	93.063	8.6	20	16628	86.1	0.015	1	1
4/11/12	10:43:11	0.802	92.463	8.2	25.1	16702	88.6	0.006	2	0
4/12/12	07:15:48	28.696	-113.104	7	13	3211	09.1	0.018	2	0
8/14/12	02:59:38	49.8	145.064	7.7	583.2	10555	84.3	0.003	1	1
8/27/12	04:37:19	12.139	-88.59	7.3	28	3463	69.3	0.011	4	0
8/31/12	12:47:33	10.811	126.638	7.6	28	12845	84.8	0.003	0	5
9/5/12	14:42:08	10.085	-85.315	7.6	35	3733	74.5	0.011	2	0

9/30/12	16:31:36	1.929	-76.362	7.3	170	4582	87.8	0.001	2	0
10/28/12	03:04:09	52.788	-132.101	7.8	14	6012	161.8	0.021	4	4
11/7/12	16:35:47	13.988	-91.895	7.4	24	3217	63.4	0.014	1	7
12/7/12	08:18:23	37.89	143.949	7.3	31	10772	84.7	0.002	10	20
12/10/12	16:53:09	-6.533	129.825	7.1	155	12527	92.7	0.000	6	27
1/5/13	08:58:19	55.393	-134.652	7.5	10	6342	159.4	0.020	1	0
2/6/13	01:12:26	-10.799	165.114	8	24	8641	87.6	0.003	3	0
2/6/13	01:54:15	-10.499	165.588	7	8.8	8588	87.6	0.003	3	0
2/6/13	01:23:20	-11.183	164.882	7.1	10	8668	87.6	0.003	3	0
2/8/13	15:26:38	-10.928	166.018	7.1	21	8543	87.4	0.001	4	1
4/6/13	04:42:36	-3.517	138.476	7	66	11578	90.9	0.000	7	13
4/16/13	10:44:20	28.033	61.996	7.7	80	16934	178.9	0.003	1	2
4/19/13	03:05:53	46.221	150.788	7.2	110	10152	88.8	0.001	4	5
5/23/13	17:19:05	-23.009	-177.232	7.4	173.7	6939	77.2	0.001	0	6
5/24/13	05:44:49	54.892	153.221	8.3	598.1	9973	90.6	0.011	0	8
7/7/13	18:35:31	-3.917	153.927	7.3	385.5	9862	89.9	0.001	2	0
7/15/13	14:03:40	-60.857	-25.07	7.3	11	10151	87.9	0.000	1	5
8/30/13	16:25:02	51.537	-175.2297	7	29	7851	116.2	0.001	0	0
9/24/13	11:29:48	26.951	65.5009	7.7	15	17038	06.6	0.004	4	7
9/25/13	16:42:43	-15.838	-74.5112	7.1	40	5036	106.2	0.001	1	1
10/15/13	00:12:32	9.8796	124.1167	7.1	19.04	13129	84.7	0.000	2	0
10/25/13	17:10:20	37.155	144.6611	7.1	35	10716	85.3	0.001	4	0
11/17/13	09:04:56	-60.273	-46.4011	7.7	10	8984	106.5	0.002	1	1
11/25/13	06:27:33	-53.945	-55.0033	7	11.78	8255	112.8	0.000	3	0
4/1/14	23:46:47	-19.609	-70.7691	8.2	25	5537	107.4	0.008	1	8
4/3/14	02:43:13	-20.570	-70.4931	7.7	22.4	5597	108.0	0.003	1	2
4/11/14	07:07:23	-6.5858	155.0485	7.1	60.53	9738	89.7	0.001	2	0
4/12/14	20:14:39	-11.27	162.1481	7.6	22.56	8967	88.1	0.007	0	0
4/13/14	12:36:19	-11.463	162.0511	7.4	39	8978	88.1	0.006	0	4
4/18/14	14:27:25	17.397	-100.9723	7.2	24	2642	44.9	0.017	3	1

4/19/14	13:28:01	-6.7547	155.0241	7.5	43.37	9741	89.7	0.002	1	5
6/23/14	20:53:10	51.8486	178.7352	7.9	109	8248	111.1	0.007	0	0
10/9/14	02:14:31	-32.108	-110.8112	7	16.54	3624	167.5	0.001	1	2
10/14/14	03:51:34	12.5262	-88.1225	7.3	40	3526	69.0	0.002	1	0
11/1/14	18:57:22	-19.690	-177.7587	7.1	434	6918	79.2	0.001	1	4
11/15/14	02:31:42	1.8929	126.5217	7.1	45	12910	89.1	0.000	0	6
2/13/15	18:59:12	52.6487	-31.9016	7.1	16.68	9720	86.5	0.002	2	9
2/27/15	13:45:05	-7.2968	122.5348	7	552.06	13326	94.2	0.000	1	6
3/29/15	23:48:31	-4.7294	152.5623	7.5	41	10013	90.0	0.002	1	0
4/25/15	06:11:26	28.2305	84.7314	7.8	8.22	16116	41.0	0.003	1	0
5/5/15	01:44:06	-5.4624	151.8751	7.5	55	10089	90.1	0.006	8	19
5/7/15	07:10:20	-7.2175	154.5567	7.1	10	9793	89.7	0.001	4	3
5/12/15	07:05:20	27.8087	86.0655	7.3	15	16063	43.2	0.001	1	0
5/30/15	11:23:02	27.8386	140.4931	7.8	664	11202	84.4	0.003	1	6
6/17/15	12:51:33	-35.363	-17.1605	7	10	10957	84.0	0.000	0	0
7/18/15	02:27:34	-10.401	165.1409	7	11	8636	87.7	0.001	1	3
7/27/15	21:41:22	-2.6286	138.5277	7	48	11574	90.6	0.001	1	2
9/16/15	22:54:33	-31.562	-71.4262	7	28.41	5976	116.7	0.011	1	1
9/16/15	23:18:42	-31.573	-71.6744	8.3	22.44	5955	116.9	0.011	1	0
10/20/15	21:52:03	-14.859	167.3028	7.1	135	8428	86.2	0.001	0	10
10/26/15	09:09:43	36.5244	70.3676	7.5	231	15912	13.1	0.001	1	6
11/24/15	22:45:39	-10.537	-70.9437	7.6	606.21	5281	99.8	0.004	0	0
11/24/15	22:50:54	-10.059	-71.0184	7.6	620.56	5264	99.4	0.004	0	0
12/4/15	22:25:00	-47.616	85.0913	7.1	35	14322	150.5	0.000	0	0
12/7/15	07:50:06	38.2107	72.7797	7.2	22	15676	16.4	0.002	1	1
1/24/16	10:30:30	59.6363	-153.4051	7.1	129	7314	139.9	0.002	1	0
1/30/16	03:25:12	53.9776	158.5463	7.2	177	9622	94.9	0.001	0	0
3/2/16	12:49:48	-4.9521	94.3299	7.8	24	16458	97.9	0.002	2	0
4/15/16	16:25:06	32.7906	130.7543	7	10	12044	77.9	0.001	0	0
4/16/16	23:58:37	0.3819	-79.9218	7.8	20.59	4182	89.5	0.006	0	13

4/28/16	19:33:24	-16.043	167.3786	7	24	8429	85.8	0.001	0	5
5/28/16	09:47:00	-56.241	-26.9353	7.2	78	10053	89.5	0.000	1	0
7/29/16	21:18:25	18.5429	145.5073	7.7	196	10758	87.8	0.004	1	0
8/12/16	01:26:36	-22.477	173.1167	7.2	16.37	7904	81.9	0.001	0	0
8/19/16	07:32:23	-55.285	-31.8766	7.4	10	9740	93.6	0.000	2	2
8/29/16	04:29:58	-0.0456	-17.8255	7.1	10	11095	90.0	0.001	0	0
9/1/16	16:37:57	-37.359	179.1461	7	19	7689	73.1	0.001	0	4
11/13/16	11:02:56	-42.737	173.054	7.8	15.11	8351	75.8	0.006	0	0
12/8/16	17:38:46	-10.681	161.3273	7.8	40	9054	88.4	0.018	2	1
12/17/16	10:51:11	-4.5049	153.5216	7.9	94.54	9907	89.9	0.003	0	5
12/25/16	14:22:27	-43.406	-73.9413	7.6	38	6469	125.8	0.003	1	0

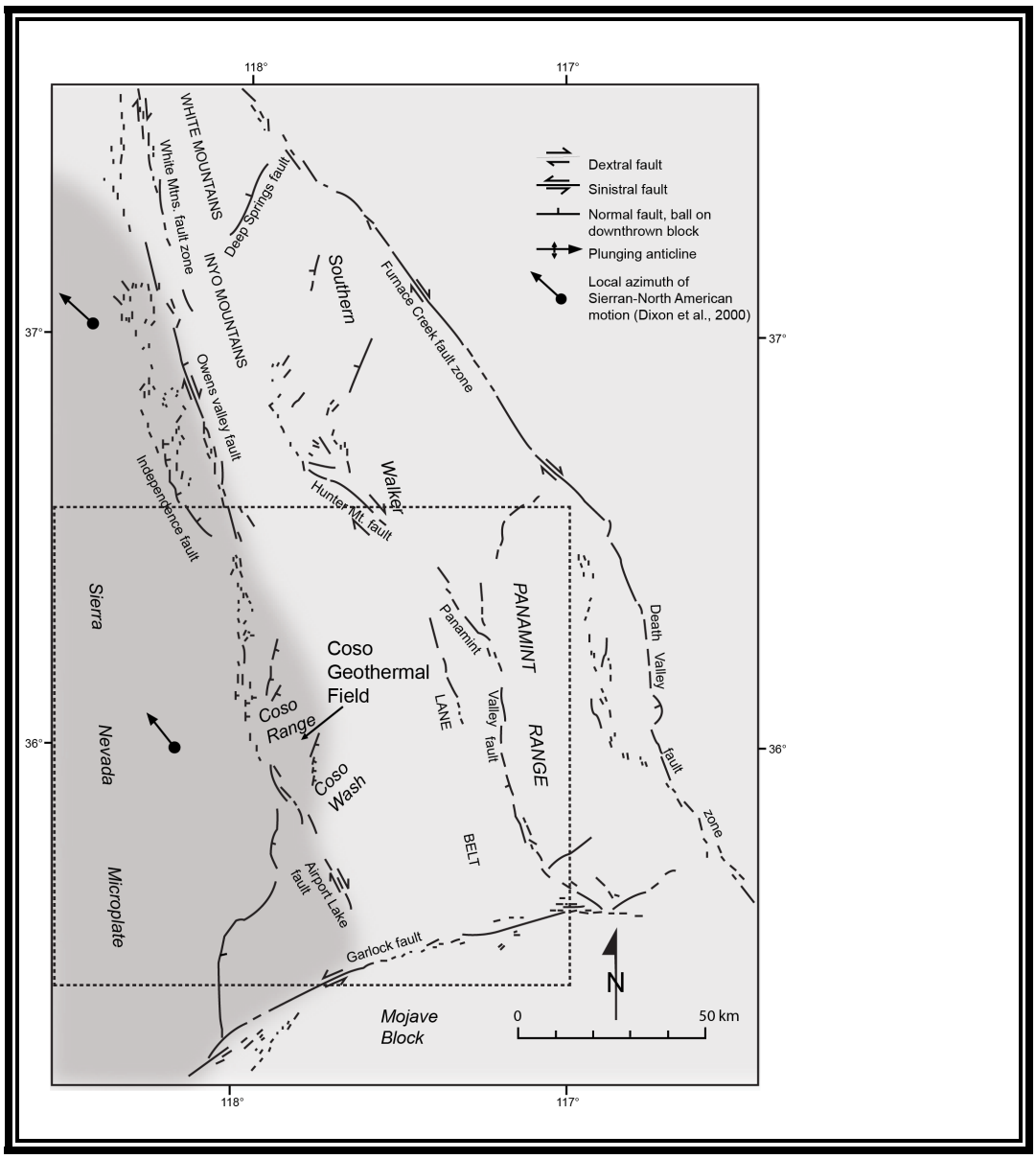

Figure 1.2: Regional location map of the Coso Range and the southern Walker Lane belt; dashed box indicates our study area (35.5°N to 36.5°N, 118.5°W to 117°W). Dark shading indicates the extent of the rigid Sierra Nevada microplate. Note that there is a right-releasing jog along the eastern margin of the Sierran microplate at the latitude of the Coso Range. Figure redrafted and modified from Unruh et al. (2008).

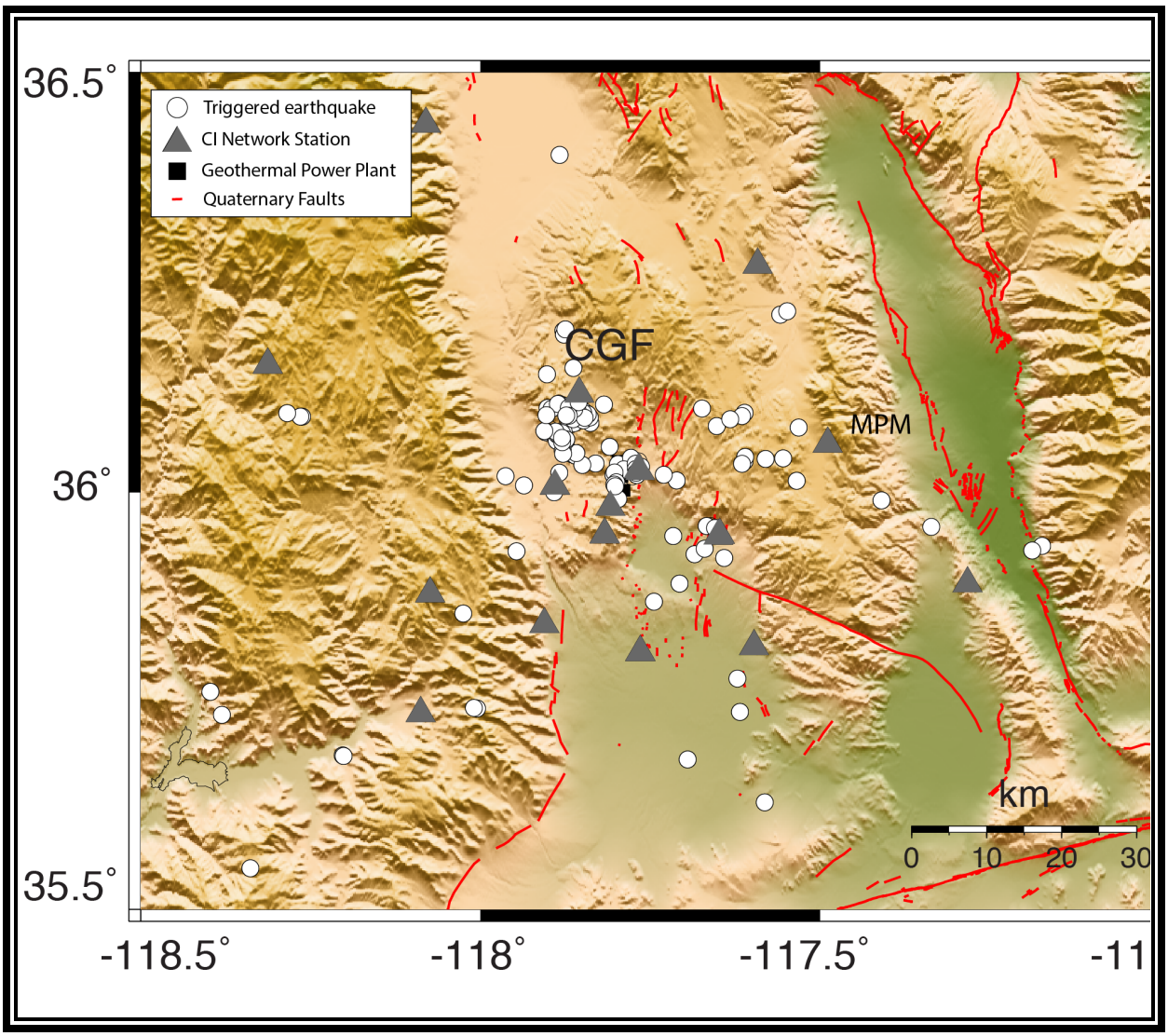

Figure 2.2: Map of locally triggered seismicity (130 events) in our study area cataloged and located by the Southern California Earthquake Center. Event magnitudes span (ML) 0.02-3.45 and depths 0-12 km. Red lines depict quaternary faults (U.S. Geological Survey 2006, Quaternary fault and fold database for the United States, accessed 02/2018).

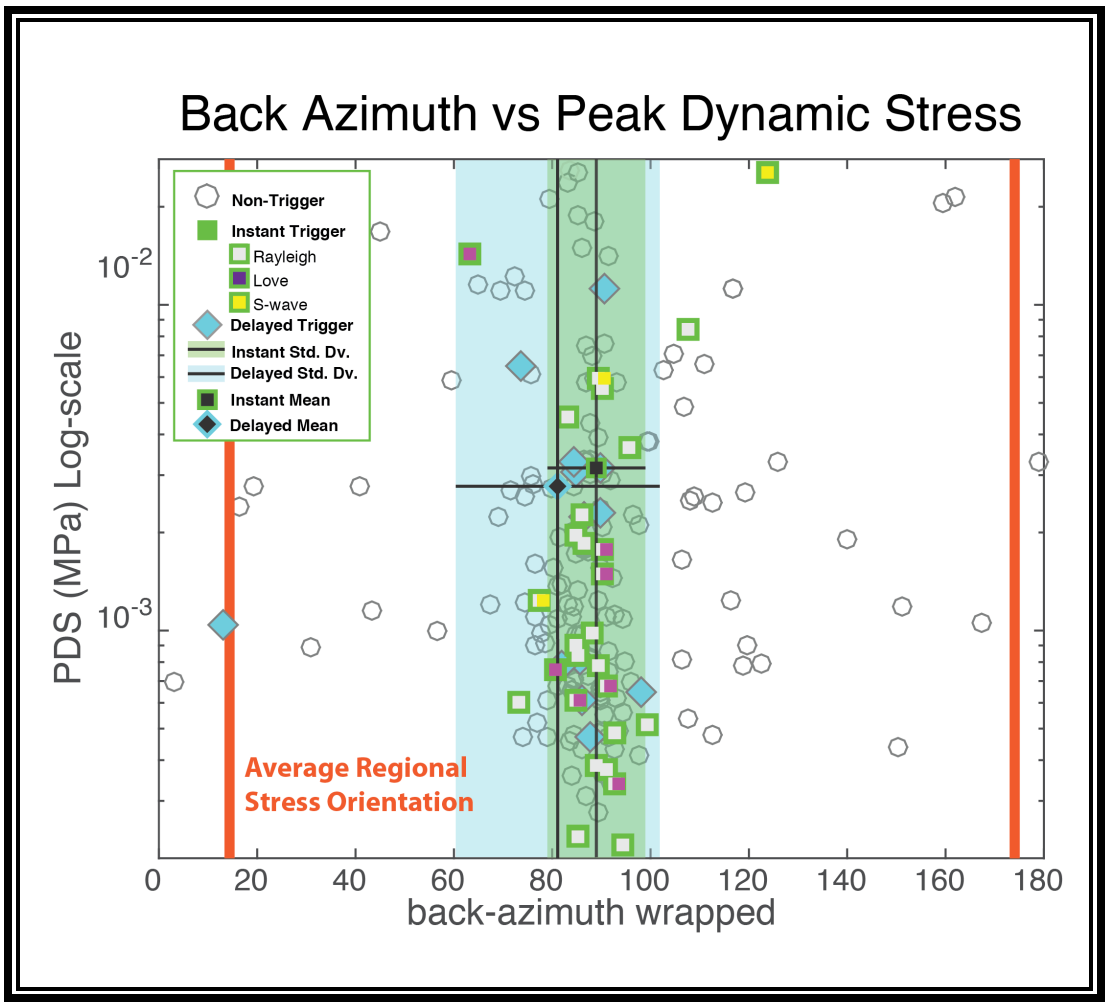

Figure 3.2: Analysis of 211 $M \geq 7$ Mainshocks (2004-2016) back-azimuth orientations versus measured PDS. The back-azimuth of each event is wrapped so that North (0°) - South (180°) and East (90°) -West (270°) are equivalent. Symbols represent non-triggering (open grey circles), instantaneous triggering (green squares) and delayed triggering (cyan diamonds). The instantaneously triggered events are further subdivided into triggering wave types: S-wave (yellow fill color), Love wave (purple fill color), and Rayleigh wave (white fill color). The background green and blue transparent swatches represent the standard deviation of instantaneous and delayed triggering azimuths, respectively. Delayed triggered events occur over a wider range of back-azimuths. Two prominent stress directions exist in our study area; the average of each dominant stress direction is calculated using data from (Heidbach *et al*., 2008) and indicated by the two orange lines. The narrow band of back-azimuths of the triggering mainshocks indicates the orientation of the incoming dynamic stresses plays a key role in the instantaneous triggering of events in the CGF. Instantaneously triggered events are constrained to a specific azimuthal range related to the orientation of the stress field in the CGF. Average mainshock PDS values from recordings at 5 stations, for both non-triggering mainshocks and triggering mainshocks range between values of (10^{-4}–10^{-1} MPa).

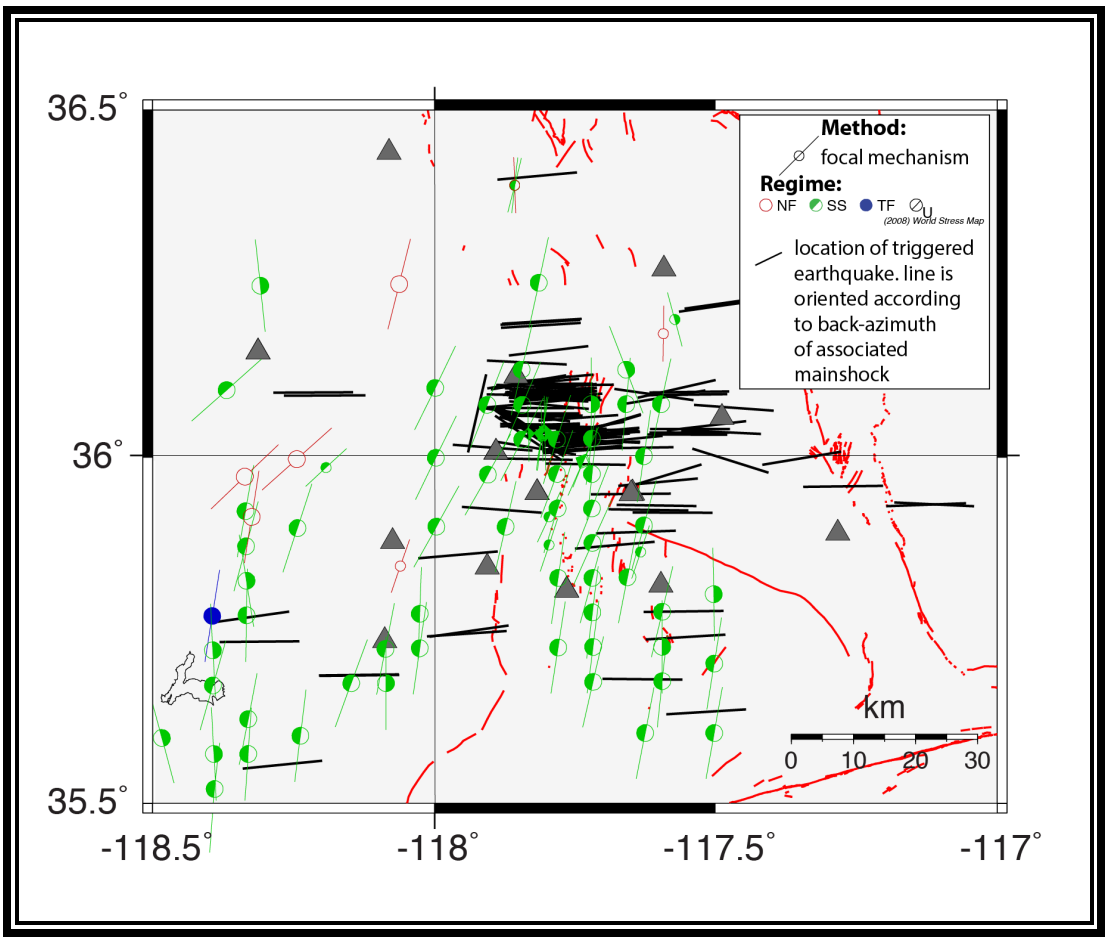

Figure 4.2: Map of regional stress within our study area (35.5°N–36.5°N, 118.5°W–117°W). Stress orientations from the world stress map data (blue and green). The location of locally triggered earthquakes are depicted as black lines, where the line orientation indicates the back-azimuth direction of the associated triggering mainshock. Stress data retrieved from The World Stress Map database (last accessed 11/2017) (Heidbach *et al*., 2008). Note that several events align favorably (approximately perpendicular) with the local stress field and/or orientation of faults in the CGF triggered region.

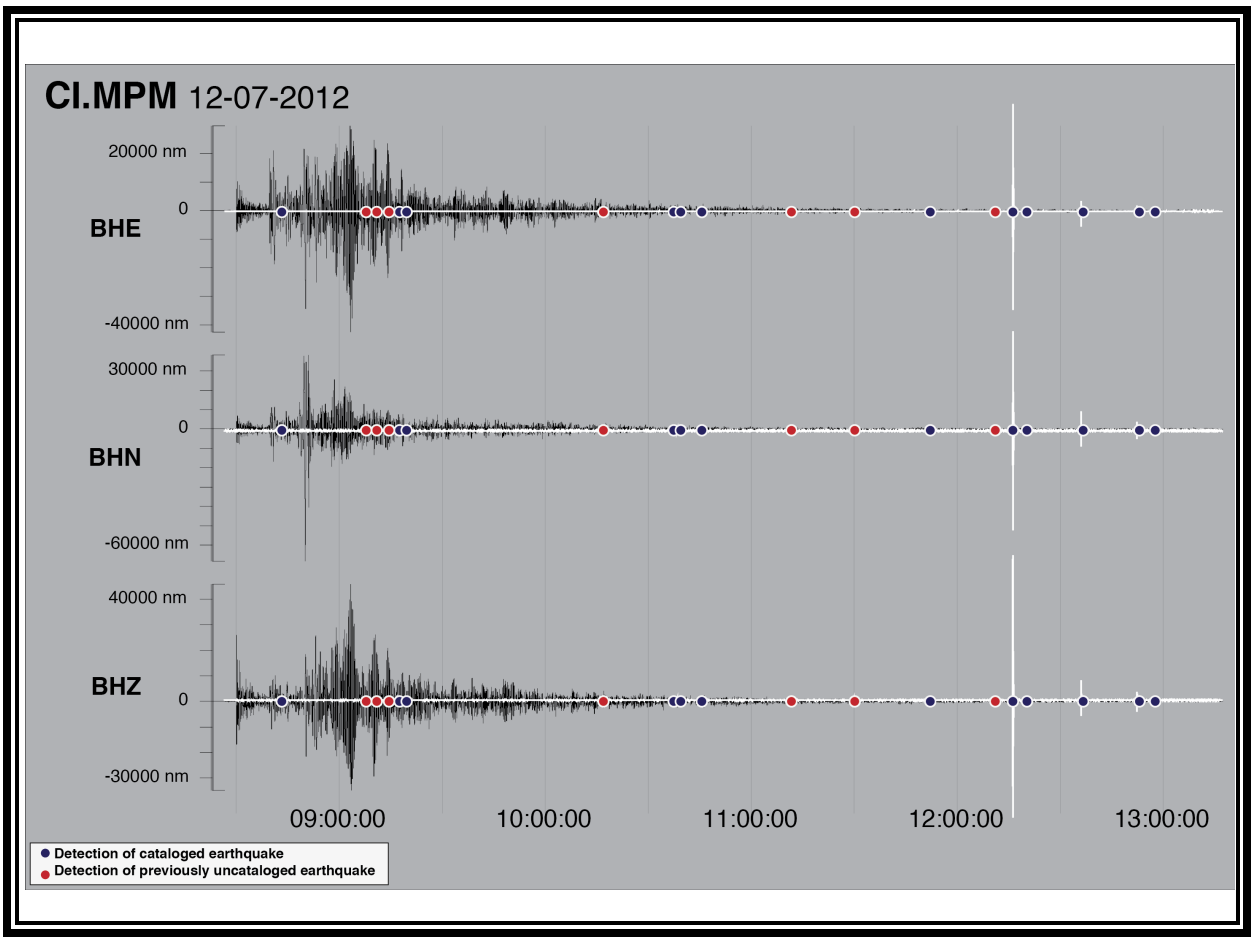

Figure S1.2: Three-component seismic waveforms (original (black) and 5Hz high-pass (white)) from station CI-network MPM of the 12/07/2012 08:18:23.130-UTC Mw=7.3 earthquake off the east coast of Honshu, Japan. We augment the previously cataloged 12 events (blue circles) with an additional 7 events (red circles) detected by our method. In this example, there is both instantaneous triggering (within the wavetrain, times < 11:00:00) and delayed triggering (events occurring after 11:00:00). Seismic activity in the study area increased 50% following the arrival of the mainshock surfaces wave in the region.

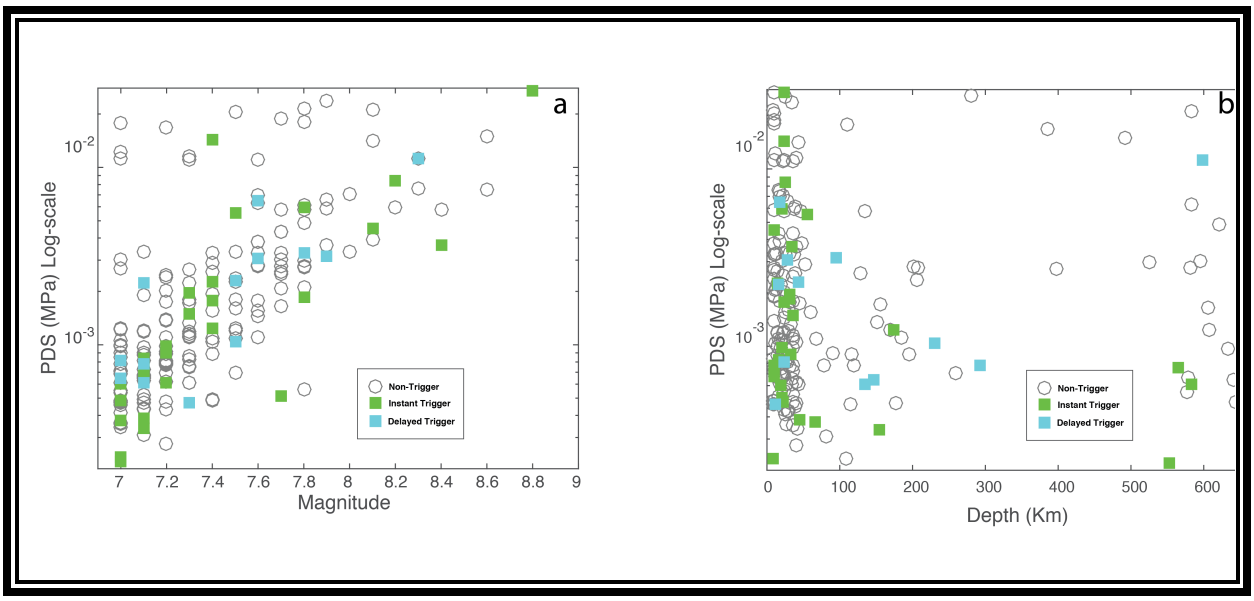

Figure S2.2: Analysis of 211 M ≥ 7 mainshocks (2004-2016). A) Earthquake magnitude versus measured peak dynamic stress (PDS) for each of the 211 events in our study, where the mainshocks are subdivided by triggering type. B) Mainshock depth versus measured peak dynamic stress (PDS).

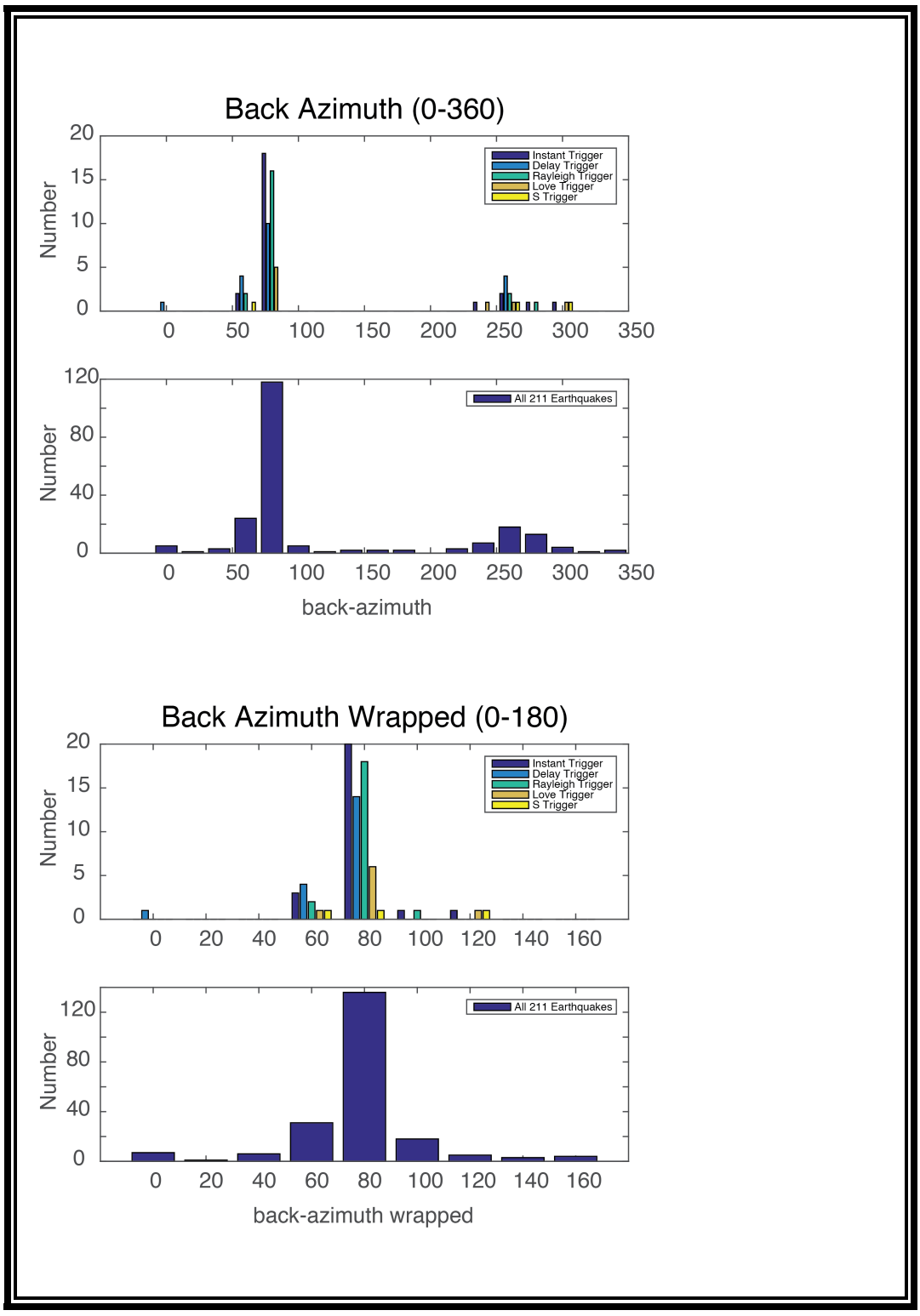

Figure S3.2: Distribution of Back-Azimuth angles. X-axis=angles Yaxis=count. Histogram binned for every 20 degrees.

References

Aiken, C., & Peng, Z. (2014). Dynamic triggering of microearthquakes in three geothermal/volcanic regions of California. Journal of Geophysical Research: Solid Earth, 119(9), 6992–7009. https://doi.org/10.1002/2014JB011218

Bodin, P., & Gomberg, J. (1994). Triggered seismicity and deformation between the Landers, California, and Little Skull Mountain, Nevada, earthquakes. Bulletin of the Seismological Society of America, 84(3), 835–843.

Brodsky, E. E. (2006). Long-range triggered earthquakes that continue after the wave train passes. Geophysical Research Letters, 33(15), L15313. https://doi.org/10.1029/2006GL026605

Brodsky, E. E., Roeloffs, E., Woodcock, D., Gall, I., & Manga, M. (2003). A mechanism for sustained groundwater pressure changes induced by distant earthquakes. Journal of Geophysical Research: Solid Earth, 108(B8). https://doi.org/10.1029/2002JB002321

Brodsky, E. E., & van der Elst, N. J. (2014). The Uses of Dynamic Earthquake Triggering. Annual Review of Earth and Planetary Sciences, 42(1), 317–339. https://doi.org/10.1146/annurev-earth-060313-054648

Brodsky, E., & Prejean, S. G. (2005). New constraints on mechanisms of remotely triggered seismicity at Long Valley Caldera. Journal of Geophysical Research, 110(B4). Retrieved from http://escholarship.org/uc/item/0nq4k55c

Chao, K., Peng, Z., Gonzalez-Huizar, H., Aiken, C., Enescu, B., Kao, H., Matsuzawa, T. (2013). A Global Search for Triggered Tremor Following the 2011 Mw 9.0 Tohoku EarthquakeA Global Search for Triggered Tremor Following the 2011 Mw 9.0 Tohoku Earthquake. Bulletin of the Seismological Society of America, 103(2B), 1551–1571. https://doi.org/10.1785/0120120171

Chao, K., Peng, Z., Wu, C., Tang, C.-C., & Lin, C.-H. (2012). Remote triggering of non-volcanic tremor around Taiwan. Geophysical Journal International, 188(1), 301–324. https://doi.org/10.1111/j.1365-246X.2011.05261.x

Davatzes, N., & Hickman, S. (2006). Stress and faulting in the Coso Geothermal Field: Update and recent results from the East Flank and Coso Wash (Proceedings 31st Workshop on Geothermal Reservoir Engineering No. SGP-TR-187) (pp. 13–19). Stanford, CA: Stanford Univ. Retrieved from https://pangea.stanford.edu/ERE/pdf/IGAstandard/SGW/2006/davatzes.pdf

Elst, N. J. van der, Savage, H. M., Keranen, K. M., & Abers, G. A. (2013). Enhanced Remote Earthquake Triggering at Fluid-Injection Sites in the Midwestern United States. Science, 341(6142), 164–167. https://doi.org/10.1126/science.1238948

Gomberg, J., Bodin, P., Larson, K., & Dragert, H. (2004). Earthquake nucleation by transient deformations caused by the M = 7.9 Denali, Alaska, earthquake. Nature, 427(6975), 621–624. https://doi.org/10.1038/nature02335

Gomberg, J., Reasenberg, P. A., Bodin, P., & Harris, R. A. (2001). Earthquake triggering by seismic waves following the Landers and Hector Mine earthquakes. Nature, 411(6836), 462–466. https://doi.org/10.1038/35078053

Gonzalez-Huizar, H., Velasco, A. A., Peng, Z., & Castro, R. R. (2012). Remote triggered seismicity caused by the 2011, M9.0 Tohoku-Oki, Japan earthquake. Geophysical Research Letters, 39(10). https://doi.org/10.1029/2012GL051015

Guilhem, A., Peng, Z., & Nadeau, R. M. (2010). High-frequency identification of non-volcanic tremor triggered by regional earthquakes. Geophysical Research Letters, 37(16). https://doi.org/10.1029/2010GL044660

Heidbach, O., Tingay, M., Barth, A., Reinecker, J., Kurfeß, D., & Müller, B. (2010). Global crustal stress pattern based on the World Stress Map database release 2008. Tectonophysics, 482(1–4), 3–15. https://doi.org/10.1016/j.tecto.2009.07.023

Hill, D. P., & Prejean, S. G. (2015). 4.11 - Dynamic Triggering. In G. Schubert (Ed.), Treatise on Geophysics (Second Edition) (pp. 273–304). Oxford: Elsevier. https://doi.org/10.1016/B978-0-444-53802-4.00078-6

Hill, D. P., Reasenberg, P. A., Michael, A., Arabaz, W. J., Beroza, G., Brumbaugh, D., … Zollweg, J. (1993). Seismicity Remotely Triggered by the Magnitude 7.3 Landers, California, Earthquake. Science, 260(5114), 1617–1623. https://doi.org/10.1126/science.260.5114.1617

Hill, David P. (2008). Dynamic Stresses, Coulomb Failure, and Remote Triggering. Bulletin of the Seismological Society of America, 98(1), 66–92. https://doi.org/10.1785/0120070049

Hutton, K., Woessner, J., & Hauksson, E. (2010). Earthquake Monitoring in Southern California for Seventy-Seven Years (1932–2008)Earthquake Monitoring in Southern California for Seventy-Seven Years (1932–2008). Bulletin of the Seismological Society of America, 100(2), 423–446. https://doi.org/10.1785/0120090130

Jagla, E. A. (2011). Delayed dynamic triggering of earthquakes: Evidence from a statistical model of seismicity. EPL (Europhysics Letters), 93(1), 19001. https://doi.org/10.1209/0295-5075/93/19001

Kane, D. L., Kilb, D., Berg, A. S., & Martynov, V. G. (2007). Quantifying the remote triggering capabilities of large earthquakes using data from the ANZA Seismic Network catalog (southern California). Journal of Geophysical Research: Solid Earth, 112(B11). https://doi.org/10.1029/2006JB004714

Kilb, D., Gomberg, J., & Bodin, P. (2000). Triggering of earthquake aftershocks by dynamic stresses. Nature, 408(6812), 570–574. https://doi.org/10.1038/35046046

Kilb, D., Gomberg, J., & Bodin, P. (2002). Aftershock triggering by complete Coulomb stress changes. Journal of Geophysical Research B: Solid Earth, 107(4), 2–1.

Kilb, Deborah, Gomberg, J., & Bodin, P. (2000). Triggering of earthquake aftershocks by dynamic stresses. Nature, 408(6812), 570–574. https://doi.org/10.1038/35046046

King, G. C. P., Stein, R. S., & Lin, J. (1994). Static stress changes and the triggering of earthquakes. Bulletin of the Seismological Society of America, 84(3), 935–953.

Linville, L., Pankow, K., Kilb, D., & Velasco, A. (2014). Exploring remote earthquake triggering potential across EarthScopes' Transportable Array through frequency domain array visualization. Journal of Geophysical Research: Solid Earth, 119(12), 8950–8963. https://doi.org/10.1002/2014JB011529

Morton, E. A., & Bilek, S. L. (2014). Limited Dynamic Earthquake Triggering in the Socorro Magma Body Region, Rio Grande Rift, New Mexico. Bulletin of the Seismological Society of America. https://doi.org/10.1785/0120140021

Pankow, K. L., Arabasz, W. J., Pechmann, J. C., & Nava, S. J. (2004). Triggered Seismicity in Utah from the 3 November 2002 Denali Fault Earthquake. Bulletin of the Seismological Society of America, 94(6B), S332–S347. https://doi.org/10.1785/0120040609

Parsons, T., Stein, R. S., Simpson, R. W., & Reasenberg, P. A. (1999). Stress sensitivity of fault seismicity: A comparison between limited-offset oblique and major strike-slip faults. Journal of Geophysical Research B: Solid Earth, 104(B9), 20.

Parsons, Tom. (2005). A hypothesis for delayed dynamic earthquake triggering. Geophysical Research Letters, 32(4). https://doi.org/10.1029/2004GL021811

Parsons, Tom, Kaven, J. O., Velasco, A. A., & Gonzalez-Huizar, H. (2012). Unraveling the apparent magnitude threshold of remote earthquake triggering using full wavefield surface wave simulation. Geochemistry, Geophysics, Geosystems, 13(6). https://doi.org/10.1029/2012GC004164

Parsons, Tom, Malagnini, L., & Akinci, A. (2017). Nucleation speed limit on remote fluid-induced earthquakes. Science Advances, 3(8), e1700660. https://doi.org/10.1126/sciadv.1700660

Peng, Z., & Chao, K. (2008). Non-volcanic tremor beneath the Central Range in Taiwan triggered by the 2001 M_w 7.8 Kunlun earthquake. Geophysical Journal International, 175(2), 825–829. https://doi.org/10.1111/j.1365-246X.2008.03886.x

Peng, Z., Hill, D. P., Shelly, D. R., & Aiken, C. (2010). Remotely triggered microearthquakes and tremor in central California following the 2010 Mw 8.8 Chile earthquake. Geophysical Research Letters, 37(24). https://doi.org/10.1029/2010GL045462

Peng, Z., Wu, C., & Aiken, C. (2011). Delayed triggering of microearthquakes by multiple surface waves circling the Earth. Geophysical Research Letters, 38(4), L04306. https://doi.org/10.1029/2010GL046373

Prejean, S. G., Hill, D. P., Brodsky, E. E., Hough, S. E., Johnston, M. J. S., Malone, S. D., … Richards-Dinger, K. B. (2004). Remotely Triggered Seismicity on the United States West Coast following the Mw 7.9 Denali Fault Earthquake. Bulletin of the Seismological Society of America, 94(6B), S348–S359. https://doi.org/10.1785/0120040610

Prejean, Stephanie G., & Hill, D. P. (2018). The influence of tectonic environment on dynamic earthquake triggering: A review and case study on Alaskan volcanoes. Tectonophysics, 745, 293–304. https://doi.org/10.1016/j.tecto.2018.08.007

Schoenball, M., Davatzes, N. C., & Glen, J. M. G. (2015). Differentiating induced and natural seismicity using space-time-magnitude statistics applied to the Coso Geothermal field. Geophysical Research Letters, 42(15), 6221–6228. https://doi.org/10.1002/2015GL064772

Shearer, P. M., & Stark, P. B. (2012). Global risk of big earthquakes has not recently increased. Proceedings of the National Academy of Sciences, 109(3), 717–721. https://doi.org/10.1073/pnas.1118525109

Stein, R. S., King, G. C., & Lin, J. (1994). Stress triggering of the 1994 m = 6.7 northridge, california, earthquake by its predecessors. Science (New York, N.Y.), 265(5177), 1432–1435. https://doi.org/10.1126/science.265.5177.1432

Stein, Ross S., King, G. C. P., & Lin, J. (1992). Change in Failure Stress on the Southern San Andreas Fault System Caused by the 1992 Magnitude = 7.4 Landers Earthquake. Science, 258(5086), 1328–1332.

Syracuse, E. M., Thurber, C. H., Wolfe, C. J., Okubo, P. G., Foster, J. H., & Brooks, B. A. (2010). High-resolution locations of triggered earthquakes and tomographic imaging of Kilauea Volcano's south flank. Journal of Geophysical Research: Solid Earth, 115(B10), B10310. https://doi.org/10.1029/2010JB007554

Tape, C., West, M., Silwal, V., & Ruppert, N. (2013). Earthquake nucleation and triggering on an optimally oriented fault. Earth and Planetary Science Letters, 363, 231–241. https://doi.org/10.1016/j.epsl.2012.11.060

Taylor, J. R. (1982). An Introduction to Error Analysis: The Study of Uncertainties in Physical Measurements (2nd ed.). Sausalito, Calif: Univ. Science Books.

Toda, S., Stein, R. S., Reasenberg, P. A., Dieterich, J. H., & Yoshida, A. (1998). Stress transferred by the 1995 Mw = 6.9 Kobe, Japan, shock: Effect on aftershocks and future earthquake probabilities. Journal of Geophysical Research B: Solid Earth, 103(10), 23.

van der Elst, N. J., Savage, H. M., Keranen, K. M., & Abers, G. A. (2013). Enhanced Remote Earthquake Triggering at Fluid-Injection Sites in the Midwestern United States. Science, 341(6142), 164–167. https://doi.org/10.1126/science.1238948

Velasco, A. A., Alfaro-Diaz, R., Kilb, D., & Pankow, K. L. (2016). A Time-Domain Detection Approach to Identify Small Earthquakes within the Continental United States Recorded by the USArray and Regional NetworksTime-Domain Detection Approach to Identify Small Earthquakes within the Continental U.S. Bulletin of the Seismological Society of America, 106(2), 512–525. https://doi.org/10.1785/0120150156

Velasco, A. A., Ammon, C. J., Farrell, J., & Pankow, K. (2004). Rupture Directivity of the 3 November 2002 Denali Fault Earthquake Determined from Surface Waves. Bulletin of the Seismological Society of America, 94(6B), S293–S299. https://doi.org/10.1785/0120040624

Velasco, A. A., Hernandez, S., Parsons, T., & Pankow, K. (2008). Global ubiquity of dynamic earthquake triggering. Nature Geoscience, 1(6), 375–379. https://doi.org/10.1038/ngeo204

West, M., Sánchez, J. J., & McNutt, S. R. (2005). Periodically Triggered Seismicity at Mount Wrangell, Alaska, After the Sumatra Earthquake. Science, 308(5725), 1144–1146. https://doi.org/10.1126/science.1112462

Zhang, Q., Lin, G., Zhan, Z., Chen, X., Qin, Y., & Wdowinski, S. (2017). Absence of remote earthquake triggering within the Coso and Salton Sea geothermal production fields. Geophysical Research Letters, 44(2), 726–733. https://doi.org/10.1002/2016GL071964

Chapter 3: Unraveling earthquake stresses: Insights from dynamically triggered and induced earthquakes

Induced seismicity, earthquakes caused by anthropogenic activity, has more than doubled in the last several years resulting from practices related to oil and gas production. Furthermore, large earthquakes have been shown to promote the triggering of other events within two fault lengths (static triggering), due to static stresses caused by physical movement along the fault, and also remotely from the passage of seismic waves (dynamic triggering). Thus, in order to understand the mechanisms for earthquake failure, we investigate regions where natural, induced, and dynamically triggered events occur, and specifically target Oklahoma. Utilizing 9 years of data (2008-2016) from EarthScope's USArray Transportable Array, Oklahoma, and GS local networks, we search for dynamically triggered seismicity in Oklahoma (OK). We first apply a short term to long term average ratio detector to high-pass (5 Hz) filtered waveforms spanning ±5 hours encompassing 144 $M \geq 7$ global earthquakes. We visually inspect these waveforms to identify uncatalogued local earthquakes. We use our augmented local earthquake catalog to investigate remote earthquake triggering in OK. Flagging mainshocks with a statistically significant increase in seismicity following the P-wave arrival, we find that of the 144 remote mainshocks, 24 (17%) statistically triggered seismicity in OK. An additional 31 mainshocks had local earthquakes coincident with the surface waves, but no statistically significant rate increase was found. Of the 55 triggering mainshocks, 51 and 4 exhibit instantaneous and delayed triggering, respectively. We find transient stresses can contribute to natural and induced stress states advancing the earthquake cycle and providing insight to the constantly changing stress state of induce systems. Utilizing the distribution of triggered earthquake populations in the OK region we identify regions particularly susceptible to earthquake hazards associated with sustained fluid injection.

1 INTRODUCTION

A growing body of evidence suggests that there is a strong link between earthquakes. Large earthquakes have been shown to promote the triggering of other events within two fault lengths, due to static stresses caused by physical movement along the fault (e.g., Stein *et al*., 1992; Stein *et al*., 1994; King *et al*., 1994), which is called static triggering. Seismic waves originating from large magnitude earthquakes ($M \geq 7$) also create dynamic stresses from propagating waves that can trigger small earthquakes and tremor at remote distances, and is referred to as dynamic or remote triggering (e.g., Hill *et al*., 1993; Brodsky *et al*., 2000; Kilb *et al*., 2000; Gomberg *et al*., 2001, 2004; West *et al*., 2005, Parsons *et al*., 2012; Velasco *et al*., 2008; Guilhem *et al*., 2010; Chao *et al*., 2012). Recent work has suggested that delayed dynamic triggering can even promote large earthquakes (Gomberg *et al*., 1997; Pollitz *et al*., 2012), yet the physical mechanism has many possible explanations with little consensus (e.g., Parsons *et al*., 2012; Brodsky and Prejean, 2005).

Beyond the link between earthquakes, seismic activity caused by human activity (induced seismicity) has been of growing interest; the number of earthquakes has more than doubled in the last several years (Ellsworth, 2013; Ellsworth *et al*., 2015; McNamara *et al*., 2015). These generally smaller, induced earthquakes impact local populations, which prompted the U.S.G.S to develop an induced seismicity hazard map beyond the traditional natural seismicity hazard map (Petersen *et al*., 2016). Much of the increase in induced seismicity results from practices to extract and/or stimulate oil and gas production, such as waste-water injection (Ellsworth *et al*., 2015). Although the mechanism for these injection-induced earthquakes results from weakening a preexisting fault through elevated fluid pressure, only a small fraction of the events appear to be dangerous. Thus, the challenge remains to understand the exact mechanisms of failure, such

that stress changes can remain below a threshold as to reduce activity and perhaps prevent larger earthquakes from occurring.

We examine the OK region (Figure 1) as it presents an ideal study site to observe the interaction of dynamic stresses produced by M ≥ 7 earthquakes and the local induced stress fields. We select data 5 hours before and 5 hours after the origin times for 144 $M \geq 7$ earthquakes at stations from the EarthScope Transportable Array (TA) and the Oklahoma local network (OK) over a nine-year period (2008-2016). We use an optimized detection algorithm to detect high frequency signals [*Velasco et al.,* 2016], and visually inspect these signals to identify earthquakes. All newly identified earthquakes are added to existing catalogs. These catalogs are then used to identify statistically significant changes in detection rates assuming a Poissonian distribution [*Velasco et al.,* 2008; *Linville et al*., 2014; *Alfaro-Diaz et al.,* 2019].

Of the 144 mainshocks, 24 have statistically significant rate increases coincident with the passing surface waves consistent with dynamic triggering and an additional 31 have local events occurring during the passage of the surface wave, but show no significant increase in the rate of earthquakes. The events in the later case may also be triggered, but do not fit past observations where dynamic triggering generates a seismic rate increase.

2 BACKGROUND

Recent increases in seismicity in the midwestern United States have been related to deep wastewater injection sites (e.g., van der Elts et al., 2013). Fluid injection sites are susceptible to triggering by small changes in stress induced by the passage of seismic waves of distant large earthquakes (e.g., van der Elts et al., 2013). Most triggered injection sites have a delay between the beginning of fluid injection and the start of seismicity, suggesting fluid injection can push a fault system into a critical state (van der Elts et al., 2013). Three sites: Prague, Oklahoma;

Snyder, Texas; and Trinidad, Colorado hosted triggered events after large magnitude distant earthquakes: the Maule, Chile February, 27 2010 M=8.8; Tohoku-oki March, 11 2011 M=9.1 (Figure 2); and Sumatra April, 12 2012 M=8.6 (van der Elts et al., 2013). Van der Elst et al. (2013) hypothesized that some regions of induced earthquake can host larger more hazardous triggered events that would otherwise not be possible had the region not experienced sustained fluid injection.

Following this study, relatively little work explored the impact of dynamic triggering in regions related to active oil and gas exploitation and induced seismicity. Investigating dynamically triggered seismicity in natural and induced settings; we address fundamental questions about the state of stress of faults. In particular, we decipher the stress type, orientation, and magnitude needed to trigger earthquakes in OK. Despite the small seismic hazard of dynamic triggering, regions that have been subjected to sustained fluid injection and induced seismicity may host larger, hazardous triggered earthquakes. Figure 1 indicates the current regional stress state defined by Heidbach *et al*. (2008). We identify regions that may be susceptible to these risks.

3 DATA AND METHOD

We investigate remote triggering in Oklahoma using a tuned Short Term Average over Long Term Average (STA/LTA) detection algorithm [*Velasco et al*., 2016] and waveform data from the EarthScope Transportable Array (TA) and the Oklahoma local networks (OK), and catalog earthquake data from the Oklahoma Geological Survey (OGS) (last accessed 01. 2019, www.ou.edu/ogs). Using the Standing Order of Data (SOD) tool from the Incorporated Research Institutes for Seismology (IRIS) Data Management Center (DMC), we obtained seismograms from ~70 stations within OK and the surrounding region. For each of our 144 M≥7 mainshocks,

we collect 10 hours of data (5 hours before and after the mainshock) bracketing the origin time of 144 $M \geq 7$ earthquakes over a nine-year period (2008-2016). We create individual waveform databases for each of our 144 mainshocks using the Boulder Real Times Technologies Antelope software. We apply a 4s/40s STA/LTA detection algorithm to three-component high-passed (5 Hz) filtered data, and flag detections that occur on at least 2 of the 3 components [method Ev1 from *Velasco et. al*, 2016]. This approach, requiring a detection on not just one, but two components, significantly reduces the detection of spurious non-seismic sources [*Velasco et. al*, 2016].

Figure 3 shows an example in OK, where we identify an uncataloged event that was detected on a USArray station. From this observation, if the Love wave is responsible for triggering, then the role of fluids may not be a strong factor in this particular event, since Love waves are shear waves. Thus, the role of different dynamic stresses will help us decipher if fluids are solely responsible for the stress release of these induced, ancient faults.

4 Assessing Remote Triggering in Oklahoma

4.1 Triggering Results

We calculate the probability of increased seismicity rates by comparing the number of local earthquakes immediately before and after the teleseismic mainshock. In order to identify statistically significant increases in numbers of local earthquakes, we process a time window of ±5 hours for each mainshock ($M \geq 7$) earthquake and assume that earthquakes occur independently (randomly) at a constant rate, following a Poissonian distribution [*Shearer and Stark*, 2012]. We consider a mainshock event to successfully trigger remote aftershocks in OK if the number of events in the 5-hour window following the arrival of the mainshock *P*-wave significantly exceeds the number of events within the prior 5-hours. We categorize the seismic

triggering as: 1) instantaneous if the increase in number of events begins in the wavetrain of the mainshock and 2) delayed if there is an increase in number of events after the wavetrain but within 5 hours of the initial mainshock.

Utilizing the methods of Alfaro-Diaz et. al (2019) we determine statistical significance, and follow what is expected for a Poisson distribution and compare the number of expected events in the 5-hour window before the P-wave (Npre) arrival to the number of events in the post 5-hour window (Npost). We assume that the average of Npre for all 144 mainshocks is a reasonable approximation to the background rate for a 5-hour window. To determine significant changes in rates we calculate the Poisson probability of getting Npost events (ν) given the expected number of events (μ, the average of Npre).

$$P_{\mu}(\nu) = e^{-\mu}\frac{\mu^{\nu}}{\nu!}$$

For the 144 mainshocks in our dataset, the average number of Npre (μ) equals 4 (the standard deviation on the mean is 6). Using this as μ in the probability equation, Npost values (ν) > 8 have < 5% probability of occurring and ν > 10, < 1% probability of occurring.

Based on these probabilities, we determine mainshocks that may have triggered remote aftershock(s) in OK if the probability of Npost events given an average rate of 4 is < 5%. Using this criteria, 31 mainshocks are identified for further analysis. For these 31 events, we next look at the number of Npre events to determine if there was already an elevated rate of earthquakes at the time of the mainshock and then we further compare the rate change between Npre and Npost (assuming Npre equals μ). For the 31 mainshocks, 4 have Npre values > 10 indicating an elevated rate of events at the time of the mainshock. Of these, we conclude that 2 are probably associated with dynamic triggering because the probability of the rate change between Npre and Npost < 2%. The other two events do not show a significant increase in the Npre to Npost events.

There are also 13 mainshocks where Npre is within 1 standard deviation of the Npre mean, for these we also test Npre as μ and calculate the probability of the change in rate between Npre and Npost. Of these 13, we conclude that 8 are probably associated with dynamic triggering because the probability of the rate change between Npre and Npost < 4%. The remaining 5 cases exceed a 5% chance of occurring and we exclude them from the triggering catalog. Based on a statistically significant change in earthquake rates at the time of the mainshock 24 of these events dynamically triggered aftershocks in OK.

In addition to looking at statistically significant changes in earthquake rates, we also identify mainshocks that have local earthquakes embedded within the surface waves. While it is difficult to rule out that these events might have occurred by chance, the coincidence with the timing of the surface waves warrants additional analysis. We identify 31 mainshocks that had local earthquakes occurring during the passage of the surface wave (with no statistically significant seismicity rate increase) and report them as special cases (Table 1). Counting these 31 mainshocks as also triggering brings us to 55 (38%) remote triggering mainshocks. These 55 events have moment magnitudes ranging from 7.0 to 8.8 and depths 8 to 607 km (49 mainshocks 0-200 km, 3 mainshocks 200-439 km, 3 mainshocks 440-600 km).

4.2 Identifying Instantaneous and Delayed Triggering in Oklahoma

Of our 55 triggering mainshocks, 51 instantaneously triggered local seismicity, of which the majority of the triggering occurred within the wavetrain of the passing surface waves (Figure S1). The remaining 4 mainshocks are classified as delayed triggering events, where the triggered seismicity occurred within 5-hours of the P-wave, but after the passage of the mainshock energy (Figure S1). We identify 477 local events ranging in magnitude (M_L) 0.0-3.9 triggered within 5-hours following 55 mainshock earthquakes ($M_W \geq 7.0$). Of the 477 local events, we identify 371

events that had not been previously cataloged, the remaining 106 events were included in the OGS catalog. All events reported here have been visually reviewed.

4.3 Factors Contributing to Triggering

We explore a suite of factors that can contribute to triggering in Oklahoma: mainshock focal mechanism, depth, peak dynamic stress, and orientation of the incoming mainshock seismic arrivals. The majority of mainshocks exhibit a thrust mechanism and are concentrated near the western edge of the Pacific Plate, a naturally more seismically active area. We do not attribute mainshock focal mechanism as a preferential trigger mechanism specific to Oklahoma as a variety of mainshock focal mechanisms appear to trigger seismicity. We compute an average the mainshock generated peak dynamic stress (PDS) (dependent on available stations). In order to compute PDS, we estimate peak vector velocities using three-component broadband data and multiply by shear modulus/Love wave group velocity (μ = 33000 MPa, U = 3.5 km/s) (Pankow et al., 2004). We then average the derived PDS obtained for available stations for each mainshock. In this way, we can examine the average PDS values as a function of mainshock magnitude, depth, and back-azimuth for each triggering and non-triggering mainshock (Table 2 and Figure 6). We find the average mainshock PDS values, for both non-triggering mainshocks and triggering mainshocks (Figure 6) generally range between values of (10^{-4}–10^{-1} MPa). The highest PDS value we computed was ~0.13 MPa for non-triggering events and ~0.13 MPa for triggering events. The lowest PDS we computed for a triggering event is ~0.0001 MPa (M 7.1 Origin 4km SE of Sagbayan, Philippines on 2013-10-15 00:12:32 UTC) a small value implying relatively weak triggering. Our data indicates a triggering threshold of <0.001 MPa for the region. In general region seems to require higher stresses (in comparison to regions in California studies *Aiken & Peng* (2014), *Alfaro-Diaz et al*. (2019)) to incite instantaneous triggering. The

orientation of the incoming dynamic stresses appears to play a role in the instantaneous triggering on at the local scale (Figure 5).

We also investigate the relationship between the local stress field and orientation of incoming surface waves (Figure 5). Back-azimuth orientations are calculated from each source location to Oklahoma City (35.4676° N, 97.5164° W) (Table 2) using the DISTAZ tool from the IRIS DMC. Calculated back-azimuth orientations are then wrapped so that orientations indicating N-S or E-W become equivalent and the data ranges from 0°-180°, allowing us to increase our data density. We separate the azimuthal orientation data into delayed and instantaneous triggering categories, and further divide instantaneous triggered events into triggering phases (S, Love, and Rayleigh waves). We calculate the mean and standard deviation of both delayed and instantaneous triggering azimuthal orientation datasets, and compare these data against non-triggering mainshocks, finding that both instantaneous and delayed triggering occur mainly over a wide range of orientations ~104 ±40 degrees and ~107 ±27 degrees respectively (Figure 6). We inspect these trends further in the subsequent section

4.4 Stress Analysis

We examine the back-azimuth angles of our triggering mainshocks and find a wide range of azimuths in which both instantaneous triggering and (29°- 168° back azimuths), delayed triggering (54°- 162° back azimuths) occur. Analyzing stress data taken from Heidbach et. al. (2016) and Alt & Zoback (2017) (Figures 1 & 7)we observe the region stress of Oklahoma predominantly trends (~80). The orientation of the incoming dynamic stresses appears to play a role in the instantaneous triggering in some cases (Figure 7). However, active oil and gas exploitation in the Oklahoma may allow for localized perturbations in stresses not previously accounted for. If these areas exhibit more complex behavior, (instantaneous) dynamically

triggered events may provide a proxy to understanding the local stress field (*Alfaro-Diaz et. al.,* 2019 *in review*). However, this is beyond the scope of this article, further analysis will be needed to quantify stress at the local scale.

5 DISCUSSION

In this study, we investigate 144 mainshocks M≥7 worldwide with depths ranging from 8 to 587 km capable of triggering remote seismicity in Oklahoma. We find 477 locally triggered earthquakes following 55 of the 144 mainshocks. Of the 477 local triggered earthquakes, 104 are considered instantaneously triggered as they occur within the wavetrain of the mainshock (Figure 3). The majority (67%) of instantaneously triggered earthquakes (70) are incited by the passage of Rayleigh waves. Previous documentation of dynamically triggered earthquakes indicates Rayleigh waves (which produce both longitudinal and transverse motion) can trigger events by inducing fluid excitation or by Coulomb failure (*Rubinstein et al*. 2007, 2009; *Hill* 2008; *Miyazawa et al*. 2008; *Peng and Chao*, 2008; *Peng et al*., 2008, 2009, 2010a) Given the active oil and gas exploitation in Oklahoma, many of the events can be assumed related to fluids and anthropogenic influences where humans have weakened the subsurface facture networks in a manner that can actually increase the likelihood of dynamic triggering in a region surrounding the anthropogenic footprint of the production wells (Ellsworth, 2013; Ellsworth *et al*., 2015; McNamara *et al*., 2015). We also identify a local triggering mechanism that favors shear-induced failure, which is fundamentally different than the fluid migration mechanism. Several events were instantaneous triggered by either the S-wave (18 events) or Love-wave (16 events) arrivals. We note the cases of local earthquakes triggered by the onset of Love-wave and Rayleigh-wave arrivals may also be consistent with failure by the Coulomb failure criteria (*Kilb et al*., 2002;

Peng and Chao, 2008; *Hill*, 2008; *Peng et al*. 2008, 2009, 2010a; *Gonzalaz-Huizar and Velasco*, 2010).

Similar to previous studies, Delayed triggered events compromise the majority (78%, 373 events) of all triggered seismic in the Oklahoma region, such that the local earthquakes occur after the passage of the remote mainshock seismic waves [e.g., *Gonzalez-Huizar et al*., 2012; 2008; *Jagla*, 2011; *Morton and Bilek*, 2014; *Peng et al*., 2010a; *van der Elst et al*., 2013]. There have been a number of triggering mechanisms proposed to explain these delays including: the excitation of crustal fluids [e.g., *Hill and Prejean*, 2015 and references therein], a change in frictional contact along a fault [*Parsons*, 2005], arrival of multiple surfaces waves circling the Earth [*Peng et al*., 2011], pore fluid diffusion, and transient pore-pressure changes [*Brodsky et al*., 2003; *Brodsky and Prejean*, 2005; *Bodin and Gomberg*, 1994; *Brodsky*, 2006; *Syracuse et al*., 2010]. In the Oklahoma region, a combination of these mechanisms may incite a delay in the triggered response.

Parsons et al. [2017] found that delay times even appear to correlate with magnitude of triggered earthquakes, as fluid needs to diffuse across a locked fault asperity before failure. Delay times related to this process specifically in seismically active areas such as OK can be short (seconds-minutes-hours) as the distance between pockets of elevated pore-pressure and adjacent faults is short [*Prejean and Hill*, 2018]. Our delayed triggering results are likely most consistent with the excitation of crustal fluids, pore fluid diffusion, transient pore-pressure, and changes in frictional contact. In this case, fluids associated with the CO2 sequestration may migrate after the passage of the mainshock generated transient wavetrain, eventually triggering local seismicity. The normal stress and strength of a fault may be reduced by these processes promoting failure by shear stresses.

We argue that anthropogenic injection and extraction activity has altered the stress state and fluid flow within the production basins of Oklahoma. Fluids associated with wastewater sites in Oklahoma may migrate after the passage of the mainshock generated transient wavetrain and eventually trigger local seismicity. In the case of delayed triggering, the normal stress and strength of a fault may be reduced by excitation and transport of fluids promoting failure by shear stresses.

6 CONCLUSIONS

Different populations of triggered seismicity indicate different physical mechanisms behind the triggering process. We have delineated regions of triggered seismicity identifying critically stressed regions, particularly susceptible to earthquake hazards associated with sustained fluid injection. In the context of dynamic triggering Oklahoma is dominated by delay triggered events. We attribute this dominance to anthropogenic exploitation of the region. Altering the natural stress of these areas may have pushed localized regions of Oklahoma into a critical state, easily triggered by remote transient stresses. Regions susceptible to delayed dynamic triggering may indicate fluid diffusion as a main mechanism, which may be associated with fluid injection and CO2 sequestration. In regions of induced seismicity, delayed-triggered seismicity may indicate area in which CO2 sequestration and fluid injection should be avoided.

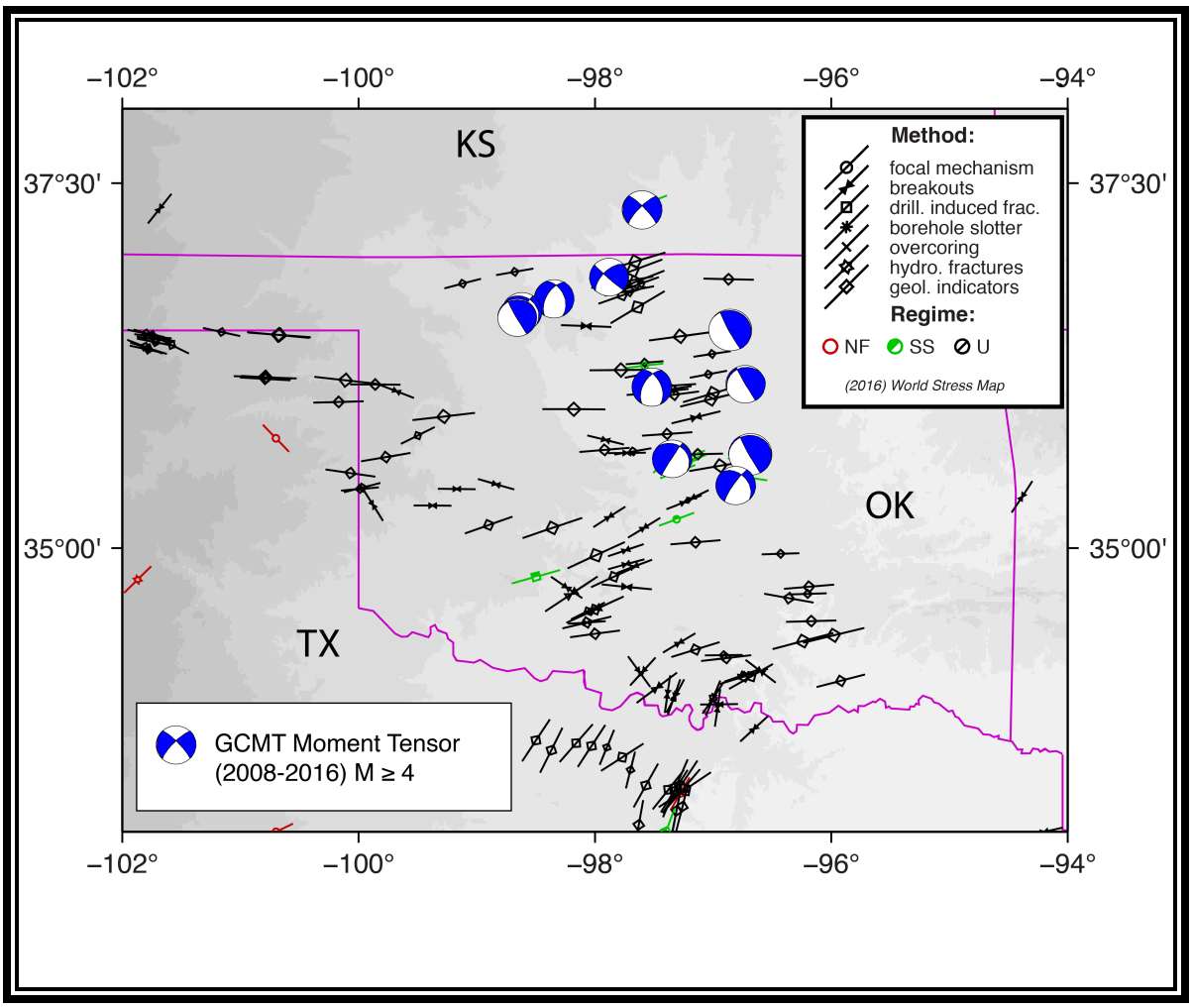

Figure 1.3: Map of region stress in Oklahoma and surrounding region. We display world stress map data and moment tensors calculated for local seismicity M ≥ 4. Stress map data indicates the local in the stress field for our study area. Stress data retrieved from The World Stress Map database (last accessed 11/2017) [Heidbach et al., 2016].

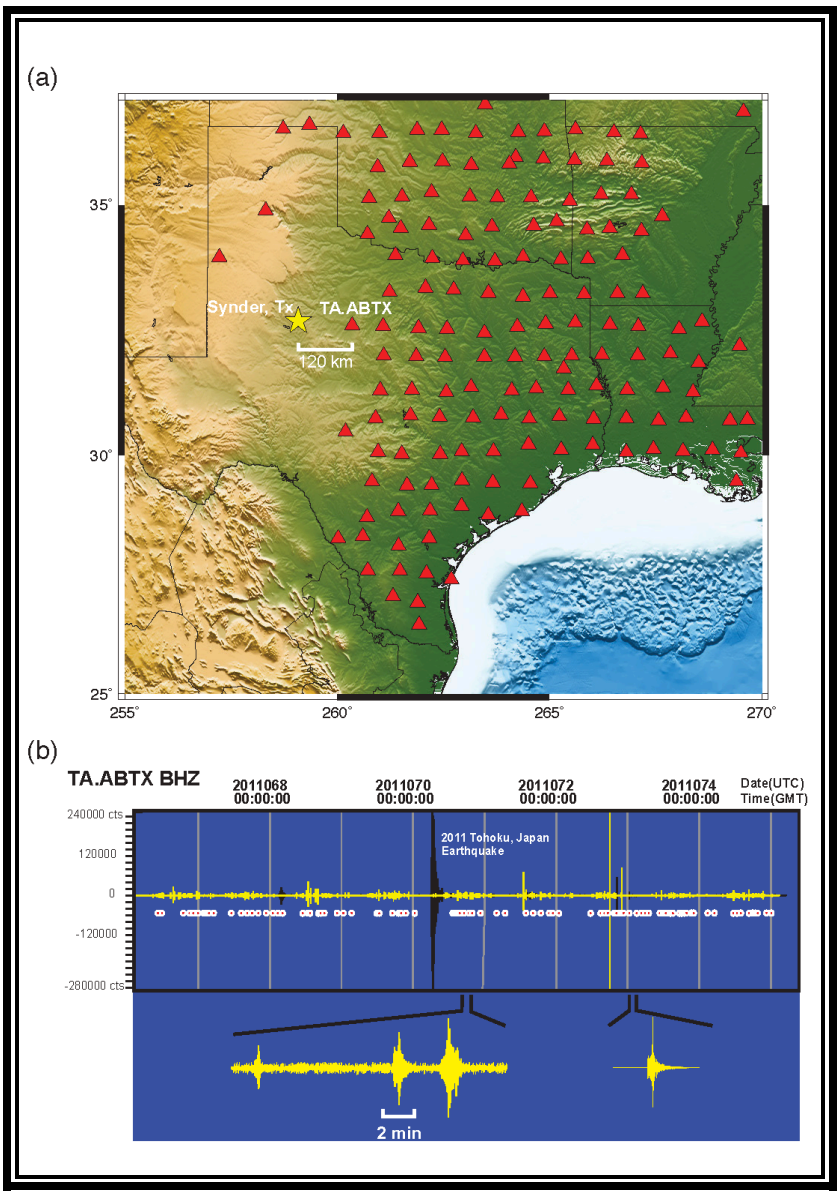

Figure 2.3 A) Operational USArray Transportable Array (TA) stations and regional seismic network stations at the time of the 11 March 2011 05:46:24 (UTC) Tohoku Japan (M 9.0) earthquake. Synder, Texas (star) where remotely triggered earthquakes were reported (van der Elst et. al., 2013). B) Seismogram (BHZ component) from TA station ABTX, which is the closest TA station Synder, TX, showing 9-days of data (4-days before and 5-days after the Tohoku mainshock). Juxtaposed on the raw data (dark hue waveforms; Tohoku mainshock labeled) is 5Hz high-passed data (light hue waveforms). Circles indicate Ev1 detections (Table 1). Zoom highlights examples of locally triggered earthquakes detected by the Ev1 detector. The Ev1 detector successfully identifies events triggered by the Tohoku Japan (M 9.0) earthquake, however because these triggering events were off-array manual review is required to flag these detections as remotely triggered aftershocks. (Modified from Velasco et al., 2016).

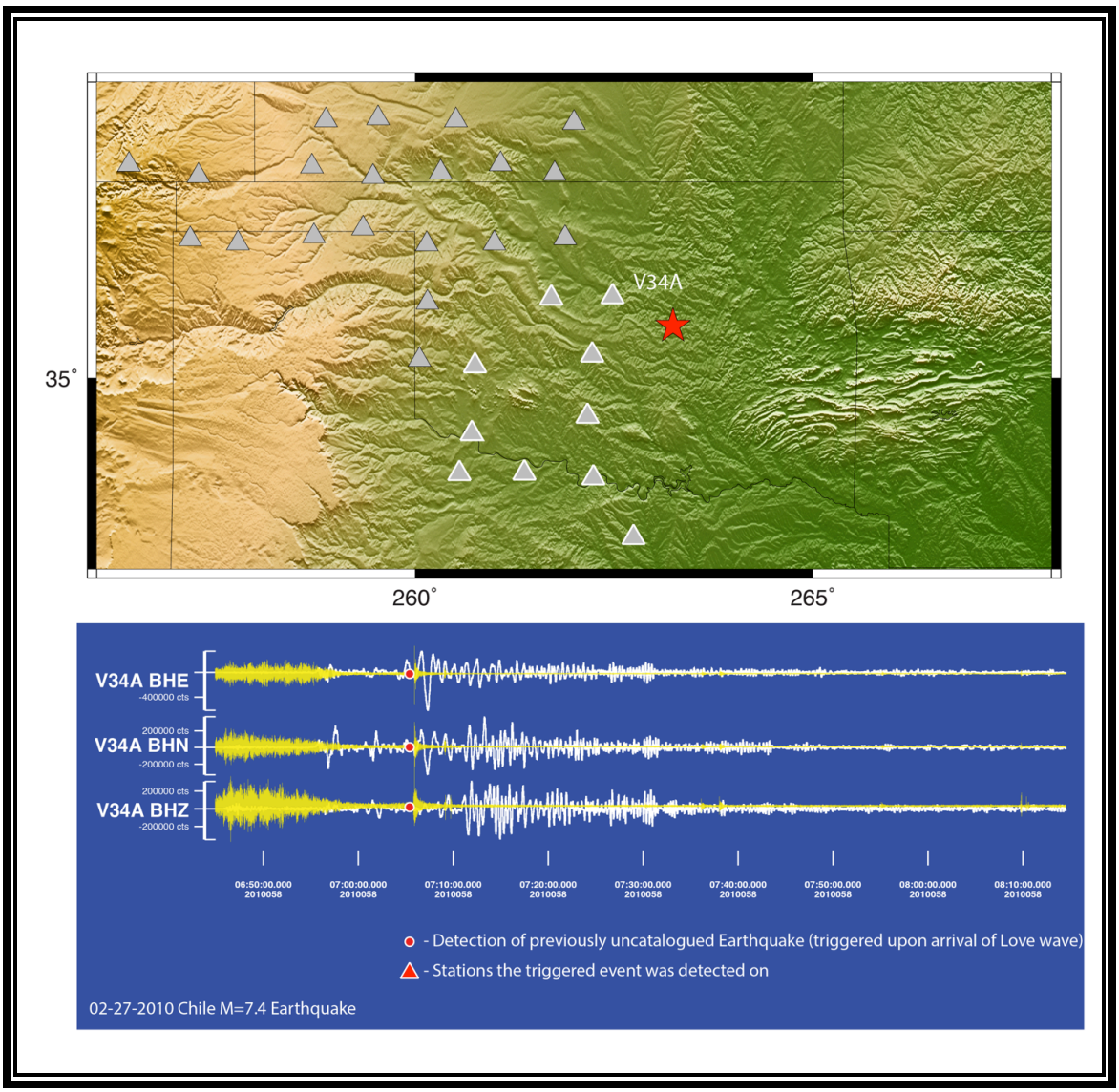

Figure 3.3 (top) Map showing locations of USArray stations (red triangles) recording a M=7.4 earthquake in Chile (2-20-2010). (bottom) Small uncataloged earthquake triggered that appears to be triggered by Love waves in Oklahoma recorded on USArray stations V34A. High-pass filtered traces (yellow traces) show the small earthquake and the raw waveforms (white traces) show the surface waves.

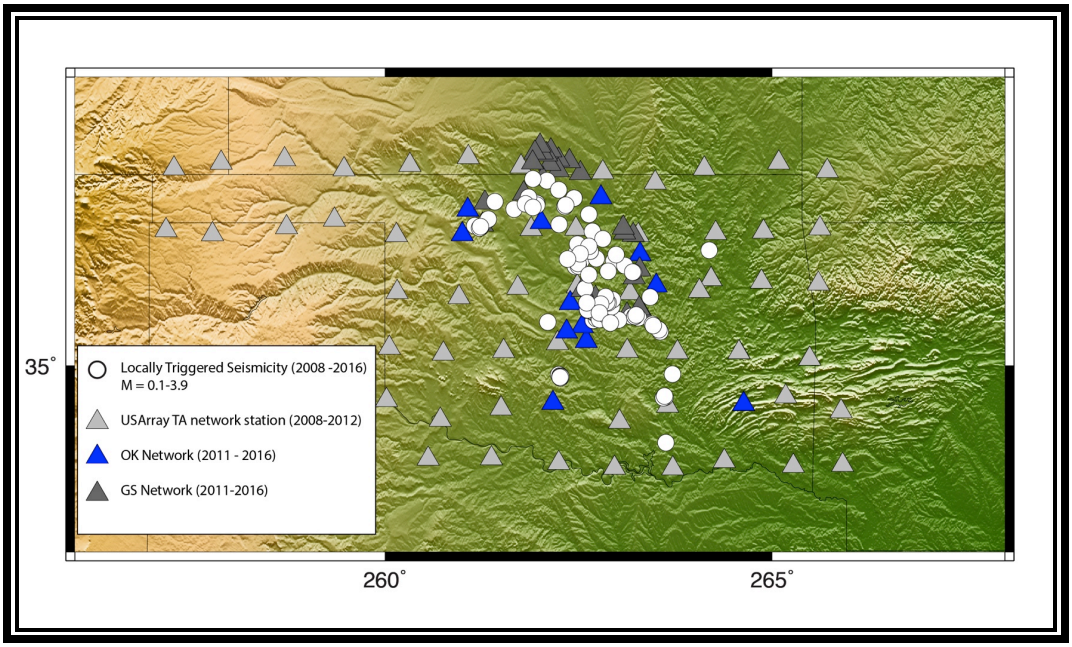

Figure 4.3 Map of locally triggered seismicity in Oklahoma. White circles indicate locations of 106 remotely triggered local earthquakes events range in magnitude (ML) 0.01-4.1.

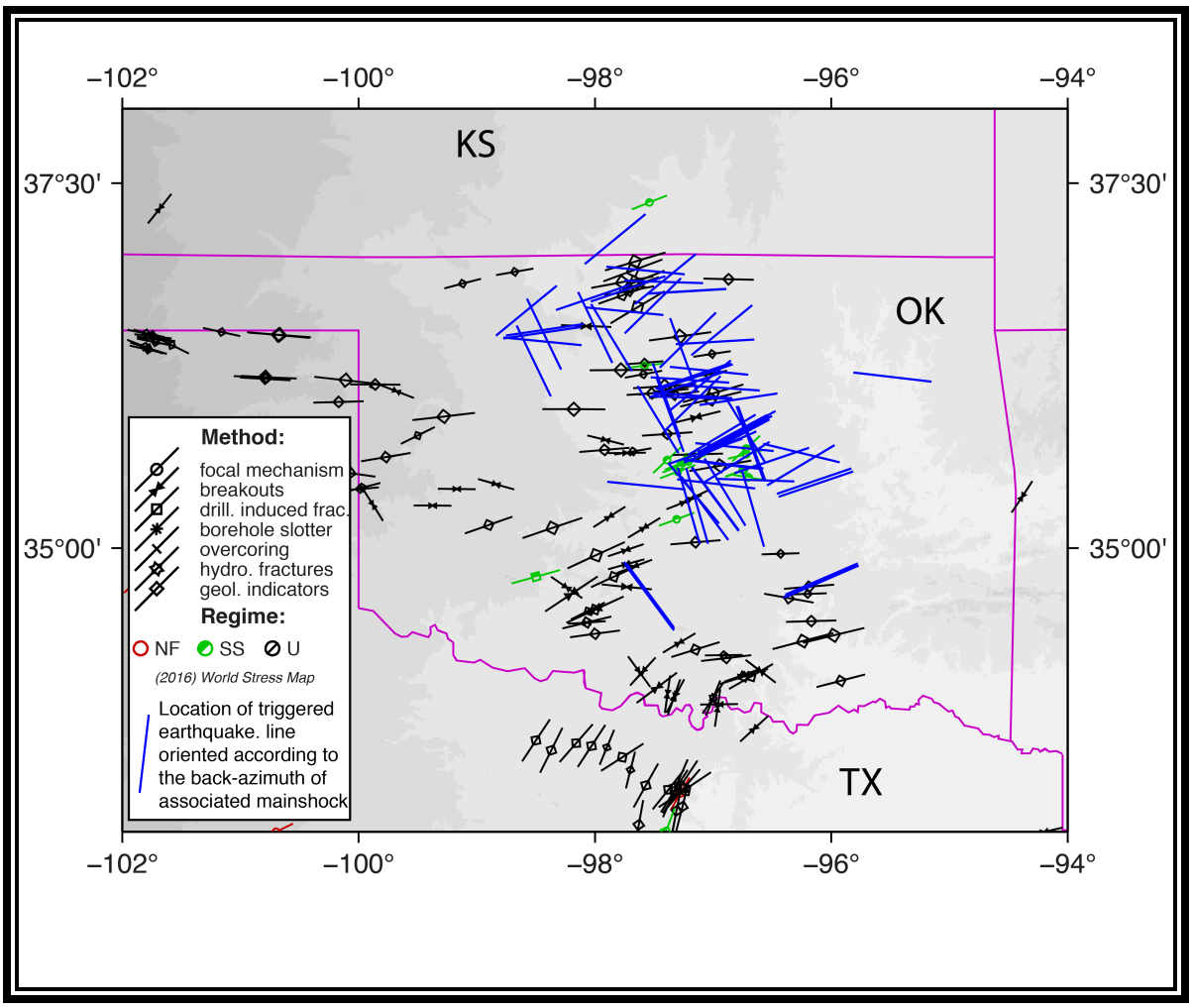

Figure 5.3 Map of region stress in study area. We display world stress map data and locally triggered earthquakes as lines oriented according to back-azimuths associated with triggering mainshocks. Stress map data indicates the local in the stress field for our study area. Stress data retrieved from The World Stress Map database (last accessed 11/2017) [Heidbach et al., 2016]. The location of locally triggered earthquakes are depicted as blue lines, where the line orientation indicates the back-azimuth direction of the associated triggering mainshock. Stress data retrieved from The World Stress Map database (last accessed 11/2017) (Heidbach *et al*., 2008).

.

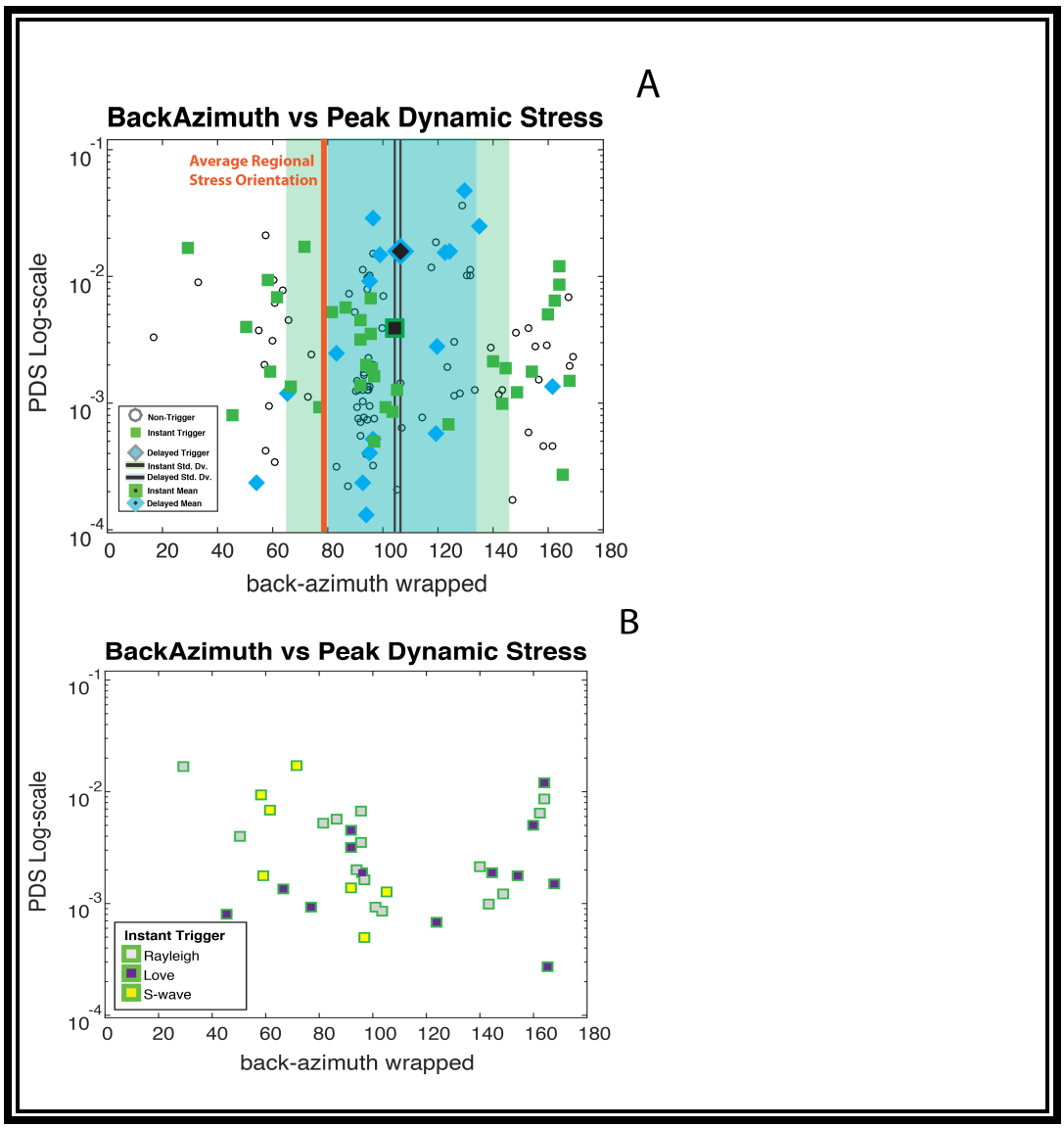

Figure 6.3 Map of region stress in study area. We display world stress map data and locally Analysis of 144 M ≥ 7 mainshock earthquake parameters 2008-2016. A) Plot of mainshock back-azimuth orientations versus PDS measured at the Oklahoma. The back-azimuth of each event is wrapped so that North and South and East and West are equivalent. Average mainshock PDS values from recordings at 5 stations, for both non-triggering mainshocks and triggering mainshocks range between values of (10-4–10--1 MPa). Green indicates a mainshock earthquake that instantaneously triggered seismicity in the Oklahoma. Blue indicates a mainshock earthquake that triggered seismicity after a delayed period of time in the Oklahoma. The standard deviation of instantaneous triggering and delayed triggering are shown as green and blue boxes respectively. B) Instantaneously triggered events are further subdivided into triggering wave types (S-wave, Love wave, Rayleigh wave). Instantaneously triggered events are not constrained to a specific azimuthal range related to the orientation of the stress field in the Oklahoma.

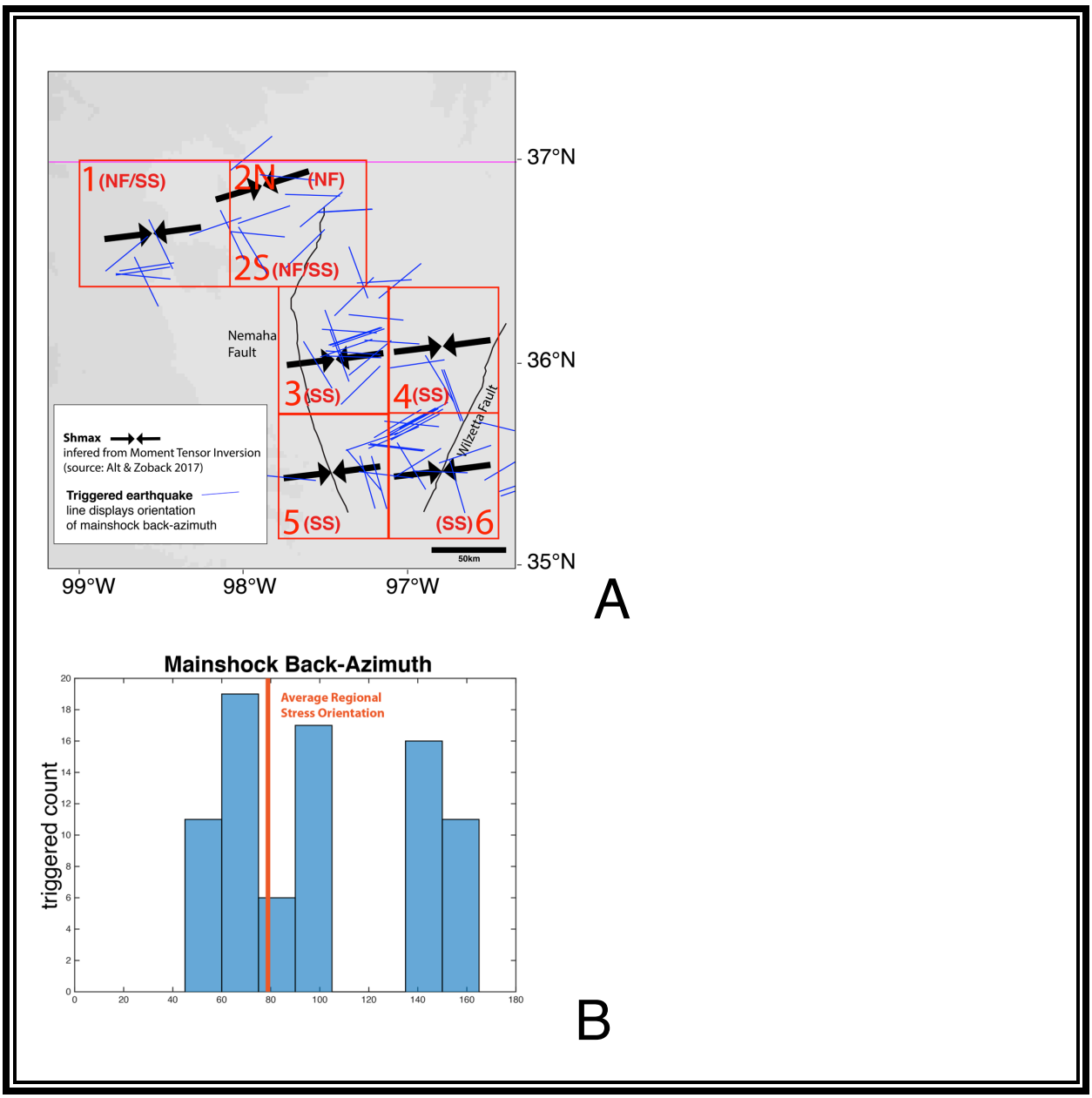

Figure 7.3 A) Map of local stress regimes in Oklahoma as defined in Alt & Zoback (2017) NF = Normal Faulting, SS= Strike Slip Faulting regimes. We display locally triggered earthquakes as blue lines orientation indicates the back-azimuth direction of the associated triggering mainshock. Note that several events align favorably (approximately perpendicular) with the local stress field and/or orientation of faults in the Oklahoma region. B) Indicates the distribution of back-azimuth orientations as a count of locally triggered earthquakes. Note that there is a Bimodal distribution in which several events align favorably (approximately perpendicular) with the local stress field, while others diverge from this trend. The triggered events that diverge from this trend may be due to anthropogenic injection and extraction activity has altered the stress state and fluid flow within the region.

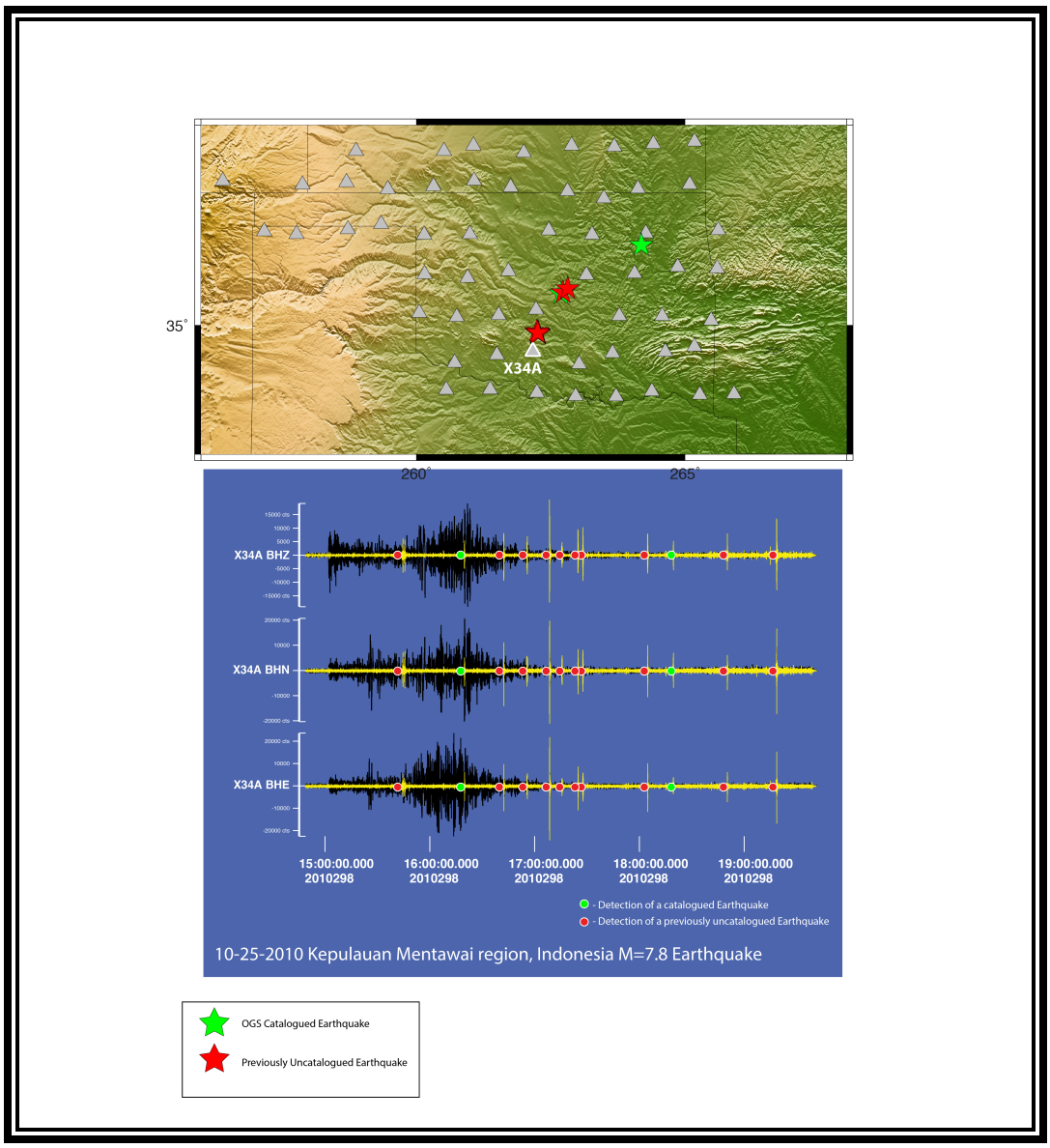

Figure S1.3 (top) Map showing locations of USArray stations (red triangles) recording a M=7.8 earthquake in Indonesia (10-25-2010). (bottom) Small cataloged and uncataloged earthquakes triggered that appear to be triggered by Love and Rayleigh waves in Oklahoma, also shown are delayed triggered events recorded on USArray stations X34A. High-pass filtered traces (yellow traces) show the small earthquake and the raw waveforms (white traces) show the surface waves.

References

Alt, R. C., & Zoback, M. D. (2017). In Situ Stress and Active Faulting in OklahomaIn Situ Stress and Active Faulting in Oklahoma. Bulletin of the Seismological Society of America, 107(1), 216–228. https://doi.org/10.1785/0120160156

Brodsky, E., and S. G. Prejean (2005), New constraints on mechanisms of remotely triggered seismicity at Long Valley Caldera, Journal of Geophysical Research, 110(B4).

Brodsky, E. E., V. Karakostas, and H. Kanamori (2000), A New Observation of Dynamically Triggered Regional Seismicity: Earthquakes in Greece Following the August, 1999 Izmit, Turkey Earthquake, Geophysical Research Letters, 27(17).

Chao, K., Z. Peng, H. Gonzalez-Huizar, C. Aiken, B. Enescu, H. Kao, A. A. Velasco, K. Obara, and T. Matsuzawa (2013), A Global Search for Triggered Tremor Following the 2011 Mw 9.0 Tohoku Earthquake, Bulletin of the Seismological Society of America, 103(2B), 1551–1571, doi:10.1785/0120120171.

Ellsworth, W., A. Llenos, A. McGarr, A. Michael, J. Rubinstein, C. Mueller, M. Petersen, and E. Calais (2015), Increasing seismicity in the U. S. midcontinent: Implications for earthquake hazard, The Leading Edge, 34(6), 618–626, doi:10.1190/tle34060618.1.

Ellsworth, W. L. (2013), Injection-Induced Earthquakes, Science, 341(6142), 1225942, doi:10.1126/science.1225942.

Van der Elst, N. J., H. M. Savage, K. M. Keranen, and G. A. Abers (2013), Enhanced Remote Earthquake Triggering at Fluid-Injection Sites in the Midwestern United States, Science, 341(6142), 164–167, doi:10.1126/science.1238948.

Gomberg, J., M. L. Blanpied, and N. M. Beeler (1997), Transient triggering of near and distant earthquakes, Bulletin of the Seismological Society of America, 87(2), 294–309.

Gomberg, J., P. A. Reasenberg, P. Bodin, and R. A. Harris (2001), Earthquake triggering by seismic waves following the Landers and Hector Mine earthquakes, Nature, 411(6836), 462–466, doi:10.1038/35078053.

Gomberg, J., P. Bodin, and P. A. Reasenberg (2003), Observing Earthquakes Triggered in the Near Field by Dynamic Deformations, Bulletin of the Seismological Society of America, 93(1), 118–138, doi:10.1785/0120020075.

Gomberg, J., P. Bodin, K. Larson, and H. Dragert (2004), Earthquake nucleation by transient deformations caused by the M = 7.9 Denali, Alaska, earthquake, Nature, 427(6975), 621–624, doi:10.1038/nature02335.

Guilhem, A., Z. Peng, and R. M. Nadeau (2010), High-frequency identification of non-volcanic tremor triggered by regional earthquakes, Geophys. Res. Lett., 37(16), L16309, doi:10.1029/2010GL044660.

Hill, D. P. et al. (1993), Seismicity Remotely Triggered by the Magnitude 7.3 Landers, California, Earthquake, Science, 260(5114), 1617–1623, doi:10.1126/science.260.5114.1617.

King, G. C. P., R. S. Stein, and J. Lin (1994), Static stress changes and the triggering of earthquakes, Bulletin of the Seismological Society of America, 84(3), 935–953.

Matthews, M. V., and P. A. Reasenberg (1988), Statistical methods for investigating quiescence and other temporal seismicity patterns, PAGEOPH, 126(2-4), 357–372, doi:10.1007/BF00879003.

McNamara, D. et al. (2015), Efforts to monitor and characterize the recent increasing seismicity in central Oklahoma, The Leading Edge, 34(6), 628–639, doi:10.1190/tle34060628.1.

Pankow, K. L. (2004), Triggered Seismicity in Utah from the 3 November 2002 Denali Fault Earthquake, Bulletin of the Seismological Society of America, 94(6B), S332–S347, doi:10.1785/0120040609.

Parsons, T., J. O. Kaven, A. A. Velasco, and H. Gonzalez-Huizar (2012), Unraveling the apparent magnitude threshold of remote earthquake triggering using full wavefield surface wave simulation, Geochem. Geophys. Geosyst., 13(6), Q06016, doi:10.1029/2012GC004164.

Peng, Z., D. P. Hill, D. R. Shelly, and C. Aiken (2010), Remotely triggered microearthquakes and tremor in central California following the 2010 Mw 8.8 Chile earthquake, Geophys. Res. Lett., 37(24), L24312, doi:10.1029/2010GL045462.

Petersen, M.D., Mueller, C.S., Moschetti, M.P., Hoover, S.M., Rubinstein, J.L., Llenos, A.L., Michael, A.J., Ellsworth, W.L., McGarr, A.F., Holland, A.A., and Anderson, J.G., 2015, Incorporating induced seismicity in the 2014 United States National Seismic Hazard Model—Results of 2014 workshop and sensitivity studies: U.S. Geological Survey Open-File Report 2015–1070, 69 p., http://dx.doi.org/10.3133/ofr20151070.

Reasenberg, P. A., and R. W. Simpson (1992), Response of regional seismicity to the static stress change produced by the loma prieta earthquake, Science, 255(5052), 1687–1690, doi:10.1126/science.255.5052.1687.

Schoenball, M., N. C. Davatzes, and J. M. G. Glen (2015), Differentiating induced and natural seismicity using space-time-magnitude statistics applied to the Coso Geothermal field, Geophys. Res. Lett., 42(15), 2015GL064772, doi:10.1002/2015GL064772.

Stein, R. S., G. C. P. King, and J. Lin (1992), Change in Failure Stress on the Southern San Andreas Fault System Caused by the 1992 Magnitude = 7.4 Landers Earthquake, Science, 258(5086), 1328–1332, doi:10.1126/science.258.5086.1328.

Stein, R. S., G. C. P. King, and J. Lin (1994), Stress Triggering of the 1994 M = 6.7 Northridge, California, Earthquake by Its Predecessors, Science, 265(5177), 1432–1435, doi:10.1126/science.265.5177.1432.

Velasco, A. A., S. Hernandez, T. Parsons, and K. Pankow (2008), Global ubiquity of dynamic earthquake triggering, Nature Geosci, 1(6), 375–379, doi:10.1038/ngeo204.

Velasco, A. A., R. Alfaro-Diaz, D. Kilb, and K. L. Pankow (2016), A Time Domain Detection Approach to Identify Small Earthquakes within the Continental United States Recorded by the USArray and Regional Networks, Bulletin of the Seismological Society of America, 106(2), 512–525, doi:10.1785/0120150156.

Zhang, Q., G. Lin, Z. Zhan, X. Chen, Y. Qin, and S. Wdowinski (2017), Absence of remote earthquake triggering within the Coso and Salton Sea geothermal production fields, *Geophys. Res. Lett.*, *44*(2), 2016GL071964, doi:10.1002/2016GL071964.

Chapter 4: Paleoseismology of the East Franklin fault: Implications for Urban Seismic Hazards in El Paso, TX and Juarez, Chihuahua, MX

Over 2.3 million people inhabit the El Paso-Juarez metropolitan area, a region that faces potential local seismic hazards related to the East Franklin Mountains fault (EFMF). The region is associated with low-level (M<4) seismicity, most recently a M=2.5 earthquake in March of 2012 located within the city limits of El Paso. Both El Paso and Juarez are located within the Rio Grande rift and are built upon Quaternary faults that pose a seismic hazard to the local population. To further assess seismic hazards in the region we conducted a paleoseismologic trenching study at a site in the main urban section of the EFMF fault system to characterize its mid-late Quaternary slip history. A paleoseismic trench was excavated across the East Franklin Mountains Fault at the McKelligan Canyon stepover on the only undisturbed section of the fault within the urbanized section of the fault. The trench site lies just east of Beaumont Medical center (BMC) on a 6.5-m high piedmont scarp about 1 km east of the range front. The trench exposed a spectacular exposure of the fault surface with a series of antithetic splays off the main fault as well as two minor subsidiary faults in the hanging wall. The excavation penetrated through a series of fault-related colluvial wedges in the hanging wall, into underlying alluvial fan strata that we correlate to alluvial fan strata exhumed in the footwall. Our field analysis of the trench leads to an interpretation of 5 colluvial wedges suggestive of ~1m of slip/event, with repeated patterns of surface rupturing suggestive of near-surface, subvertical mode-1 tensile fractures within the hanging wall developing into coseismic keystone graben at the fault scarp.

1 INTRODUCTION

Understanding the slip history of faults remains a key factor for understanding the seismic hazard and tectonic history of a region. The East Franklin Mountains Fault (EFMF) in El Paso, TX is an example of a fault posing a significant seismic hazard with a potential for Earthquakes of M6.5-7.0 (USGS Ref) in an area with little, if any seismic preparedness. To address the slip history of the EFMF, we conducted a paleoseismic investigation to estimate the characteristic earthquake

magnitude, slip rate, and recurrence interval for this structure. In this chapter we focus on the central segment of the EFMF to characterize the mid-late Quaternary activity of the fault. Our efforts build upon previous investigations in the region (Keaton et al., 1995; Keaton and Barnes, 1996; McCalpin 2006) to derive a paleoearthquake chronology and magnitude estimates for the EFMF (Figure 1).

2 TECTONIC SETTING

The Franklin Mountains dominate the skyline of the city of El Paso and separate the city into its two parts. An active fault, the East Franklin Fault, bounds the range to the east. Related, and potentially linked normal faults extend both to the south to the Sierra Juarez. The Franklin Mountains are one manifestation of a nearly continuous series of approximately north-south trending ranges that define the actively extending Rio Grande Rift. Geodetic studies indicate the southern Rio Grande rift is extending at a relatively low rate of 4-5 1.2 mm/yr (Berglund et. al., 2012).

The bedrock geology of the Franklin Mountains and basic structure of adjacent basins are well known, primarily from a series of theses and dissertations at the University of Texas at El Paso (e.g. Stacy, 1991; Fetzner, 1992; Wu, 2002; Scharmann, 2005) and related efforts (e.g. compilations of Collins et al, 1996). In the simplest sense, the Franklin Mountains are a fault-bounded, west-tilted homocline of Paleozoic strata depositionally overlying Proterozoic crystalline basement. The EFMF forms the eastern boundary of this homocline (Figure 2), and the deepest part of the Hueco basin (aka Hueco Bolson) lies immediately to the east of the Franklin Mountains (Collins and Raney, 2000) which suggests strongly that the EFMF bounds a west-tilting basin-range pair. This inference is supported by a low-angle (~30°) bedrock fault surface of a now inactive strand of the EFMF exposed by quarry operations in the center of the range (Pavlis,

unpublished field observations, 2014). Similarly, low-angle, gently-east-dipping normal faults have been mapped in the northern Franklin Mountains (e.g. earlier references; Scharmann, 2005; Pavlis and Hurtado, unpublished mapping). Collectively, these bedrock structures indicate progressive west tilting of the range during Neogene extension resulting in at least 30° and possibly as much as 50° rotation through the entire extensional period (upper half, Figure 3). Differential uplift of Pleistocene terraces across the range suggests this range tilt continues today (Armour-Finch, 2014). Armour-Finch (2014) also showed that terrace offsets along the EFMF approach zero near the present northern and southern boundaries of the Franklin Mountains and mimic the summit elevations of the range. This observation is potentially critical to seismic hazard assessment because it implies the present trace of the EFMF is a single, active fault segment that tips out at the limits of the present day Franklin Mountains. Thus, if the terrace data apply to fault segmentation and earthquake occurrence, the maximum earthquake magnitude is limited by this ~30km segment.

This view of the Franklin Mountains as a simple, tilted extensional fault block is complicated, however, by other observations. The western escarpment of the range contains a west-dipping normal fault that partially reactivates and cuts across, an older, Laramide thrust fault (Colins and Raney, 2000). The thrust system indicates that part of the range tilt may be inherited from Laramide deformation, and the normal fault reactivation indicates the range is not a simple tilt block, but instead is an asymmetric horst block. Nonetheless, there seems little doubt that the EFMF is the main normal fault within this fault system, and the range tilt has important bearing on the seismic hazard. Specifically, although Collins and Raney (2000) show a steep fault dip (~60°) for the EFMF, the successive west tilt of the range and the bedrock fault exhumed by quarrying indicate the range itself may be rotating above a master detachment fault (Figure 3).

The low-angle fault hypothesis is important from a seismic hazards perspective because a complex array of Quaternary scarps occurs within the Hueco Bolson, scattered through Ft. Bliss and east El Paso (Figures 1 and 3). These scarps show variable asymmetries (east and west side down) and displace the Quaternary surface by as much as 20-30m, but it is unclear if these faults relate directly to the EFMF or are independent faults. Collins and Raney (2000) show these faults as independent structures, but, if the EFMF is the master fault or part of a detachment system (Figure 3), these faults may move in direct response to the EFMF. A recent M ~2.5 earthquake (Figure 2) was located along one of these structures illustrating the significance of this issue. Presently there is virtually no information constraining this problem other than subsurface information from geophysics and water well drilling in the Hueco Basin (Avila et. al., 2016).

3 METHODS

To evaluate the seismic hazard of the EFMF we excavated a 39m long trench across the EFMF in the central section of the fault (Figures 1 and 4a). The trench was excavated with a track hoe to a depth that ranged from 2 to 4m with the deeper portion of the trench limited to the fault hanging wall. The footwall was excavated as a single slot to a depth of ~1.5m. At the fault the trench was extended into the hanging wall by benching to a width of ~ 6 m to depth of ~2 m and the central part of the trench was deepened to form an ~1m wide, 1.5 m deep slot that was shored for safety. The trench walls were manually cleaned and logged using a string grid with the interpretation of the deposits shown in Figures 5 and 6. To aid in the interpretation we also developed a Structure-from-Motion/Multiview Stereo (SM) model of the trench that was georeferenced to 39 markers that were located using a Topcon survey grade GPS with an estimated precision of 10 mm. Permit restrictions for the trench limited the field effort to ~8 days for trench logging and sampling. After completion of the effort, the trench was backfilled with a front-end

loader.

After logging the trench we collected samples for geochronology to constrain the ages of paleoseismic events. We attempted 3 geochronometers: (1) radiocarbon geochronology of organic matter in graben fill that post-dates the most-recent-event (MRE); (2) Optically Stimuated Luminescene (OSL) geochronology of colluvial wedge materials and alluvial fan strata from both the hanging wall and footwall; and (3) U-series geochronology of pedogenic carbonate as well as carbonate minerarlization along the fault slip surface. Radiocarbon dates were obtained from the PaleoResearch Institute in Golden, CO. Bulk samples were floated using a modification of procedures outlined by Matthews (1979). OSL dates were obtained at the Utah State University Lab. The Utah State University Lab follows the latest single-aliqout regenerative-dose (SAR) procedures for OSL dating of quartz sand (Murray and Wintle, 2000, 2003; Wintle and Murray, 2006). U-Series dating was conducted at the University of Texas at El Paso.

4 TRENCHING RESULTS

The trench site lies at 31.821687°N, 106.454405°W, approximately 6 km from the southern tip of the Franklin Mountains (Figures 1 and 2). The trench site lies at the southern end of the main trace of the EFMF where the fault makes an ~1km, right-stepover. To the north the fault scarp is close to bedrock exposures but near the trench site the scarp is entirely within the piedmont alluvial surface and dies out entirely less than 1km to the south in an urbanized segment of the fault trace. The scarp reappears, near bedrock, approximately 1km to the west near the mouth of McKelligan Canyon (Figure 1) and is traceable to the southern tip of the range where it disappears into heavily urbanized terrane and very young deposites of the Rio Grande Valley.

The trench lay just inside the Fort Bliss' Beaumont Medical Center security fence on the north side of Hayes Avenue (Figure 7). A topographic profile obtained prior to excavation (Figure 8) shows the vertical surface offset of the fan surface across the scarp of 6.5 m, projecting the far-field fan slope angle of 3°across the scarp.

4.1 Local geomorphology and Quaternary Geology

The trench site lies on an alluvial fan deposited by McKelligan Creek. Comparing the geomorphology of this fan to the fans mapped by Scherschel (1995) farther north suggests that the McKelligan fan correlates to the Jornada II (or Picacho) geomorphic surface defined by Monger et al (2009). The Jornada II geomorphic surface has an estimated age of Late to middle Pleistocene (75 ka to 150 ka) (McCalpin, 2006).

Scarp incision (Figure 4) suggests that the parts of the uplifted fan between incised gullies were abandoned by active deposition after one or more faulting events and become relict surfaces. This inference is supported by the strong caliche soil developed on the footwall of the scarp as seen both in the trench (Figure 9) and in gullies indicating Stage IV carbonate extends right up to ground surface; i.e., there is no evidence of Holocene or latest Pleistocene deposition on the footwall. In contrast, in the hanging wall there is minimal to no gullying, surface materials are unconsolidated to weakly consolidated, and evidence of deposition is clear.

4.2 Stratigraphy

The trench exposes alluvial fan strata. The footwall stratigraphy is composed of moderately- to well-sorted gravel units, and bouldery debris flows. The hanging wall is composed of heterogeneous, poorly-sorted, scarp-derived colluvium, moderate to well-sorted gravel units, and boulder debris flows. We defined 15 mappable units in the 8-m thick footwall stratigraphic sequence (Figures 5 and 6). The footwall units are subdivided into well-sorted, moderately-sorted,

and poorly-sorted gravels, as well as debris flows. We further subdivided these units as a means to identify and correlate the stratigraphy exposed in the deepened hanging wall section of the trench.

4.3 Footwall

The footwall stratigraphic sequence is well-stratified (Figures 5 and 6). 15 units are exposed on the north wall of the trench and 10 of the 15 units can be traced over the entire 25-m width of the north wall (the other 5 pinching out in the east). Four of the 15 units are well-sorted gravels and seven of the 15 units are moderately-sorted gravels. Both are interpreted as channel deposits of ephemeral streams. Two of the 15 units are poorly-sorted with some matrix support, and they are interpreted as thin debris flows. Two of the 15 units are bouldery debris flows.

Overall, the sedimentology of the footwall indicates a depositional environment fed by both water floods and debris flows, i.e. a composite fan (Figure 9). Deposition at the fan surface was steadily aggrading and dominated by a sheetflood-streamflood environment and intermittent debris-flows. Streamflow deposits are dominant at this site probably because it is located ~1 km east of the range front, so only exceptionally large debris flows would have travelled this far out into the basin. It is likely the EFMF did not move during the deposition of the footwall fan deposits as the sedimentology and thicknesses of identified subunits do not change as they approach and cross the fault.

4.4 Hanging Wall

The hanging wall stratigraphic sequence exposed in the trench is ~6 m thick. We defined 13 mappable units in the hanging wall (Figures 5 and 6). We subdivided these units based on their sedimentology and also degree of soil development (paleosol). The five youngest units are all scarp-derived colluvial packages. Unit CV (youngest) was deposited after the most recent

displacement event and consists of poorly sorted gravel and sand in a brown matrix. The modern surface soil is developed on this unit (Figure 10). Units CI-CIV are colluvium deposited during successive displacement events with some uncertainty associated with internal stratification of these units (see below).

During the logging we labeled the hanging wall units with an H (for hanging wall) to distinguish them from the footwall units because we were not sure our field correlation with footwall strata would stand up in light of the numerical age dates once they were complete. Alluvial units H14-H10 underlie the scarp-derived colluvium units and consist of thick, stratified deposits including well-sorted, medium-large gravels (units H11, H14), matrix-supported gravel (units H10, H13a, H13b), and poorly sorted gravel (unit H12). Unit H15 is a boulder bed debris flow. The hanging-wall alluvial units range from ~0.5 m to 1 m thick, and units (H10-11, H13-15) can be directly correlated to footwall units (10-11, 13-15) since they represent the same depositional environment as the stream-flood gravels and debris flows exposed in the footwall. In summary, the thicknesses, geometries, and textures of hanging wall beds H10-11, H13-15 resembles that of footwall beds 10-11, 13-15.

4.5 Soils

The soil profiles preserved in the footwall are very different from those preserved in the hanging wall. This is primarily because the footwall is a stable geomorphic surface of late to middle Pleistocene age (Jornada II, 75,000 to 150,000 years old) whereas episodic scarp-derived deposition has continued on the hanging wall side up through the late Holocene. Incision into the scarp and cessation of local fan deposition should have occurred soon after the oldest faulting event on the eastern piedmont scarp, consistent with the soil development seen in the trench. The profile is dominated by a K horizon about 1-m thick, which is a bit thicker than the average II K

horizon. We did not make a detailed profile description at the trench to compare with the type section, because we were not going to use soil profile development to date the surface, relying instead on OSL dating (see Sect. 4.3.4). However, OSL dating may be affected by the long time period (75-150 ka) over which eolian dust and dissolved calcium carbonate could have trickled down through the soil profile.

The hanging wall soil profile consists of four or five superimposed soils, each developed on a scarp-derived colluvial wedge. The youngest colluvial wedge (CV) is so young that it shows no soil horizon and no carbonate deposition. All the underlying colluvial wedges are completely impregnated with secondary soil carbonate (Stages III-IV of Gile et al, 1981). Impregnation is so complete that it has nearly obscured the depositional contacts between colluvial wedge units. This phenomenon occurs where colluvial wedge deposits are thin and the time between their deposition is long; i.e. 10s of kyr between earthquakes. In this case, there is enough time for the carbonate horizon in the youngest colluvial wedge to envelop the entire unit, "welding" itself onto the top of the carbonate soil of the underlying colluvial wedge. If no basal stone lines can be seen at the base of each colluvial wedge, the carbonate overprint can make identifying individual colluvial wedges very difficult (McCalpin et al., 2011). Fortunately, the scarp free faces that formed episodically at our site exposed gravelly alluvial fan deposits, which released gravel into the basal part of each proximal wedge deposit, making subdivision based on stone lines possible.

4.6 Structure

The trench exhumed a spectacular exposure of the main fault surface together with its associated damage zone as well as 3 subsidiary faults in the hanging wall (Figures 5 and 6). The main fault was marked by a clear, discrete slip surface in the lower 2/3 of the trench (Figures 11 and 12) and was recognizable in the footwall as the paleo-free face of the latest seismic event and

colluvial wedge V. The slip surface dips steeply to the east (75°) and strikes 010, obliquely to the trench which trends E-W (Fig. 10), despite the trench's orientation perpendicular to the fault scarp. Due to this slight obliquity, the main fault plane on the south wall of the trench was exposed in the approximate center of the fault scarp, but on the north wall of the trench the fault daylighted several meters downslope of the scarp midpoint. Thus the 5 m-deep trench exposed four deeper, older footwall alluvial fan units in the lower north wall (uncolored polygons in Figure 6) that were not exposed in the lower south wall (Figure 5).

Below colluvial wedge V, the fault slip surface is conspicuously slickensided (Figure 13) with downdip slickenlines developed in a 1-2mm thick calcite vein parallel to the slip surface (Figure 12). This calcite vein is clearly associated with soil carbonate development, and is interpreted as a fracture that opened during multiple seismic events, but was soon filled and sealed following each event. Thus, the carbonate in the vein presumably records multi-cycle infillings in the deeper parts of the trench.

The fault slip-surface is within a 1- to 2-m wide damage zone. The damage zone is the product of a combination of surficial processes associated with seismic slip and the development of mode-1, tensile fractures that emanate from the main fault. The damage zone is marked by extensive carbonate cementation, which presumably results from increased near-surface permeability enhanced by co-seismic fracturing and brecciation, which allowed increased water infiltration and associated calcrete development.

Deposits related to the latest seismic event (unit CV), and structures associated with it, provide the best evidence for interpretation of the fault damage zone. Unit CV is the conspicuous dark-colored fill material in Figure 11, and, in addition to forming a colluvial wedge, this unit shows a conspicuous V-shaped base centered in the hanging wall of the main fault slip surface.

The dark fill material comprises both organic rich soil and loose cobbles. This dark fill material is bounded to the east by a conspicuous slip surface which represents an antithetic slip surface to the main fault. In addition, there is a distinct subvertical fissure that splays into smaller subordinate fractures (Figure 11). We interpret these features to be direct products of surface rupturing during the last seismic event. The antithetic fault and the subvertical fissure almost certainly imitated as mode-1 tensile fractures as the rupture reached earth's surface. As coseismic slip progressed rapidly on the free-face, opening of the mode-1 fractures produced a surface void that collapsed to form the v-shape of colluvial unit V, converting the mode-1 fracture into the antithetic slip surface that bounds the V-shaped fill.

While a similar faulting pattern is recognized at deeper intervals within the trench, a superposition of slip requires a more complicated interpretation. Specifically, a series of antithetic faults splay from the main fault, but all bound gravity fill packages containing loose stones and associated colluvial material or, in the case of the north trench wall, a distinct keystone block comprised of hanging-wall strata (Figure 6). The hanging wall strata in the keystone block, however, do not provide significant chronostratigraphic control because they comprise pre-faulting, alluvial fan deposits. Nonetheless, the north trench wall (Figure 6) does show cross-cutting relationships among the antithetic faults that show a succession of wedges with an older fault to the east that cuts CI and CII, but that is overlapped by the younger part of CII, whereas a younger, structurally higher antithetic fault to the west cuts CII and CIII but is itself overlapped by CIV.

In addition to the main fault and its associated antithetic faults, we recognize three small synthetic faults in the hanging-wall of the main fault (F2, F3, and F4 in Figure 6). F2 is subvertical and lies in close proximity to the main fault, but it terminates at the base of the oldest colluvial

wedge (CI). Thus, F2 is either a fissure generated during the first seismic event that generated C1, or F2 pre-dates all of the slip events recognized in the trench. F3 and F4 lie 5 m and 7 m, respectively, to the east of the main fault, and they are both subvertical faults with slip of only a few cm. Indeed, slip of F4 is so small that the fault is not even recognizable on the north trench wall, indicating it tips out within the trench.

The normal fault that formed the surface fault scarp is well-exposed in the center of the trench (Figures 11 and 12). On the south wall, the fault has an apparent dip of 75°E and is planar over the depth of the trench (~5 m). The fault is expressed as a 1-3 cm-wide fissure filled with soft, noncalcareous brown sand, in contrast with the carbonate-impregnated footwall and hanging wall. This sand is probably mostly inwash from the surface into an open void space along the fault.

5 GEOCHRONOLOGY

5.1 Radiocarbon and OSL dating

Based on previous trenching on the EFMF in 2003 (McCalpin, 2006) we anticipated difficulty in obtaining datable material. Therefore we employed three dating methods to constrain ages of seismic events: radiocarbon (^{14}C), optically-stimulated luminescence (OSL), and uranium series disequilibrium (U-series).

The only stratigraphic unit that was not engulfed by pedogenic calcium carbonate was unit CV, the colluvial wedge deposited after the Most Recent Event (MRE). This is also the only unit that contained visible charcoal appropriate for ^{14}C geochronology. We collected three samples from CV (Figure 5) but one was too small to date. The other two samples were taken from close to the base of unit CV, and were very small samples of charred stems. They yielded unexpectedly young dates of ~500 and ~1000 years BP (Table 1).

We collected 8 OSL samples, 5 from the colluvial wedge sequence and 3 from pre-faulting alluvial fan gravels. All five OSL samples obtained from the colluvial wedge package yielded dates in the correct stratigraphic order, ranging from 39.9 ka in unit CIV to 82.0 ka in unit CI (Figure 5 and Table 2). In the pre-faulting alluvial fan section, the oldest OSL date is 108 ka (from hanging wall unit H14, about 1 m below the bottom of the colluvial wedge sequence). The second-oldest OSL age(78 ka) came from footwall unit 14. However, this sample may have actually been collected from overlying unit 15, which would explain why it is 30 ka younger than hanging wall unit H14. At the extreme east end of the trench we sampled what we thought was alluvial unit H13a (sample EFL-7), which was expected to have been the stratigraphically oldest of the sampled units. However, EFL-7 yielded a date of 62.9 ka, which is younger than the oldest colluvial wedge date (CI, 70-82 ka). During logging we suspected that the lens of sandy gravel sampled might be an inter-event local alluvium deposited at the toe of the fault scarp. Based on this interpretation, we mapped an east-dipping contact (dashed line in Figure 5), which separates tabular fan strata on the west from lenticular strata to the east. The OSL date of 62.9 ka suggests that the first faulting event (V) formed a ~1.4 m-high scarp, after which streams incised into the scarp and deposited channel-facies alluvium at the toe of the scarp. However, this interpretation highlights a problem with our trench log in that the units defined in some places appear to be soil horizons that cross-cut the depositional strata. This has major implications, relative to our five identified colluvial wedges, because some or all of these colluvial wedges may in fact actually be soil horizons. This possibility is discussed below.

5.2 U-Series dating experiment

We collected a total of 21 U-series samples in three vertical transects (one each from correlative alluvial fan strata on the hanging wall and footwall), a vertical transect through the

colluvial wedge sequence, and two samples from within the main fault zone. The colluvial wedge samples came from the south wall (Figure 5), while the alluvial fan samples came from the north wall (Figure 6).

Samples EFU-1 through EFU-7 were collected in a 1.6 m-thick vertical transect at the 30-m horizontal mark (Figures 6 and 14). The sample transect extends from the ground surface down through colluvial units CV, CIV, CIII, and CII. The lowest sample is from what is labeled as H15 on the trench log, although it arguably the sample site could be the very eastern tip of the CI colluvial wedge.

The lab was only able to process three of the seven hanging-wall samples (EFU-3, -4, -5). These samples yielded apparent ages of (from top to bottom): 21.2 ± 5.7 ka (unit CIV), 22.9 ± 6.8 ka (unit CIII), and 24.3 ± 3.8 ka (unit CII). These dates are about half as old as the OSL dates from the same colluvial units: CIV, 39.6 ± 7.4 ka; CIII, 43.8 ± 9.5 ka; CII, 54.7 ± 8.5 ka. The difference probably reflects what each analytical technique is dating. OSL dates the deposition of the clastic sediment, before any soil formation or diagenetic processes occur. In this case, however, the U-series dates the time when carbonates migrated from the ground surface downward, penetrating older units. Since the entire colluvial wedge has been impregnated with caliche, and carbonate from younger caliches has travelled downward into underlying caliches, this process is important in this trench. Notably, McCalpin (2006) found that the radiocarbon dates on bulk soil carbonate on the hanging wall of the EFMF in his 2003 trench farther north were also about half the IRSL dates on the same units. This similarity to the BMC trench suggests that the OSL technique dates sediment deposition, whereas U-series (and radiocarbon) date later soil development processes.

Samples EFU-9 and -10 were collected on either side of the main fault plane exposed on the lower north trench wall, near its top. Sample EFU-10 came from the carbonate-impregnated

gouge zone of the fault, while sample EFU-9 came from a fissure fill between the main fault plane and a forward-toppled block of alluvial fan strata (Figure 15). This poorly-sorted fissure fill was completely engulfed with Stage IV carbonate and its stratigraphic position suggests it was formed during the oldest faulting event exposed here (Event V).

Despite the Stage IV carbonate and stratigraphic indicators of antiquity, EFU-9 yielded a U-series date of 12.1 ± 7.1 ka (Figure 15). This date is younger than all colluvial units except for CV, and stratigraphy and soil development indicate that the fissure must be older than CI or CII (40-70 ka). Sample EFU-10 yielded an even younger date (10.6 ± 0.6 ka) which we interpret as the latest pulse of carbonate migration down the fault zone. Presumably, this would have occurred due to cataclasis of existing carbonate cement during the latest surface rupture, creating a network of open voids for downward infiltration and precipitation of carbonate from the ground surface.

6 DISCUSSION

6.1 Interpretation of the Trench

The trench site for this study is an example of a site with mixed characteristics. On the one hand, it is advantageous because it is near the termination of the surface scarp and therefore individual surface rupture events are relatively small affording a long-term record in this relatively shallow trench. Conversely, however, because the site is near the termination of the surface scarp, within a stepover zone, it is likely that not all earthquakes ruptured through to the tip of the surface scarp; i.e. some events may be missed in the trench. Our analysis of the trench indicates both of these issues are critical for interpretation of the observations.

In paleoseismic investigations it is important to clarify confidence in various elements of the interpretation. We are confident of several features found in the trench:

- The faulted fan surface exposed in the footwall is ~75-150 ka, equivalent to the Jornada II surface;
- The OSL ages of the uppermost fan deposits at the trench site range from 78 ka to 108 ka;
- The cumulative vertical surface offset on the EFMF since the development of the faulted fan surface has been 6.5 m;
- The scarp-derived colluvial wedge section was deposited between 82 ka and ~1 ka;
- There are multiple colluvial wedges, as indicated by cross-cutting relationships, and degree of soil development.

Nevertheless, there are two important ambiguities: 1) the exact number of colluvial wedges is open to interpretation and, thus, the number of surface-rupturing events; and 2) correspondingly, the exact displacement per event is debatable.

To estimate the displacement during each surface faulting event we began with the rule of thumb estimate based on the assumption that the free face height is equal to twice the colluvium thickness at the fault (McCalpin, 2009). However, some of the five-colluvial wedges did not thicken toward the fault, but instead thinned toward the fault and pinched out atop the underlying wedge (Figures 5 and 6). This suggests that they are not scarp-derived debris-facies colluvial wedges, but either: (1) wash facies colluvium overlying the debris-facies colluvium within a single wedge; or (2) a soil horizon. The first option is particularly plausible given the evidence from fault geometry that graben developed along the fault during earthquakes and a small gully lay just to the north of the trench site; hence, that stream may have been temporarily deflected along the scarp. In either case, they would not be a separate wedge and would not represent a separate paleoearthquake. This produces the central question for the interpretation of this site: are there five wedges, or just four?

Since the wedges do not all have the same shape, it appears that free face height could not be estimated by simply doubling the maximum colluvium thickness, because that thickness sometimes occurred next to the fault (where it should be), and sometimes at the midpoint of the wedge or closer to the toe. Regardless of the shape of the wedge, its volume should scale more-or-less linearly with the height of the free face from which it was derived. On the 2D trench walls wedge volume is represented by the area of each wedge exposed on the trench wall and on the log.

Table 3 shows the cross-sectional areas of the five colluvial wedges exposed on the south wall. Examining the clast composition within each unit on the trench logs (Figures 5 and 6), it can be seen that some wedges (such as CV) are dominated by clast-poor, sandy wash facies. The cross-sectional area of wash-facies colluvium may be more related to the time between earthquake events (i.e. the time for accumulation), or to eolian input rates, than to the height of the free face. To resolve this uncertainty, we reconstructed the cross-sectional area of only the debris-facies colluvium that was (presumably) derived from erosion of the free face. Complicating this analysis, however, is the formation of coseismic grabens/tension fissures adjacent to the fault, which would have trapped much of the debris-facies colluvium. For some wedges most of the volume of debris-facies colluvium was trapped in a graben, and the rest of the wedge was mostly wash facies. In Table 3 we make consistent assumptions about these processes.

The cross-sectional area of the five wedges (debris facies and fissure fill only) ranges from 2.44 m^2 (unit CIII) to 4.94 m^2 (unit CII). Individual debris wedges constitute 14% to 29% of the total colluvial sequence (mean = 20%, sigma = 6%, coefficient of variation = 0.28). If these percentages can be used as surrogates for the free face height formed in each event (REF), then we can apply them to the cumulative 6.5 m of surface offset to estimate per-event displacements (Table 3). In the 5-event model, this results in per-event displacements from 0.94 to 1.89 m (mean

= 1.3 m, sigma = 0.36 m). The coefficient of variation (COV) of these displacement estimates (0.36) is within the range for COV of fault displacement at-a-point ($\leq$ 0.5), according to Hecker et al. (2013).

We constructed a slip history diagram using the displacements from Table 3 and the OSL (Table 2) and C-14 ages (Table 1) of the post-event colluviums. Figure 16 shows the estimated age and displacement of the five inferred events, totaling 6.5 m of vertical surface offset since 108 ka. The stairstep pattern is quite irregular, with the oldest and youngest closed seismic cycles being long, and the two middle ones being very short. Closed-cycle slip rates are likewise irregular, ranging from 0.03 mm/yr (the Y-Z cycle) to 0.29 mm/yr (the X-Y cycle), or an order of magnitude different.

There are two possible explanations for this high variation. The first is that recurrence intervals have in fact been irregular, perhaps due to ruptures occurring at the trench site from independent segments to both the north and south. However, if a segment boundary is experiencing ruptures that propagate into it from both adjacent segments, one would expect twice as many events at the boundary than in either flanking segment. On the EFMF we have the opposite phenomenon; two of the four seismic cycles are longer than those observed 20 km to the north (McCalpin, 2006).

The second possibility is that not every colluvial wedge we defined in the BMC trench represents an earthquake. Instead, some of these colluvial wedges may be soil horizons or some other type of non-tectonic sedimentation. For example, in our initial interpretation of the trench, wedges CIII and CIV were thought to be a single wedge separated by facies or soil horizons. Explanation 2 proposes that Events X and Y were not separate events, but only a single larger event (XY) that shed a two-facies wedge. This possibility is shown by the red line in Figure 16. Combining Events X and Y into a single event produces a more regular pattern, although the

middle cycle (W to XY) still has a higher slip rate (0.14 mm/yr) than the oldest and youngest cycles (0.03 to 0.07 mm/yr).

The length of the oldest and youngest seismic cycles at BMC are 27 kyr and 40 kyr, respectively, which are both longer than the recurrence interval of 14-18 ka obtained from the trench located about 20 km north site (McCalpin, 2006). One way to explain this pattern is to assume that only half of the rupture events that propagate through the McKelligan stepover cause rupture at the Beaumont trench site; an interpretation we explore below.

6.2 Displacement per Event, Surface Rupture Length, and Paleomagnitude

Displacements per event range from 0.94 to 1.89 m (mean = 1.3 m, sigma = 0.36 m) in the 5 event model to 1.27 to 2.05 m (mean = 1.63 m, sigma = 0.40 m) in the 4 event model. These values are significantly smaller than the per-event displacements measured in the 2003 trench (McCalpin, 2006) 20-km farther north (Table 4).

Because the BMC trench is located near the end of a fault scarp in a stepover zone, displacements there would not be expected to be the maximum in each rupture event. Moreover, surface ruptures may not all have ruptured through. In Table 4 we assume these displacements must have been closer to average rather than the maximum. In contrast, the mean displacements exposed in the 2003 trench in the middle of a long continuous scarp are 166% larger (REF). Thus we assume that they more closely approximate the maximum displacement in each rupture event. Table 4 shows that the surface rupture lengths normally associated with these per-event displacements are very similar at the 2003 (35.2 km) and BMC trenches (37.9 km). Likewise, the magnitudes of the earthquakes at the two trench sites, based on mean displacement-per-event, are virtually identical (M = 6.90 (2003) vs. M = 6.91 (2017)).

Figure 17 shows the locations of the two trenches compared to the Quaternary fault traces of the EFMF. It can be clearly seen that 35-40 km-long surface ruptures implied by the site displacements must span the McKelligan Canyon stepover. For example, a 35 km-long rupture starting at the NM-TX state line would extend south of El Paso and into Mexico. A 35 km-long rupture originating at the northern end of the EFMF fault in New Mexico (as mapped by USGS), would cross the McKelligan stepover and extend nearly to the Rio Grande. Based on our new data, it now seems unlikely that the McKelligan stepover functioned as a segment boundary during the past 4 paleoearthquakes, so it is probably not a persistent segment boundary.

6.3 Recurrence Intervals Between Paleoearthquakes

The new data from this study, together with the 2003 trenching study (McCalpin, 2003) provide a far better estimate on recurrence intervals for earthquakes on the EFMF, subject to details of how the data are interpreted. Estimating recurrence intervals, however, is complicated by two issues: (1) the discordance between the Most Recent Event (MRE) dates at the 2003 and BMC trenches, and (2) the poor precision of age constraints on the older events at both sites.

The first issue is whether the MREs were correctly dated at the two trench sites. Keaton and Barnes (1996) concluded that the MRE must be older than 8 ka, because "*…younger Organ units (< 8 ka) are clearly unfaulted*." Furthermore, they state that "*soil carbonate development suggests that the latest surface faulting earthquake occurred between 9 and 22 ka*." In addition, Keaton and Barns (1996) obtained a ^{14}C date from carbonate in the MRE colluvium in a tension fissure on the main fault of 10,880 ± 70 C-14 yr BP (equivalent to about 12.7 cal ka).

McCalpin (2006) did not find any datable material (radiocarbon or luminescence) in the MRE colluvium (his unit 40). However, he radiocarbon-dated dated bulk carbonate in the colluvial wedge of the penultimate event (PE; his unit 31). McCalpin (2006) found, the youngest

luminescence sample came from unit 31, a block of soil that was downfaulted into the main fault graben during the penultimate event (Event Y). Although that sample also yielded an age in correct stratigraphic order (17.7 ± 2.3 ka), significantly younger than the sample that came from subjacent unit 30 outside the graben (41.3 ± 4.2 ka), and there are no unconformities between those two units as logged. Based on these age constraints McCalpin (2006) inferred an age of 13-17 ka for the MRE.

In the 2003 trench, radiocarbon dates on secondary carbonate were always younger than luminescence ages from the same units (Figure 18). For example, unit 31 (PE colluvium) yielded a date of 9,720 ± 70 C-14 yr BP (11,120-11,200 cal yr BP). This date contradicts the Keaton and Barnes (1996) age of 12,680 cal yr BP for the next younger colluvium (our unit 40), and contradicts their IRSL date from our unit 31 of 17.7 ± 2.3 ka. The most likely explanation is that the secondary carbonate was contaminated by even younger calcium carbonate from above reprecipitating in the dated sample.

In the 2016 BMC trench, our only two radiocarbon dates came from the MRE colluvium (unit CV) from which we have no corresponding OSL dates. We did not find any datable carbon in the older units where all our OSL dates were from, so we cannot quantitatively demonstrate a discordance between the two methods, as at the 2003 trench. However, we have some concern that the two dated radiocarbon samples may be intrusive to the MRE colluvium and thus younger than its age of deposition. This interpretation is consistent with the lack of young fault scarps offsetting Holocene deposits on the EFMF. All maps of Quaternary deposits along the EFMF (Raney and Collins, 1994a, 1994b; Scherschel, 1995; Keaton and Barnes, 1996) show that Holocene alluvial deposits cross the fault zone and contain no scarps, indicating that the latest rupturing event is pre-Holocene. Additional support to our interpretation of the anomalously young radiocarbon dates is

the lack of very steep fault scarp slope segments (bevels) on multi-event scarps on the EFMF. If there had been 1-2 m-high reactivation of these older fault scarps only 500-1200 years ago, all the multi-event scarps should show a prominent, steep bevel in the center of their scarp faces, yet none do. As seen in Figure 19, the fault scarp at BMC is a broad, smooth scarp face with no evidence of a young reactivation bevel.

However, if we discount the 0.5 ka and 1.2 ka radiocarbon dates from the MRE colluvium, we then have no age control on the MRE except that it must be younger than the OSL sample from unit CIV (i.e. <39.9 ka). It is tempting to also say that the MRE must also be younger than the U-series age of unit CIV (21.2 ka), but that age is only half the OSL age from the same unit which we ascribe to carbonate mobility in the soil formation process. A last resort for dating the MRE in the BMC trench, then, is to look at the pair of U-series ages from the fault zone on the north wall, which may date the latest pulse of carbonate migration down the fault zone. Coincidentally, these two U-series ages (10.6 ka, 12.1 ka) are very similar to the radiocarbon age of the MRE colluvium in the 1995 trench of Keaton and Barnes (1996). This may be coincidence, a late Pleistocene age for the MRE would explain why there are no fault scarps in Holocene deposits and the lack of a Holocene bevel on the BMC fault scarp face.

We can calculate an average recurrence for the past 4 events (CI-CV). The 4-event sequence spans 3 recurrence intervals. These 3 intervals post-date unit 14 (80.3 ± 27.1 ka) and end with the MRE (age either 1060-1260 cal yr BP, or ~10.6-12.1 ka). Depending on the age of the MRE, this results in average recurrence intervals of 26.4 ka (with a late Holocene MRE) or 23 ka (with a late Pleistocene MRE).

6.4 Slip Rates

Slip rates are shown graphically in Figure 16. In the 4-event scenario, the middle cycle (W to XY) has a higher slip rate (0.14 mm/yr) than the oldest and youngest cycles (0.03 mm/yr to 0.07 mm/yr). The long-term slip of 0.081 mm/yr is based on 6.5 m slip in 80 kyr. This slip rate is much lower than that obtained for the 2003 trench (0.16 to 0.25 mm/yr), which is not surprising since the 2003 trench was near the center of the fault where scarps are high, and the BMC trench is in a stepover only 520 m from the end of the fault scarp.

7 Implications for Segmentation of the EFMF

Figure 20 compares the slip-history of paleo-earthquakes at the BMC site (black) with that at the 2003 trench site (blue), which ~20 km north of the suspected segment boundary. The black lines and event letters show the MRE as dated by radiocarbon at 0.5-1.2 ka. However, if the radiocarbon samples were intrusive and the U-series ages of 10.6-12.1 ka are used to date the MRE at BMC, then quite a good temporal correspondence emerges between the ages of the four faulting events at the 2016 BMC trench and the four faulting events at the 2003 trench of McCalpin (2006) and Keaton and Barnes (1996)(blue rectangles).

In summary, the displacements per event at both the 2003 and 2016 trenches (1.6 m and 2.6 m, respectively) indicate ruptures 35-40 km long, using the empirical relationships of Wells and Coppersmith (1994). Such long ruptures would have involved the entire mapped length of the EFMF, crossed the McKelligan Canyon area, and occurred at both trench sites, which are only 20 km apart. The luminescence dates from both trenches are quite similar for the older three events, supporting the hypothesis that the EFMF ruptured as a single segment in those events. But if radiocarbon ages at the BMC trench are accurate, then the MRE there would be too young (0.5-1.2 ka) to correlate with the MRE 20 km to the north at the 2003 trench. We suspect that the BMC radiocarbon samples may be intrusive to the MRE colluvium (that is they are much younger than

the deposit). In this case, the next-best age control for the MRE at BMC becomes a pair of U-series ages at 10.6 and 12.1 ka. These latter ages overlap with the age range of the MRE 20 km north. Thus, the simplest explanation of the 2003 and 2016 trenching results is that the EFMF has been composed of a single, 35-40 km-long rupture segment that has ruptured in M 6.9 to M 7.1 earthquakes with an average recurrence interval of about 23-26 kyr. In turn, this implies that this paleoseismic history also applies to the EFMF in downtown El Paso.

Table 1.4 Stratigraphic setting of the radiocarbon (C14) samples from the BMC trench. Sample preparation and dating by Paleoresearch Laboratories, Golden, CO (Appendix 2).

Sample	**Unit**	**Calendar-Corrected age (2σ)**	**Age Constraint** (if samples were not intrusive)
EFC-1	CV	1,060-1,250 cal yr BP	Close minimum age on MRE
EFC-2	CV	500-560 cal yr BP	Close minimum age on MRE

Table 2.4 Final OSL ages from USU Luminescence Lab, 27-APRIL-2017.

Sample num.	USU num.	Depth (m)	Num. of aliquots[1]	Dose rate (Gy/ka)	DE[2] ± 2σ (Gy)	OD3 (%)	OSL age ± 2σ (ka)
EFL01-A	USU-2341	3.3	22 (32)	1.55 ± 0.07	166.82 ± 24.67	30.3 ± 5.8	**107.96 ± 19.02**
EFL02-A	USU-2342	1.9	17 (24)	1.41 ± 0.07	115.33 ± 18.54	30.5 ± 6.1	**82.04 ± 15.35**
EFL03-A	USU-2343	1.6	17 (28)	1.88 ± 0.09	132.51 ± 14.90	16.4 ± 5.0	**70.41 ± 10.39**
EFL04-A	USU-2344	1.2	19 (27)	2.24 ± 0.10	122.48 ± 15.02	23.1 ± 4.9	**54.68 ± 8.51**
EFL05-A	USU-2345	0.7	16 (33)	1.15 ± 0.06	50.60 ± 9.89	35.5 ± 7.5	**43.82 ± 9.52**
EFL06-A	USU-2346	0.35	19 (28)	1.52 ± 0.07	60.61 ± 9.59[4]	15.1 ± 4.4	**39.89 ± 7.36**
EFL07-A	USU-2347	1.9	16 (35)	2.54 ± 0.11	159.47 ± 15.52	11.7 ± 4.8	**62.86 ± 8.59**
EFL08-A	USU-2348	0.55	19 (38)	1.77 ± 0.08	138.47 ± 14.48	11.2 ± 6.3	**78.05 ± 11.00**

Table 3.4 Areas of various colluvial units (shaded gray) exposed on the south wall of the BMC trench.

TRENCH UNIT	Area-sq ft in GIS	True Area-Sq meters	Area-% of subtotal	Area plus crack fill[1]	Area-% of Total including crack fill	Debris facies only (contains gravel)[2]	% of Total Debris facies Area	Proportion of 6.5 m VSO
Meter square	*0.1521*	*1.00*						
CV-slope on HW	0.894	5.88	0.29					
CV-graben	0.057	0.37	0.02	6.37	0.29	3.31	**0.20**	**1.27**
CIV	0.666	4.38	0.22	5.07	0.23	2.89	**0.17**	**1.11**
CIII	0.3718	2.44	0.12	2.44	0.11	2.44	**0.14**	**0.94**
CII	0.646	4.25	0.21	4.94	0.22	4.94	**0.29**	**1.89**
CI	0.4068	2.67	0.13	3.37	0.15	3.37	**0.20**	**1.29**
subtotal	3.0416	20.00	1.00	22.19	1.00	16.95	1.00	6.5
Crack fill-upper big	0.1059	0.70						
Crack fill-upper small	0.0174	0.11						
Crack fill-lower	0.2101	1.38				**Mean**	**0.20**	**1.3 m**
Total with crack fill	3.375	22.19				**sigma**	**0.06**	**0.36 m**
						COV	**0.28**	

[1] part of the crack fill area assigned to each wedge, based on cross-cutting relationships

[2] does not count the sandy, clast-poor wash facies. The volume of wash facies may be affected by factors other than the scarp height formed during each rupture event. For example, the longer the time between faulting events, the larger the wash facies wedge can grow. The higher the eolian influx rate (climate-controlled), the faster the wash facies wedge can grow.

Table 4.4 Estimated surface rupture lengths and magnitudes for the surface faulting events interpreted from the 2003 and 2016 trenches.

Trench	Event	Age Range (ka)	Vertical Displace-ment (m)	Displace-ment Parameter	Empirical Surface Rupture Length (km)	Empirical Magnitude from Displacement
2003	*Z*	*13-17*	*3.0*	D_{max}	33.6	6.95
2003	*Y*	*38-41*	*4.45*	D_{max}	38.6	7.07
2003	*X*	*41-64*	*3.0*	D_{max}	33.5	6.95
2003	*W*	*>64*	*>0.8*	D_{max}	>21.2	>6.54
		TOTAL	*>11.5*	*Mean*	35.2	
		Mean	***2.6 m***			**6.90**
2016	Z	0.5-1.0	1.27	D_{avg}	35.4	6.85
2016	X+Y	44-45	2.05	D_{avg}	40.5	6.98
2016	W	55	1.89	D_{avg}	39.6	6.96
2016	V	82-87	1.29	D_{avg}	36.0	6.85

		TOTAL	6.5	Mean	37.9	
		Mean	**1.6 m**			**6.91**

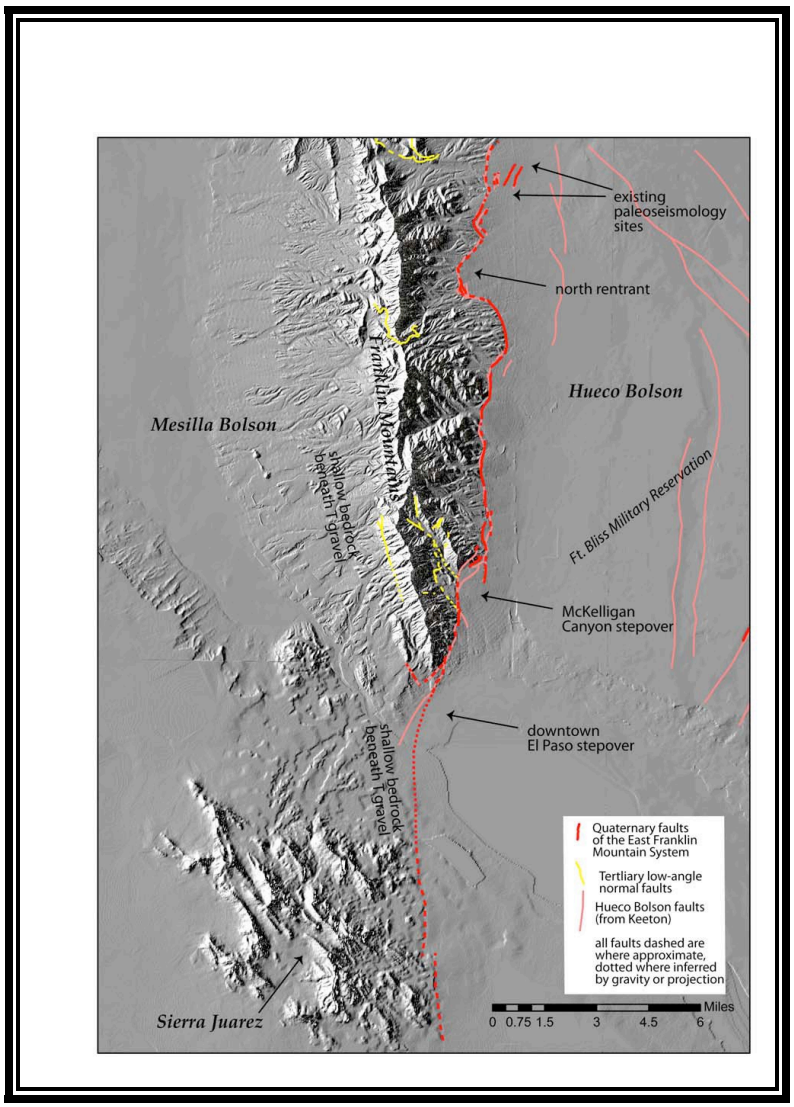

Figure. 1.4 Regional map of the East Franklin Mountain fault system (red) in the El Paso-Juarez Region on a shaded relief base prepared from SRTM DEM from the USGS. Our mapping of the fault (red) is shown together with our digitized traces of Keeton's (1993) mapping (in magenta). In addition to the main fault trace note the locations of older, low-angle normal faults (in yellow) within the Franklin Mountains and surface ruptures in the Hueco Bolson that comprise part of the local Quaternary deformation. Also note the locations of previous work at the far north end of the fault.

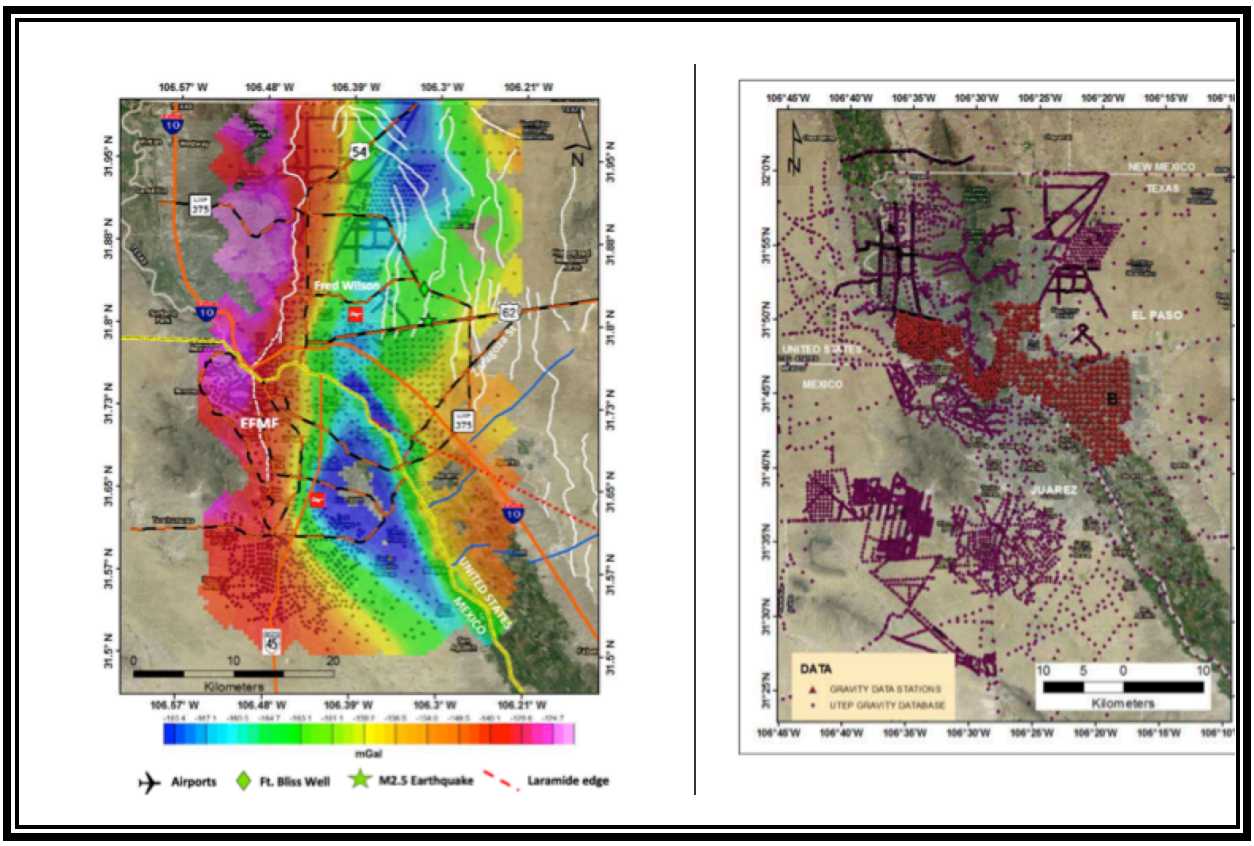

Figure 2.4 Complete Bouguer Anomaly map of the urbanized El Paso-Juarez region (left) and detail of gravity stations used for the map in downtown El Paso and Juarez (right). Note the steep gravity gradient that shows continuity of the EFMF through downtown El Paso to the Sierra Juarez. Also note this gradient continues southward past Sierra Juarez into far east El Paso County and into Chihuahua State (from Avila et. al., 2016). Green star indicates location of a M2.5 earthquake in 2012.

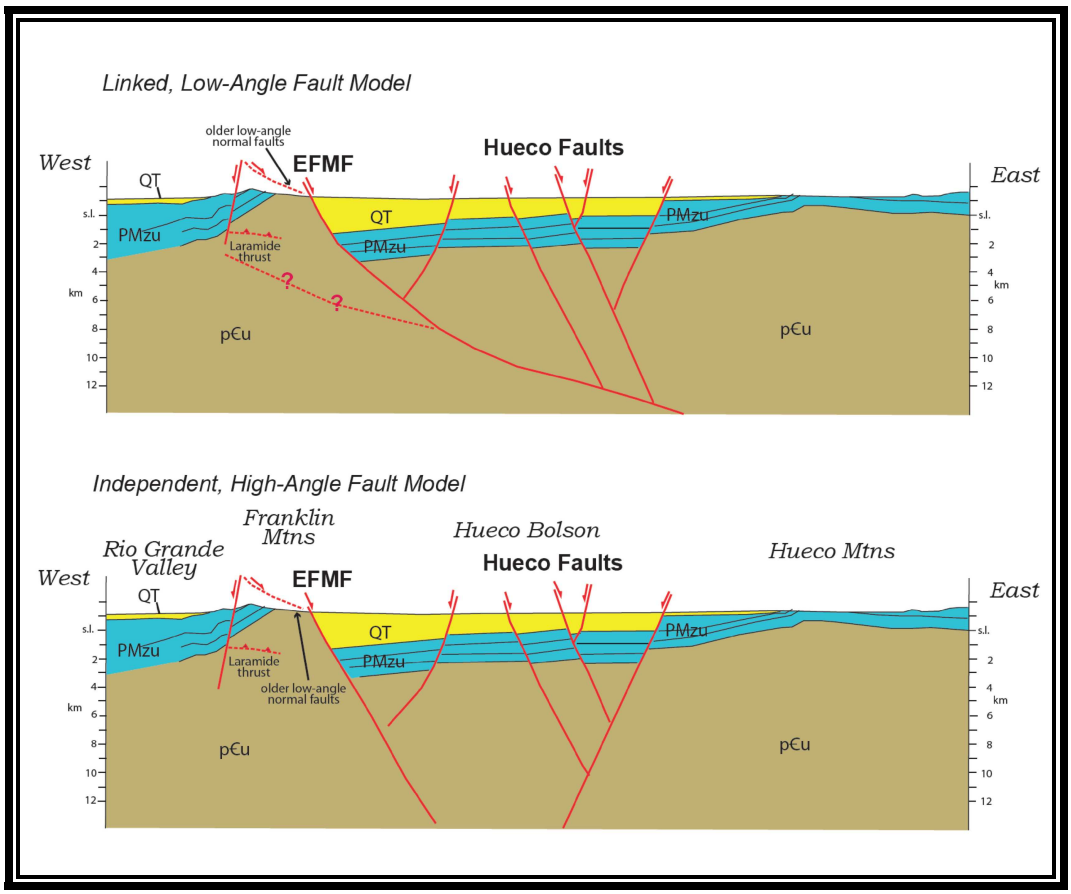

Figure 3.4 Schematic cross-sections across the Hueco Bolson and Hueco graben showing two alternative seismo-tectonic interpretations that relate the EFMF to the Hueco Bolson faults. Redrawn from section in Colins and Raney (2000).

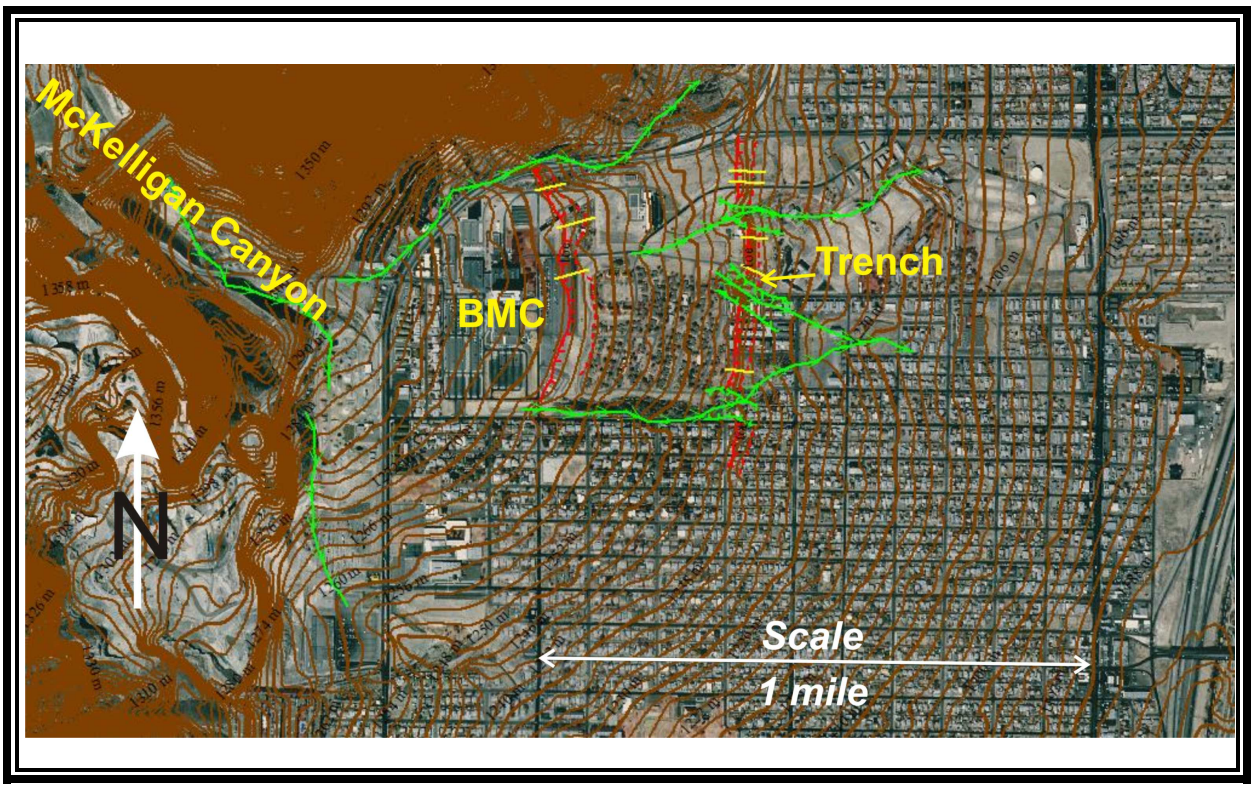

Figure 4.4a Annotated orthophoto with 2 m contours on the McKelligan alluvial fan. BMC, Beaumont Medical Center. Red lines show piedmont fault scarps. The eastern scarp is clearly a continuation of the range-front fault to the north, but the western scarp does not line up with any scarps to the north or sout, and may have been created by mass grading to create the level building pad to the west. Green lines show drainages that have incised into the part of the fan uplifted by the eastern piedmont scarp. The natural channel of McKelligan Creek downstream (east) of Alabama Street has been destroked by grading in the area of the BMC. However, a large channel (green) on the southern edge of the BMC between the two piedmiont scarps may be the remains of the last channel active prior to BMC construction.

Figure 4.4b Close-up of the eastern piedmont scarp (red lines, center) and gullies that cut through the scarp (green channels and erosional limits). Scarp incision suggests that the parts of the fan between the incised gullies were abandoned by active deposition after one or more faulting events and become relict surfaces. This inference is supported by the strong caliche soil developed on the footwall of the scarp (as exposed in the trench), because the Stage IV carbonate extends right up to ground surface. In other words, there is no evidence of Holocene or latest Pleistocene deposition on the footwall.

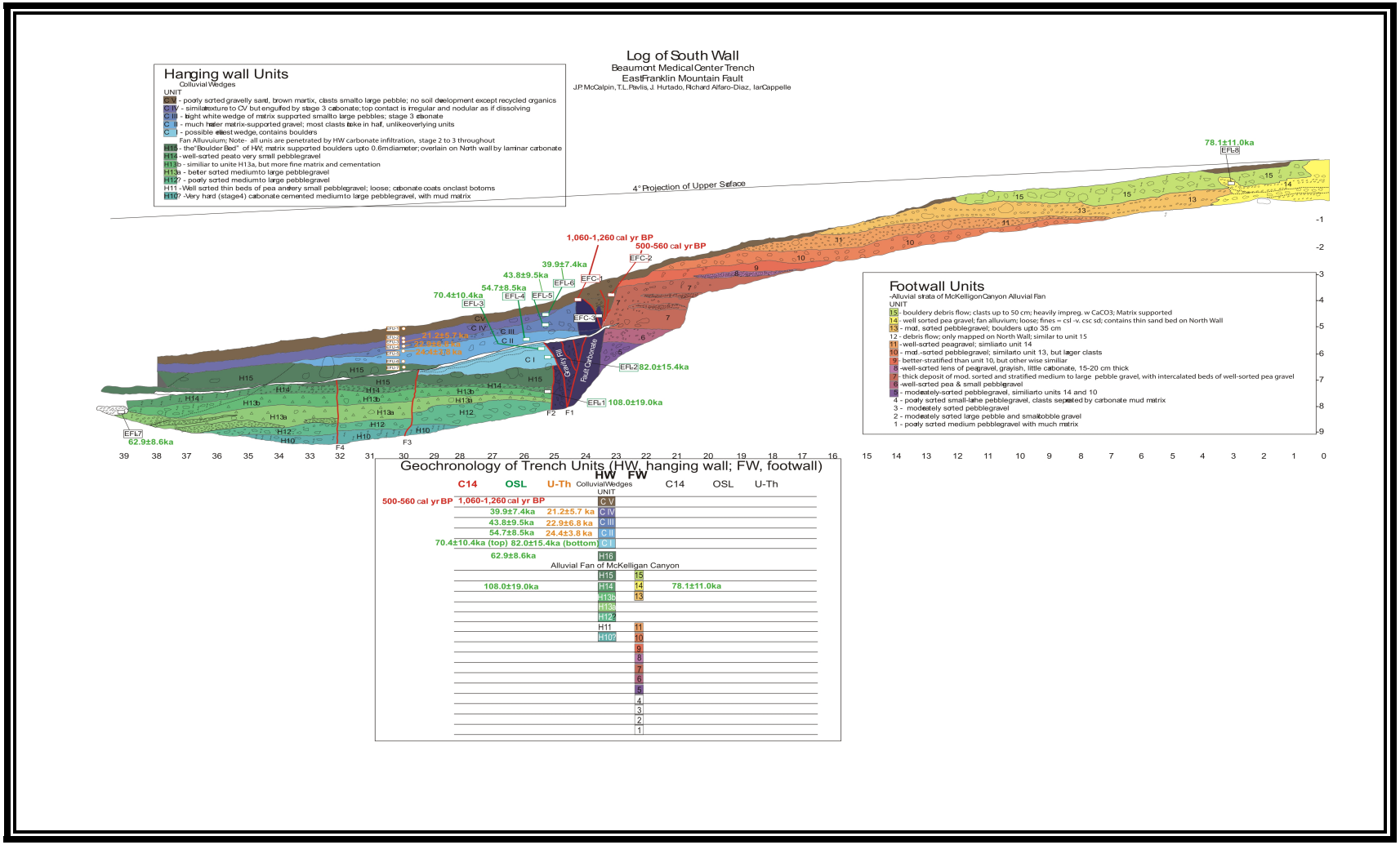

Figure 5.4 Log of the south wall of the BMC trench.

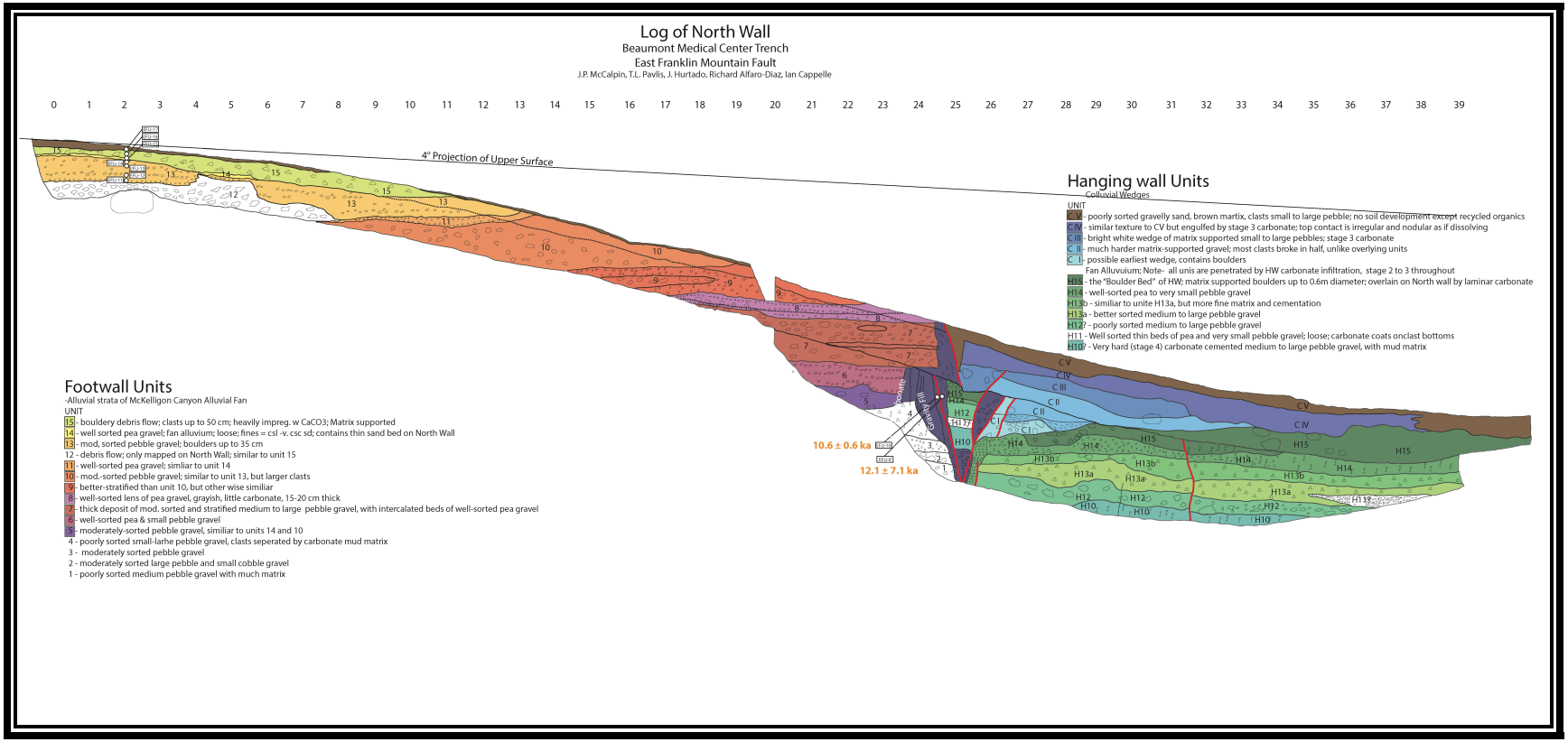

Figure 6.4 Log of north wall of the BMC trench.

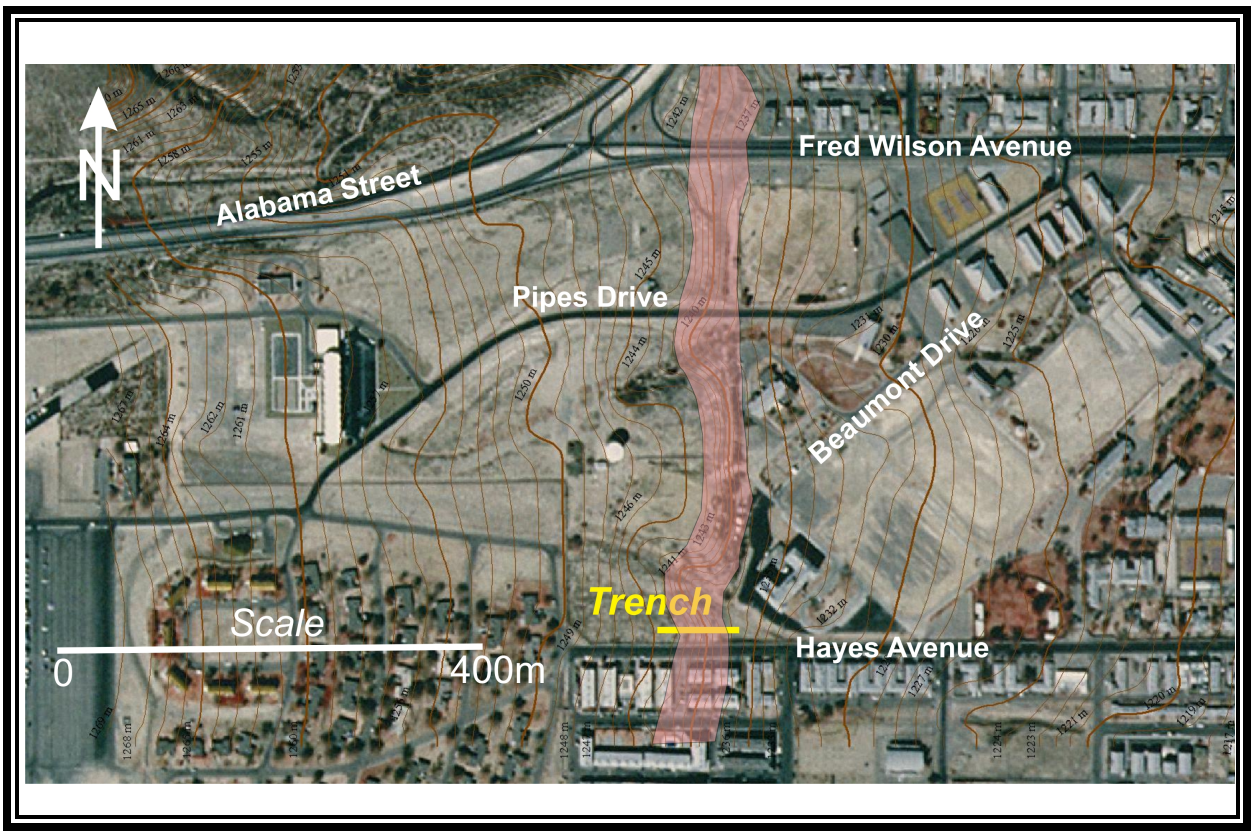

Figure 7.4 Location of the BMC trench. Annotated orthophoto with 1 m contours around the trench (yellow bar). Pink overlay shows the topographic fault scarp. The scarp is narrowest and steepest at center, where undercutting of the toe may have occurred during past grading. The scarp is broadest and gentlest at north and south where residential development has encroached on it. At the 2016 BMC trench site there was no evidence for either undercutting by grading of the hanging wall, or smoothing from land development.

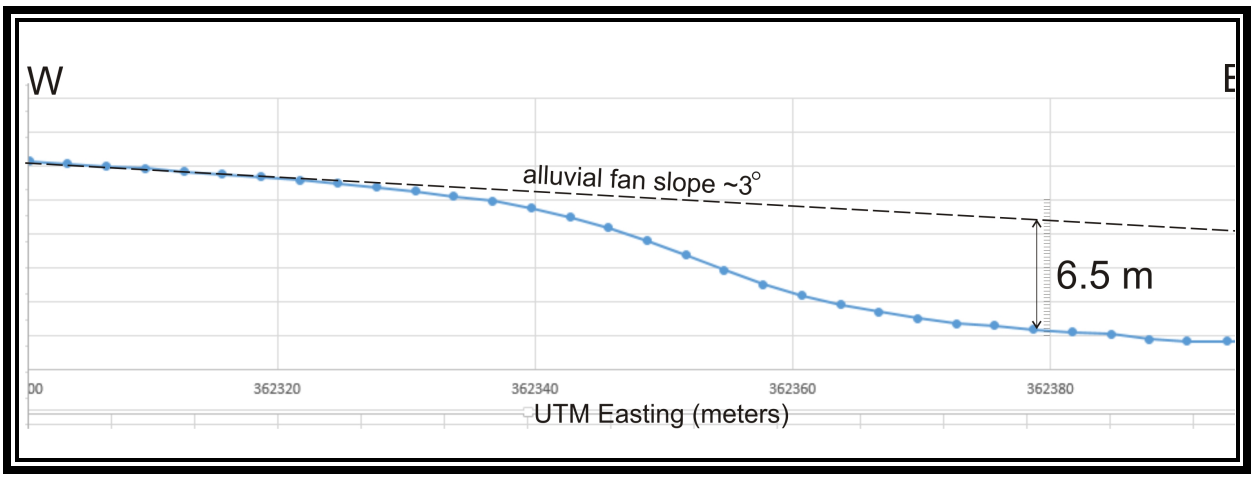

Figure 8.4 Topographic profile across fault scarp of the EFMF at the BMC trench site. No vertical exaggeration.

Figure 9.4 Photo of the westernmost part of the southern trench wall (footwall above the scarp crest). View to south. Yellow labels on string line at bottom are 1 m (right) and 2 m (left). Head of trench is just out of view to right. The upper half of the trench wall here is unit 15, a matrix-supported boulder diamicton (debris flow). The matrix is mostly composed of Stage IV soil carbonate (caliche, or calcrete); this is the relict soil of the Jornada II surface. The lower half of the wall is unit 14, composed of well-stratified, well-sorted stream gravels (hyperconcentrated flow deposits).

Figure 10.4 South wall, upper part of fault. Upper, before wall cleaning and stringing. Below, afterwards. Brown deposit against the fault is unit CV, the scarp-derived colluvium of the Most Recent Event.

Figure 11.4 Mosaic of main fault zone exposed on the south wall. Large yellow arrows indicate main fault. Smaller yellow arrows indicate minor faults of the boundaries of tension fissures. Note that only the MRE colluvium (unit CV) is not plugged by secondary calcium carbonate. Shoring rails are 20 cm wide. In a 1.0 to 1.5 m-wide zone of the hanging wall there are several secondary faults that dip 70°W and are truncated against the main fault. These structures represent two different processes. Type 1 abut hanging wall units (alluvium and colluvium) against fissure fill, and thus look like antithetic faults bounding the east side of filled fissures/graben. In Type 2, however, the fissures truncate the western (back) edges of colluvial wedges and appear stratigraphically higher than the wedges, as if they have been thrust against them (that is, synthetic fault movement). In some cases it appears that the west-dipping faults originated as Type 1 with down-to-the-west slip, but in later surface ruptures transformed into Type 2 with down-to-the-east slip. In other words, early-event fissure fills became impregnated with carbonate and welded themselves onto the footwall, and then in succeeding events they remained stuck to the fottwall while the softer hanging-wall strata dropped down to the east.

Figure 12.4 Photo of the main fault plane on the north walls of the trench. Yellow dotted line is drawn on the western edge of the carbonate-cemented fault zone. Upper wall is 1.5 m high, bench is 1.5 m wide, lower wall is 2.5 m high, shores are 2.1 m long. View to north.

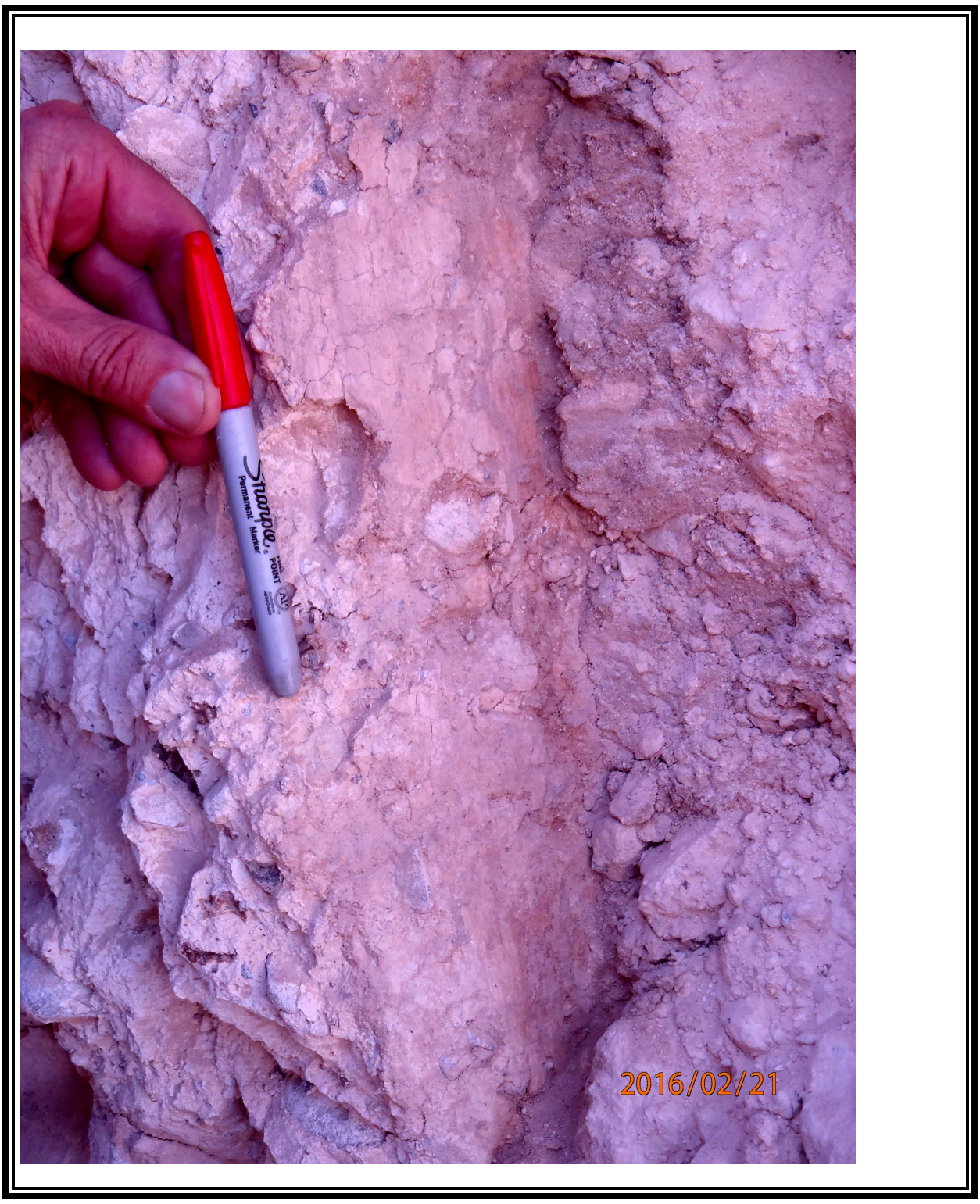

Figure 13.4 Slickensided carbonate on main fault plane, lower north wall below level line -7 m.

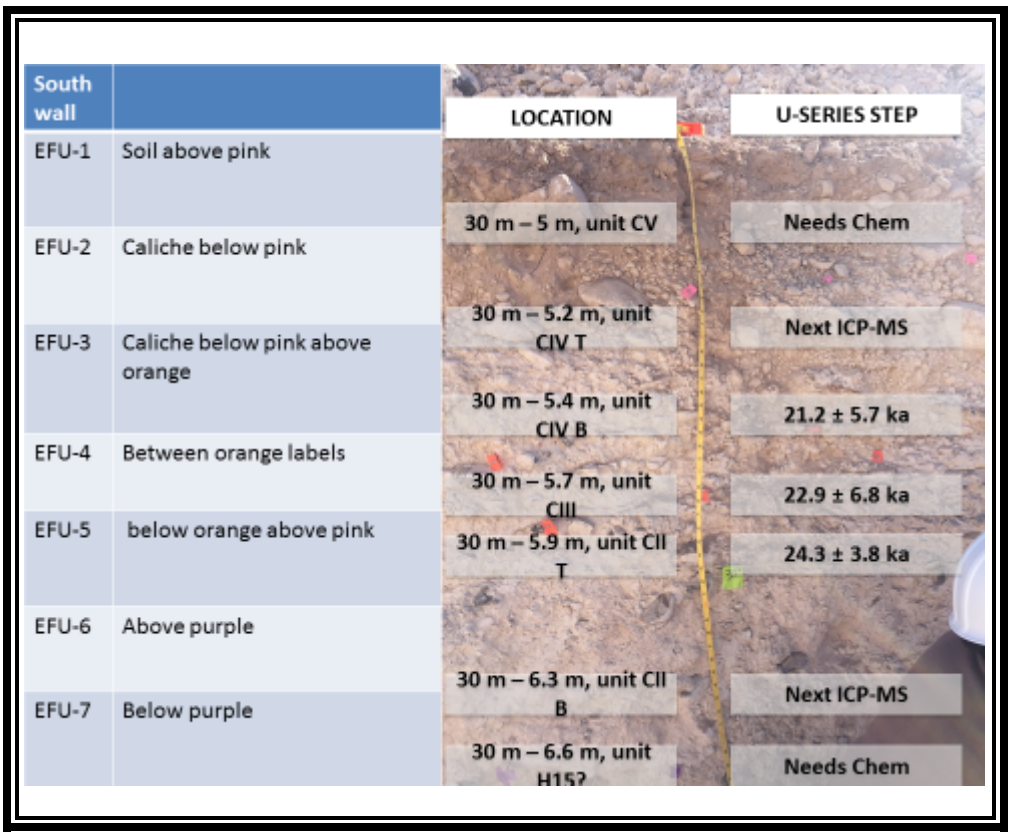

Figure 14.4 Location of the seven U-series samples from the colluvial wedge sequence exposed on the south trench wall.

North wall	Fault zone
25 m – -5.8 m	Hanging wall
25 m – -5.8 m	Foot wall

Figure 15.4 Photo sample sites EFU-9 and EFU-10, in the fault zone at the top of the lower north wall.

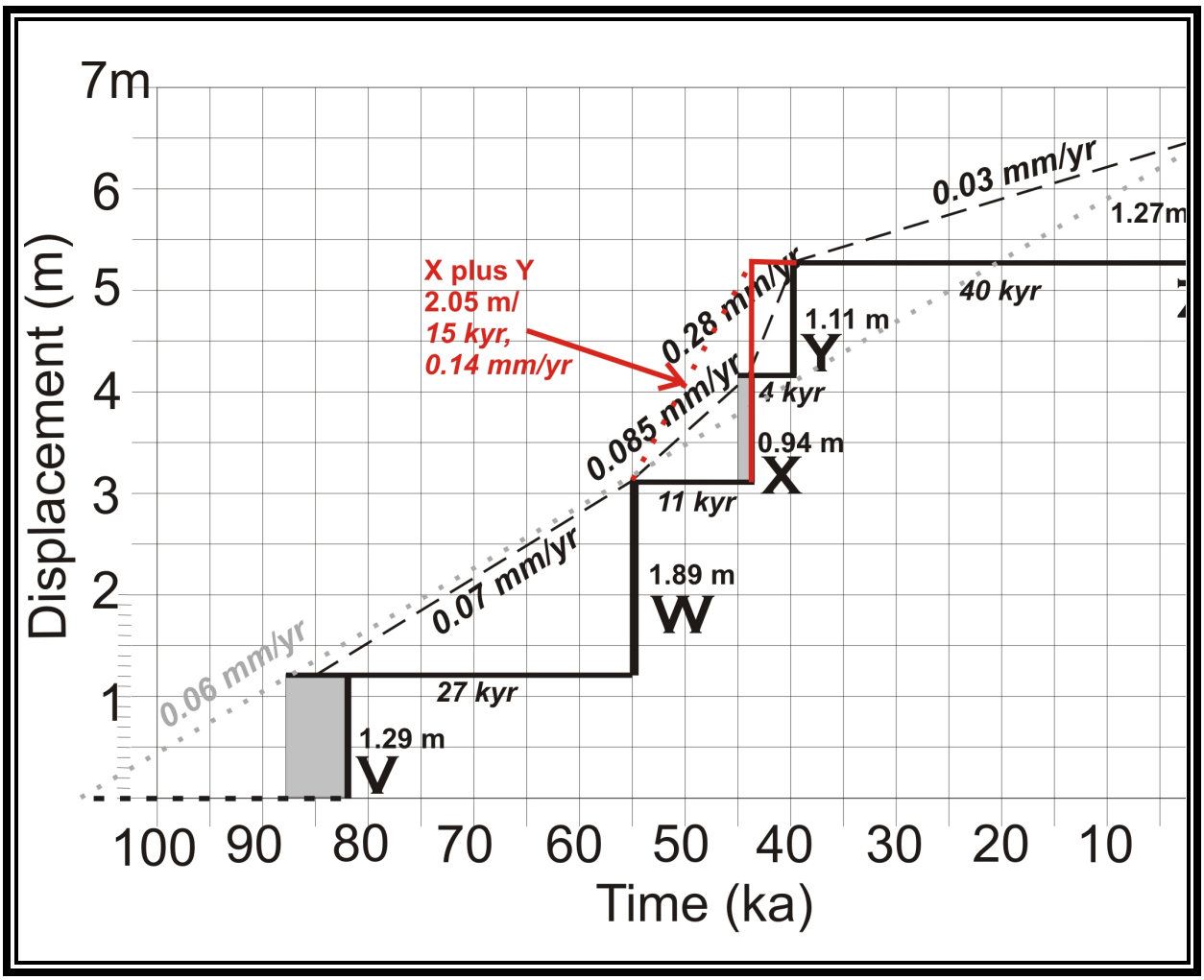

Figure 16.4 Slip-history diagram of the EFMF from the BMC trench. Displacements in each event were estimated by dividing the 6.5 m of cumulative vertical surface offset proportionally based on the exposure area of each debris-facies wedge on the south wall. Ages are OSL from the south trench wall. Gray boxes indicate that the true age of the rupture may be older than the OSL age (black vertical bars), because the dated sample came from the middle of a wedge, rather than the bottom. Red lines and labels represent an alternative rupture history assuming that wedges CIII and CIV are the lower and upper parts of a single wedge. See text for details.

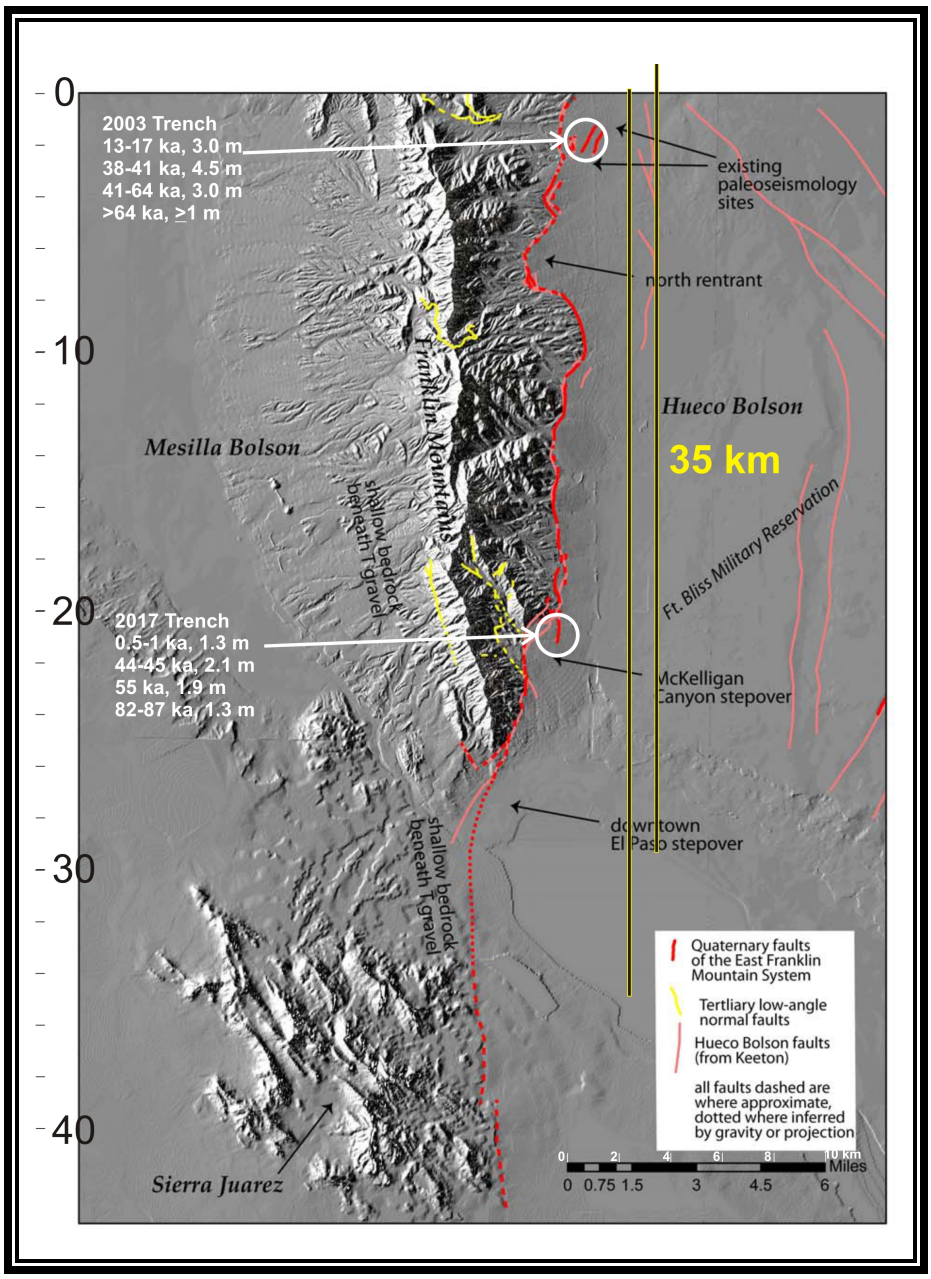

Figure 17.4 Map of the EFMF fault traces (red) with paleoearthquake data from the 2003 and 2017 trench sites. The yellow bars are 35 km long, the approximate length of surface ruptures implied by per-event displacements at the two sites.

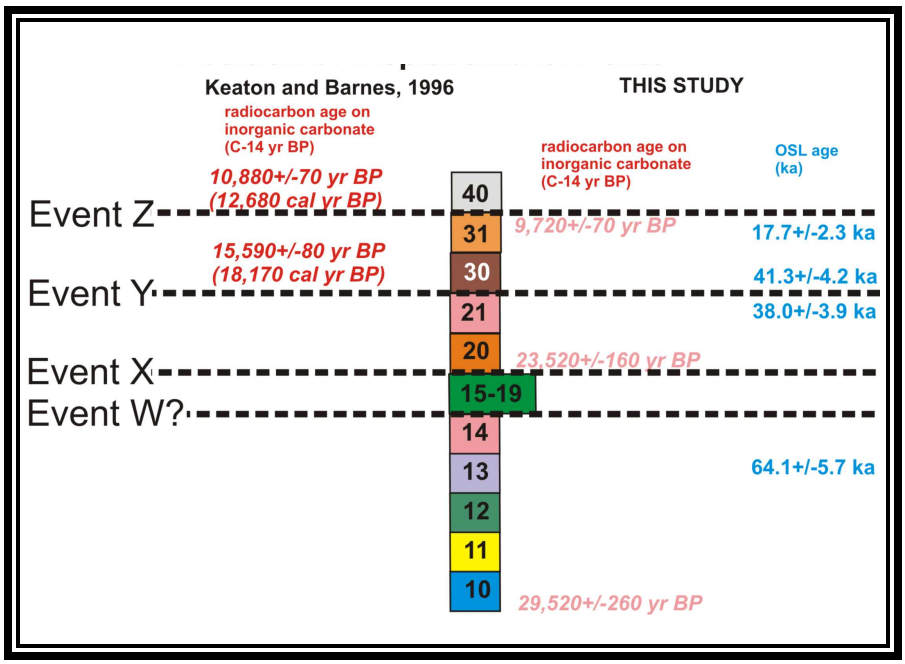

Figure 18.4 Event stratigraphy and age dates from the 1995 Keaton trench (left) and 2003 trench of McCalpin (2006) (right, labeled "This Study").

Figure 19.4 View west up the axis of the BMC Trench looking toward the range front of the East Franklin Mountains. Street at left is Hayes Avenue. Photo was taken after removal of the shores (visible at right edge) from the hanging-wall slot, just before backfilling.

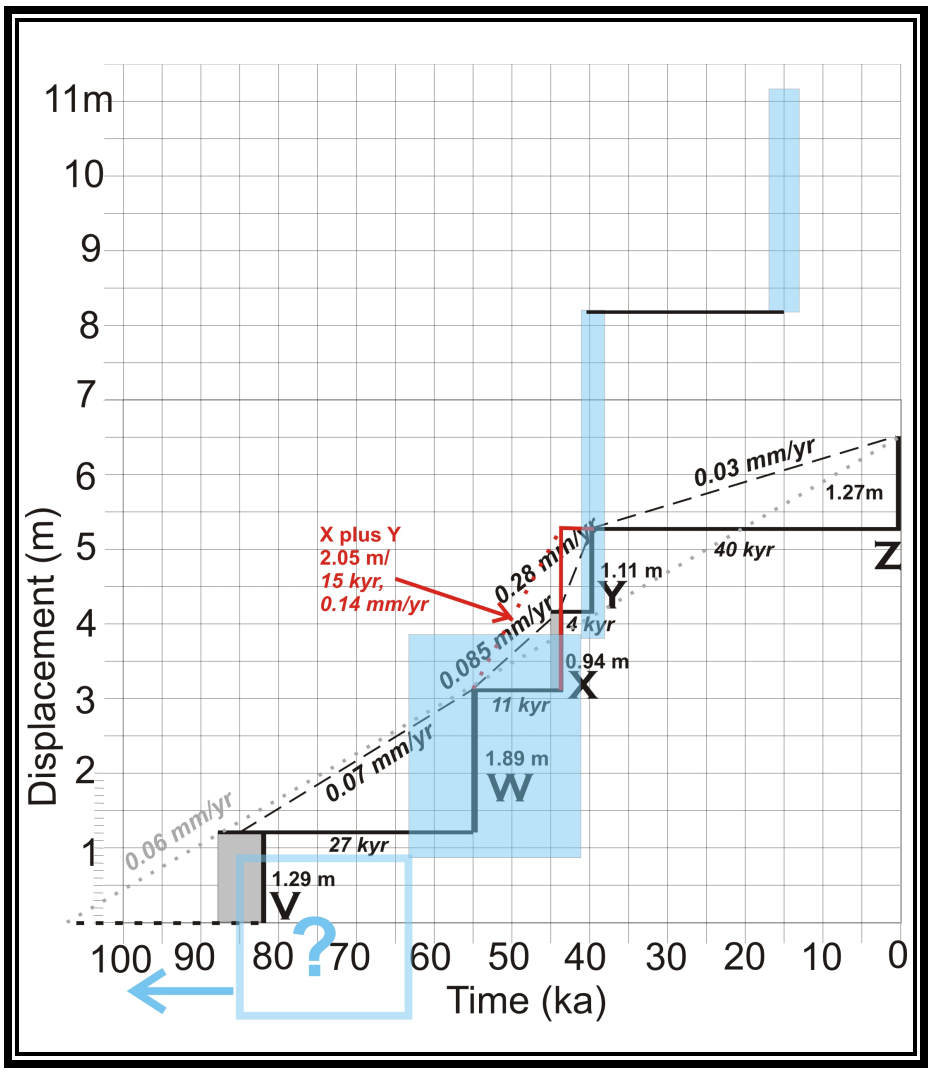

Figure 20.4 Composite slip-history diagram for the 2016 BMC trench (black lines and event letters) and the 2003 trench farther north (blue lines and rectangles; McCalpin, 2006). There was 6.5 m of vertical surface offset in the past 80 ka at the BMC trench, compared to >11.2 m in the past 64 ka at the 2003 trench.

References

Armour-Finch, L., 2014, Long term deformation in the Rio Grande Rift as inferred from topography and uplifted terraces: unpublished PhD thesis, The University of Texas at El Paso, United States – Texas.

Avila, V.M., Doser, D.I., Dana-Ornelas, O.S., Moncada, M.M., and Marrufo-Cannon, S.S., 2016, Using geophysical techniques to trace active faults in the urbanized northern Hueco Bolson, West Texas, USA and northern Chihuahua, Mexico: Geosphere, v. 12, no. 1, p. 264-280.

Cervera, S., 2008, The Quaternary Deformational History of the East Potrillo Mountains, Dona Ana County, New Mexico [M.S. thesis]: University of Texas at El Paso, 69 p.

Collins, E. W., and Raney, J. A., 1993, Late Cenozoic faults of the region surrounding the Eagle Flat study area, northwestern Trans-Pecos Texas: University of Texas at Austin, Bureau of Economic Geology final contract report, prepared for Texas Low-Level Radioactive Waste Disposal Authority under Interagency Contract IAC (92-93)-0910, 74p.

Collins, E.W., and Raney, J.A., 2000, Geologic Map of West Hueco Bolson, El Paso Region, Texas,. University of Texas at Austin, Bureau of Economic Geology, Miscellaneous Map No. 40,1:100,000

Collins, E. W., Raney, J. A., Machette, M. N., Haller, K. M., and Dart, R. L., 1996, Map and data for Quaternary faults in West Texas and adjacent parts of Mexico: U.S. Geological Survey Open-File Report 96-002, ii + 74 p., 1 folded plate, scale 1:750,000.

Dover, Kohl & Partners, 2012, Comprehensive Plan Amendaments to the 1/12/12 Draft (Draft 1), City of El Paso: Memo from Kohl, Dover & Partners, El Paso, TX to the El Paso City Plan Commission, February 21, 2012. www.elpasotexas.gov/muni_clerk/agenda/02-28-

12/02281210N - Part4.pdf

Fetzner, Keith, 1992, The interpretation of principal strains from calcite twins in the Franklin Mountains, Texas, M.S. Thesis, University of Texas at El Paso, El Paso, TX 79968, 51p.

Gile, L. H., Hawley, J. W., & Grossman, R. B. (1981). Soils and geomorphology in the Basin and Range area of Southern New Mexico: Guidebook to the Desert Project [Memoir 39]. Socorro, NM: New Mexico Bureau of Mines and Mineral Resources.

Hecker, S., Abrahamson, N. A., and Wooddell, K. E., 2013, Variability of Displacement at a Point: Implications for Earthquake-Size Distribution and Rupture Hazard on Faults: Bulletin of the Seismological Society of America, vol. 103, issue 2A, pp. 651-674.

Keaton, J.R, 1993, Maps of potential earthquake hazards in the urban area of El Paso, Texas: Technical report to U.S. Geological Survey, under Contract 1434-92-G-2171, July 28, 1993, 87 p.

Keaton, J.R, and Barnes, J.R, 1996, Paleoseismic evaluation of East Franklin Mountains fault, El Paso, Texas: Technical report to U.S. Geological Survey, under Contract 1434-94-G-2389, May 10, 1996, 45 p.

Machette, M.N., 1998, Contrasts between short- and long-term records of seismicity in the Rio Grande rift—important implications for seismic-hazard assessments in areas of slow extension, in Lund, W.R. (ed.) Basin and Range Province Seismic-Hazards Summit, Proceedings: Utah Geological Survey, Miscellaneous Publication 98-2, p. 84-95.

McCalpin, J.P., 2006, Quaternary Faulting and Seismic Source Characterization in the El Paso-Juarez Metropolitan Area; Collaborative Research with the University of Texas at El Paso: unpublished Final Technical Report submitted to U.S. Geological Survey by GEO-HAZ Consulting, Inc., Contract 03HQGR0056, 26 APR 2006, 68 p.

(http://earthquake.usgs.gov/research/external/reports/03HQGR0056.pdf)

McCalpin, J.P. (ed.), 2009a, Paleoseismology, 2nd Ed.: Academic Press, Elsevier, San Diego, CA, 708 p.

McCalpin, J.P. (ed.), 2009b, Application of paleoseismic data to seismic hazard assessment and neotectonic research, in McCalpin, J.P. (ed.), Paleoseismology, 2nd Ed.: Academic Press, Elsevier, San Diego, CA, p. 603-708. Available online at www.elsevierdirect.com/companions/9780123735768

McCalpin, J.P., Olig, S.S., Harrison, J.B.J. and Berger, G.W., 2006, Quaternary faulting and soil formation on the County Dump fault, Albuquerque, New Mexico: New Mexico Bureau of Geology & Mineral Resources, Socorro, New Mexico, Circular 212, 36 p.

McCalpin, J.P., Harrison, J.B.J., Berger, G.W., and Tobin, H.C., 2011, Paleoseismicity of a low-slip-rate normal fault in the Rio Grande rift, USA; The Calabacillas fault, Albuquerque, New Mexico, in Audemard, F.A., Michetti, A.M. and McCalpin, J.P. (eds.), Geological Criteria for Evaluating Seismicity Revisited: Forty Years of Paleoseismic Investigations and the Natural Record of Past Earthquakes: Geological Society of America Special Paper 479, p. 23-46.

Monger, H. C., Gile, L. H., Hawley, J.W., and Grossman, R.B., 2009, The Desert Project - An Analysis of Aridland Soil-Geomorphic Processes: New Mexico State University, Agriculture Experiment Station, Bulletin 798, 76 p. http://aces.nmsu.edu/pubs/research/weather_climate/BL798/welcome.html

Pavlis, T.L., Langford, R., Serpa, L., Hurtado, J., 2010, Computer based data acquisition and visualizations systems in field geology; Results from 12 years of experimentation and future potential: Geosphere, 6, 275-294, doi: 10.1130/GES00503.1

Personius, S. F., and Mahan, S. A., 2000, Paleoearthquake recurrence on the East Paradise fault zone, metropolitan Albuquerque, New Mexico: Seismological Society of America, Bulletin, v. 90, no. 2, pp. 357–369.

Personius, S. F., Eppes, M. C., Mahan, S. A., Love, D. W., Mitchell, D. K., and Murphy, A., 2000, Log and data from a trench across the Hubbell Spring fault zone, Bernalillo County, New Mexico: U.S. Geological Survey, Miscellaneous Field Studies Map MF-2348, available at

Raney, J.A., and Collins, E.W., 1994a, Geologic map of the El Paso quadrangle, Texas: The University of Texas at Austin, [Texas] Bureau of Economic Geology Open-File Map, 1 sheet, scale 1:24,000.

Raney, J.A., and Collins, E.W., 1994b, Geologic map of the North Franklin Mountain quadrangle, Texas: The University of Texas at Austin, [Texas] Bureau of Economic Geology Open-File Map, 1 sheet, scale 1:24,000.

Scharman, Mitchell R., 2006, Structural constrains on Laramide shortening and Rio Grande rift extension in the central Franklin Mountains, El Paso County, Texas, M.S. Thesis, University of Texas at El Paso, El Paso, TX 79968, 70p.

Scherschel, C.A., 1995, Quaternary geologic and geomorphic framework for Neotectonic analysis of the northeastern Franklin Mountains, El Paso, Texas: unpublished MS thesis, Texas A&M University, College Station, TX.

Stacy, John K., 1991, Structural and tectonic history of McKelligon Canyon, El Paso County, Texas, M.S. Thesis, University of Texas at El Paso, El Paso, TX 79968, 75p.

Wells, D.L. and K.J. Coppersmith, 1994, Empirical relationships among magnitude, rupture

length, rupture area, and surface displacement: Bulletin of the Seismological Society of America, v. 84, p. 974-1002

Wu, Kaiwen, 2002, The structural geology and tectonics of the southern Franklin Mountains in El Paso County, Texas, M.S. Thesis, University of Texas at El Paso, El Paso, TX 79968, 57p.

Vita

Richard A. Alfaro-Diaz earned his Bachelor of Science degree in Geological Sciences from UTEP in 2013. In 2015, he received his Master of Science degree in Geophysics from UTEP. He joined UTEP's doctoral program in Geological Sciences in 2015. Dr. Alfaro was a National Science Foundation SMARTS Scholar, and National Science Foundation GK-12 Fellow. He was also a recipient of the Africa Array Scholarship, the Keck Geology Fellowship, and the W. P. Nash Geophysics Scholarship. Dr. Alfaro has presented his research at several meetings including the Latin American and Caribbean Seismological Commission in 2016, the Seismological Society of America in 2017, and the Society for Advancement of Chicanos and Native Americans in Science meeting in 2018. His work has appeared in the proceedings of these conferences as well as American Geophysical Union. While pursuing his degree, Dr. Alfaro worked as a research associate for the Department of Geological Sciences and UTEP's Cyber-ShARE center. Dr. Alfaro has accepted a postdoctoral research associate position in Geophysics at Los Alamos National Lab where he will work as a full-time researcher. Dr. Alfaro's dissertation, "Unraveling Earthquake Stresses: Insights from Dynamically Triggered Earthquakes & Quaternary Faulting and Urban Seismic Hazards in the El Paso Metropolitan Area" was supervised by Dr. Aaron Velasco.

Contact Information: Richard-Alfaro@outlook.com